SEMG-BASED ANKLE POSITION AND MOMENT PREDICTION IN SILICO: NEURAL NETWORK APPROACH AND MUSCLE SELECTION

by

Ahmet Doğukan Keleş

B.S., in Mechatronics Engineering, Yıldız Technical University, 2014

M.S., in Biomedical Engineering, Boğaziçi University, 2017

Submitted to the Institute of Biomedical Engineering

in partial fulfillment of the requirements

for the degree of

Doctor

of

Philosophy

Boğaziçi University

2023

SEMG-BASED ANKLE POSITION AND MOMENT PREDICTION IN SILICO: NEURAL NETWORK APPROACH AND MUSCLE SELECTION

APPROVED BY:

Prof. Dr. Can A. Yücesoy .....
(Thesis Advisor)

Prof. Dr. Mehmed Özkan .....

Assoc. Dr. Evren Samur .....

Prof. Dr. Oliver Röhrle .....

Prof. Dr. Volkan Patoğlu .....

DATE OF APPROVAL: 19 September 2023

ACKNOWLEDGMENTS

I would like to express my deepest gratitude to my advisor Prof. Dr. Can A. Yücesoy for his inspiring guidance, invaluable support, insight on several issues, and the opportunities he has offered throughout this study. His expertise and guidance have been instrumental in shaping this dissertation and my academic journey.

I would like to express my gratitude to the members of my doctoral committee, Prof. Dr. Mehmed Özkan and Assoc. Prof. Dr. Evren Samur, for their constructive feedback, critical evaluation, and contributions. Their examination has significantly enhanced the quality and depth of my research.

It was an honor and pleasure for me to have the opportunity to share my study and its outcomes with Prof. Dr. Oliver Röhrle and Prof. Dr. Volkan Patoğlu, the external members of the dissertation committee. I am grateful for taking their time and providing a valuable and enjoyable discussion session.

Most importantly, I am deeply grateful to my family for their unconditional love, encouragement, inspiration, and belief in my abilities. Their support was the pillar of my success and kept me motivated during challenging times.

Finally, I dedicate this dissertation to my dearest Cemre Su Kaya Keleş, who has been with me since the first day of this journey. Her belief in me during moments of self-doubt has been a motivator that kept me going. Her patience and understanding during long hours of study and research have been immeasurable. I am grateful for your endless love, patience, and support, which have been the driving force. Without you, none of them would have been within reach, my loving wife.

ACADEMIC ETHICS AND INTEGRITY STATEMENT

I, Ahmet Doğukan Keleş, hereby certify that I am aware of the Academic Ethics and Integrity Policy issued by the Council of Higher Education (YÖK) and I fully acknowledge all the consequences due to its violation by plagiarism or any other way.

Name :

Signature:

Date:

ABSTRACT

SEMG-BASED ANKLE POSITION AND MOMENT PREDICTION IN SILICO: NEURAL NETWORK APPROACH AND MUSCLE SELECTION

Lower limb amputation is the partial or complete removal of a limb, and powered prostheses are the best solution for restoring amputees' locomotion abilities. Although recent advancements have enhanced their hardware, autonomous adaptation is required to achieve natural ambulation. The utilization of surface electromyogram (sEMG) holds promise, whereas real-time analysis is challenging. Also, a systematic analysis should be conducted for muscle selection to ensure compatibility with different levels of amputations. Therefore, the feature extraction was implemented for non-normalized sEMG amplitudes, and an economic algorithm minimizing sEMG input was sought. For the sake of different amputation level compatibility, a practical algorithm was aimed to limit the use of lower leg muscles. In this context, neural network-based algorithms with timing-based approaches utilizing sEMG amplitudes as inputs have been developed to (1) predict sagittal ankle position and moment during ground-level walking and (2) rank all muscle combinations based on success. Eight leg muscles were studied: tibialis anterior (TA), soleus (SO), medial gastrocnemius (MG), peroneus longus (PL), rectus femoris (RF), vastus medialis (VM), biceps femoris (BF) and gluteus maximus (GMax). The results showed the best-performing muscle variation was MG+RF+VM whereas, PL and GMax+VM were distinguished as the economic and practical variations ($r_{position}$>0.90, r_{moment}>0.97), respectively. The analysis regarding the effect of window size selection for feature extraction on prediction accuracy revealed that a window size of 150 ms demonstrated the best performance for the proposed neural network architecture. The cross-validation results supported the repeatability of the structure and methodology.

Keywords: Surface Electromyography, Neural Network, Powered Ankle Prosthesis.

ÖZET

BİLGİSAYAR ORTAMINDA SEMG TABANLI AYAK BİLEĞİNİN POZİSYON VE MOMENT TAHMİNİ: SİNİR AĞI YAKLAŞIMI VE KAS SEÇİMİ

Alt ekstremite amputasyonu, bir uzvun kısmi veya tamamen çıkarılmasıdır ve tahrikli protezler, ampütelerin hareket yeteneklerini eski haline getirmekte en iyi çözümdür. Son gelişmeler donanımlarını geliştirmiş olsa da, doğal yürüyüş için otonom adaptasyon gereklidir. Yüzey elektromiyogramının (sEMG) kullanımı umut vadederken, gerçek zamanlı analiz zorluklar içermektedir. Ayrıca, farklı amputasyon seviyeleriyle uyum sağlamak için kas seçimine yönelik sistematik analiz yapılmalıdır. Bu nedenle, öznitelik çıkarımı normalize edilmemiş sEMG genlikleri üzerinden gerçekleştirilmiş ve sEMG girişini en aza indiren bir ekonomik algoritma aranmıştır. Farklı amputasyon seviyeleriyle uyum için, alt bacak kaslarının kullanımını sınırlayan pratik bir algoritma hedeflenmiştir. Bu bağlamda, (1) yer seviyesinde yürüyüş sırasında sagittal ayak bileği pozisyonunu ve momentini tahmin etmek ve (2) başarıya dayalı olarak tüm kas kombinasyonlarını sıralamak amacıyla sEMG genliklerini girdi olarak kullanan zaman temelli yaklaşımlarla çalışan sinir ağı tabanlı algoritmalar geliştirilmiştir. Sekiz bacak kası incelenmiştir: tibialis anterior (TA), soleus (SO), medial gastrocnemius (MG), peroneus longus (PL), rectus femoris (RF), vastus medialis (VM), biceps femoris (BF) ve gluteus maximus (GMax). Sonuçlar, en iyi performans gösteren kas varyasyonunun MG+RF+VM olduğunu, PL ve GMax+VM varyasyonlarının sırasıyla ekonomik ve pratik algoritma girdileri ($r_{position}$>0.90, r_{moment}>0.97) olduğunu ortaya koymuştur. Öznitelik çıkarımı için pencere boyutu seçiminin tahmin doğruluğu üzerindeki etkisine ilişkin analiz, önerilen sinir ağı mimarisi için 150 ms'lik bir pencere boyutunun en iyi performansı sergilediğini göstermiştir. Çapraz doğrulama sonuçları, yapı ve yöntemin tekrarlanabilirliğini desteklemiştir.

Anahtar Sözcükler: Yüzey Elektromiyografisi, Yapay Sinir Ağı, Güçlendirilmiş Ayak Bileği Protezi.

TABLE OF CONTENTS

ACKNOWLEDGMENTS iii
ACADEMIC ETHICS AND INTEGRITY STATEMENT iv
ABSTRACT v
ÖZET vi
LIST OF FIGURES x
LIST OF TABLES xii
LIST OF SYMBOLS xiii
LIST OF ABBREVIATIONS xiv
1. INTRODUCTION 1
1.1 Related Literature 1
1.1.1 Lower Limb Amputations and Prostheses 1
1.1.2 Human Ankle Biomechanics 3
1.1.3 Electromyogram Signal 6
1.1.4 Neural Network Structures 8
1.2 Outline of the Thesis 15
1.2.1 Aim of the Study 15
1.2.2 Overview 15
1.3 List of Publications Resulting from the Thesis 16
1.3.1 Journal Articles 16
1.3.2 Conference Proceedings 17
2. DEVELOPMENT OF A NEURAL NETWORK-BASED CONTROL ALGORITHM FOR POWERED ANKLE PROSTHESIS 18
2.1 Introduction 18
2.2 Materials and Methods 20
2.2.1 Dataset 20
2.2.2 Neural Network Development 21
2.2.3 Neural Network Training 22
2.2.3.1 Main and Versatility Implementations 22
2.2.3.2 Data Augmentation 23

2.2.3.3 Training 23
2.2.4 Evaluation of the Developed Neural Networks 24
2.2.4.1 Main Implementation 24
2.2.4.2 Versatility Implementation 24
2.3 Results 25
2.3.1 Main Implementation 25
2.3.2 Versatility Implementation 28
2.4 Discussion 29
2.5 Conclusion 35
3. THE USE OF NON-NORMALIZED SURFACE EMG AND FEATURE INPUTS FOR LSTM-BASED POWERED ANKLE PROSTHESIS CONTROL ALGORITHM DEVELOPMENT 36
3.1 Introduction 36
3.2 Materials and Methods 39
3.2.1 Data Utilized and Summary of Data Collection Procedures . . . 39
3.2.2 Neural Network Development 40
3.2.3 Neural Network Training 43
3.2.4 Evaluation of the Developed Neural Networks 44
3.3 Results 45
3.3.1 sEMG Feature Selection 45
3.3.2 Muscle Selection 46
3.4 Discussion 55
3.5 Conclusion 61
4. THE OPTIMIZATION OF THE LSTM-BASED ANKLE POSITION AND MOMENT PREDICTOR 63
4.1 Introduction 63
4.2 Materials and Methods 65
4.2.1 Gait Data Utilized 65
4.2.2 Neural Network Development 66
4.2.3 Neural Network Training 67
4.2.4 Evaluation of the Developed Neural Networks 67
4.3 Results 68

4.4 Discussion 71
4.5 Conclusion 75
5. GENERAL DISCUSSION 76
5.1 Neural Network Approach 76
5.2 Muscle Selection 78
5.3 Limitations and Future Directions 80
APPENDIX A. VISUALIZATIONS OF CORRELATIONS BETWEEN ACTUAL VS. ESTIMATED ANKLE POSITION AND MOMENT 82
APPENDIX B. VISUALIZATIONS OF EXTRACTED FEATURES 84
APPENDIX C. THE COMPARISON OF MUSCLE VARIATIONS 88
APPENDIX D. THE VERSATILITY IMPLEMENTATION FOR SEMG FEATURE SELECTION 102
REFERENCES 109

LIST OF FIGURES

Figure 1.1	Transtibial and ankle-foot amputations.	2
Figure 1.2	Examples of lower limb prostheses.	3
Figure 1.3	Human ankle biomechanics for level walking.	4
Figure 1.4	A motor unit and the muscle fibers it innervates.	7
Figure 1.5	The representation of the sliding window for feature extraction.	8
Figure 1.6	A sketch of biological neuron.	9
Figure 1.7	A basic model of a single artificial neuron.	10
Figure 1.8	An example of an ANN with one hidden layer.	11
Figure 1.9	An illustration of a TDNN.	12
Figure 1.10	Inner structure of LSTM unit.	13
Figure 2.1	NN structure and data generation for training.	22
Figure 2.2	Temporal success assessment for TA + MG + BF.	29
Figure 2.3	Temporal success assessment for MG + BF + GMax.	30
Figure 3.1	Block diagram of the LSTM structures for ankle position and moment prediction.	41
Figure 3.2	Mean and standard deviation of sEMG signals and its extracted features for the TA muscle.	44
Figure 3.3	Temporal success assessment for IEMG+WL.	49
Figure 3.4	Temporal success assessment for PL.	53
Figure 3.5	Temporal success assessment for MG+RF+VM.	54
Figure 3.6	Temporal success assessment for GMax+VM.	55
Figure 4.1	*Post hoc* test results for the effect of window sizes on joint position and moment prediction.	68
Figure 4.2	Temporal success assessment for the window size of 150 ms.	70
Figure A.1	Four muscle combination averaged results for the self-selected speed classes of adult and young age group.	82
Figure A.2	Three muscle combination averaged results for the self-selected speed classes of adult and young age group.	82

Figure A.3 Two muscle combination averaged results for the self-selected speed classes of adult and young age group. 83
Figure A.4 Single muscle combination averaged results for the self-selected speed classes of adult and young age group. 83
Figure B.1 Mean and standard deviation of sEMG signals and its extracted features for the soleus muscle. 84
Figure B.2 Mean and standard deviation of sEMG signals and its extracted features for the medial gastrocnemius muscle. 84
Figure B.3 Mean and standard deviation of sEMG signals and its extracted features for the peroneus longus muscle. 85
Figure B.4 Mean and standard deviation of sEMG signals and its extracted features for the rectus femoris muscle. 85
Figure B.5 Mean and standard deviation of sEMG signals and its extracted features for the biceps femoris muscle. 86
Figure B.6 Mean and standard deviation of sEMG signals and its extracted features for the vastus medialis muscle. 86
Figure B.7 Mean and standard deviation of sEMG signals and its extracted features for the gluteus maximus muscle. 87

LIST OF TABLES

Table 2.1	Training and test datasets for the main and versatility implementations.	23
Table 2.2	The comparison of the NN variations.	26
Table 2.3	TA+MG+BF versatility per different implementation datasets.	28
Table 2.4	MG+BF+GMax versatility per different implementation datasets.	28
Table 3.1	Mathematical definition of the sEMG feature extraction methods.	42
Table 3.2	The comparison of the performance of sEMG feature variations utilizing the muscle combination MG+BF+GMax.	47
Table 3.3	The best-performing 30 muscle combinations determined by utilizing the sEMG feature IEMG+WL.	50
Table 4.1	The performance comparison of window sizes for the IEMG+WL feature combination utilizing the sEMG signals of MG+RF+VM muscle combination.	69
Table 4.2	Cross-validation results.	69
Table C.1	The comparison of the muscle variations.	89
Table D.1	The comparison of the sEMG feature variations calculated over MG+TA.	103
Table D.2	The comparison of the sEMG feature variations calculated over BF+MG+TA.	105
Table D.3	The comparison of the sEMG feature variations calculated over BF+MG+TA+RF+GMax.	107

LIST OF SYMBOLS

mV	Millivolt
x	Input
y	Output
f	Function
b	Bias
w	Weight
x_t	Input Node
h_t	Output Node
f_t	Forget Gate
i_t	Input Gate
o_t	Output Gate
C_t	Cell State
$\tilde{C}_t$	Alternative Value Vector
σ	Sigmoid Function
$tanh$	Tangent Function
m	Meter
v	Walking Speed
Nm	Newtonmeter
kg	Kilogram
r	Correlation Coefficient
$^\circ$	Degree

LIST OF ABBREVIATIONS

LLA	Lower Limb Amputation
GC	Gait Cycle
CP	Controlled Plantarflexion
CD	Controlled Dorsiflexion
PP	Powered Plantarflexion
SP	Swing Phase
EMG	Electromyography
MU	Motor Unit
MUAP	Motor Unit Action Potential
sEMG	Surface Electromyogram
nEMG	Needle Electromyogram
BH	Body Height
NN	Neural Network
ANN	Artificial Neural Network
TDNN	Time Delay Neural Networks
LSTM	Long Short Term Memory
TA	Tibialis Anterior
SO	Soleus
PL	Peroneus Longus
MG	Medial Gastrocnemius
RF	Rectus Femoris
BF	Biceps Femoris
VM	Vastus Medialis
GMax	Gluteus Maximus
RMSE	Root Mean Square Error
SPM	Statistical Parametric Mapping
IEMG	Integrated Electromyogram
MAV	Mean Absolute Value

WAMP	Willison Amplitude
RMS	Root Mean Square
WL	Waveform Length

1. INTRODUCTION

1.1 Related Literature

1.1.1 Lower Limb Amputations and Prostheses

Lower limb amputation (LLA) is the partial or total removal of a limb due to a disease, accident, or trauma. The most commonly seen types of LLA include transtibial amputation, which entails the surgical removal of the lower leg below the knee joint, and ankle-foot amputations, involving the surgical removal of the foot around the ankle joint (Figure 1.1). The incidence rates of these interventions are very high, with transtibial amputations accounting for approximately half of the LLAs reported in the UK between 2003 and 2013 [1], while in Canada, from 2006 to 2011, around 24% and 28% of total LLAs were categorized as transtibial and ankle-foot amputations, respectively [2]. The size and volume of residual limb muscles vary among amputees, based on the factors such as the cause of amputation and the surgical technique employed. Notably, in cases of transtibial amputation, if the amputation is closer to the knee, there is a significant reduction in the size and volume of residual limb muscles [3]. Conversely, in ankle-foot amputation, a larger proportion of the muscle mass tends to remain intact [4].

The assistive robotics aiming to restore the locomotion of individuals suffering from LLAs has notably improved with the recent advancements in hardware and software development. The first examples of such systems are energetically passive prosthetic devices that have been in use for many years and continue to dominate the market of commercial prostheses owing to their relative simplicity, low cost, and robust design. These devices use passive components such as springs and dampers, and with recent advances in new materials such as carbon composite have improved the hardware allowing the entire device to flex, absorb, and return energy with a flexible carbon fiber shaft and a heel spring (e.g., Figure 1.2A) [5]. However, the human ankle performs more positive mechanical work than negative and has a greater peak power

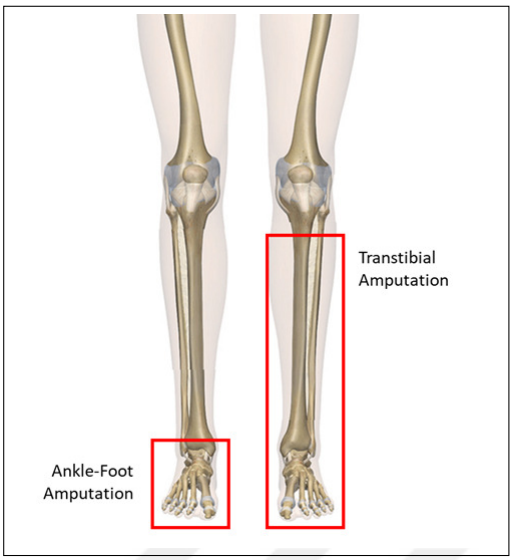


Figure 1.1 Transtibial and ankle-foot amputations.

over the stance period, especially at moderate to fast walking speeds [6]. Therefore, although passive prostheses provide a good approximation of the ankle's function, passive prostheses are not able to provide adequate energy for forward propulsion during the push-off. Therefore, compared to able-bodied individuals, amputees using passive prostheses expend 20% - 30% more energy while walking [7] due to the passive prostheses' limitations in generating mechanical power, their inability to autonomously adapt, and their lack of sensory feedback.

Recent advances in robotic technology especially in actuation, energy storage, miniaturized sensing, and embedded computing led to the development of powered prostheses that improves the ambulation for amputees [8]. These are size and weight vises comparable to actual human ankle-foot and consist of an actuator and a battery to provide external power required during walking (e.g., Figure 1.2B) [9,10]. Therefore, powered prostheses result in lower metabolic costs compared to passive prostheses [11] and are able to provide locomotion beyond slow walking speeds [12]. However, the use of an actuator raises the issue of robotic control [12]. Despite the availability of algorithms providing torque control, the majority of robotic control approaches still lack the ability for autonomous adaptation which serves for the sake of a natural and seamless ambulation [13].

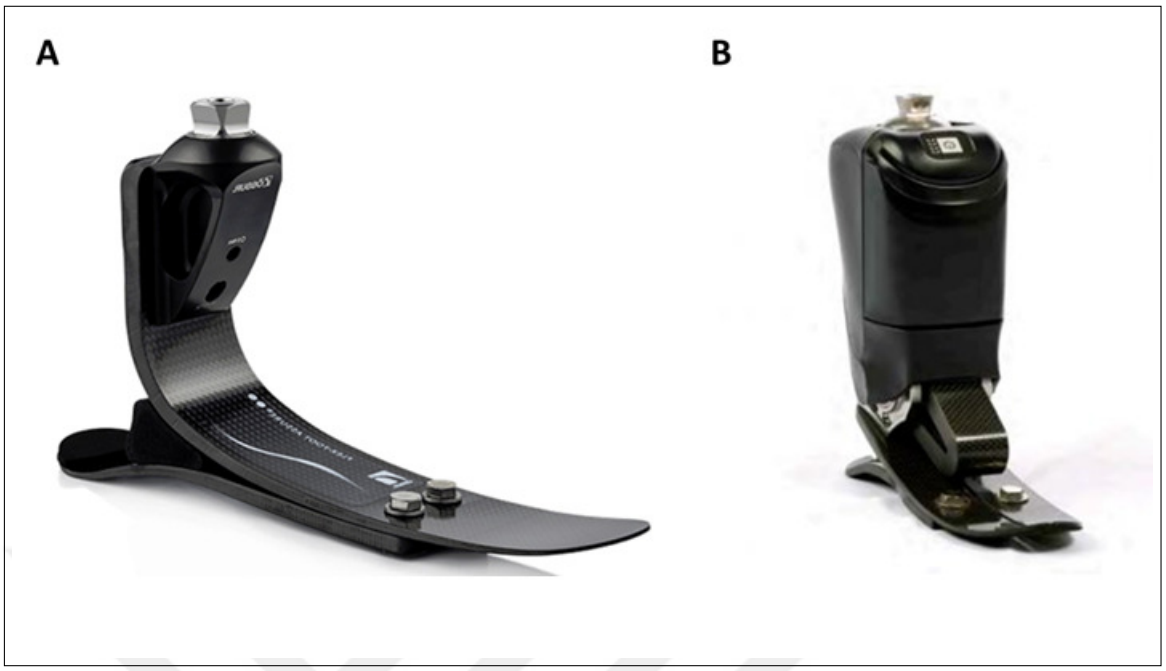


Figure 1.2 Examples of lower limb prostheses. In (A) and (B), the Flex-Feet by Össur (Reykjavik, Iceland) and the Empower by Ottobock (Duderstadt, Germany) are presented as examples of energetically passive and powered prostheses, respectively.

1.1.2 Human Ankle Biomechanics

Walking is an essential movement in daily life that combines the functionalities of a variety of muscles allowing people to keep their balance and move their bodies. Although it is a straightforward activity for able-bodied, it is challenging for people who underwent LLA [14]. Prosthesis development is being focused on enabling amputees to successfully improve their functionalities. However, many prostheses can not fully mimic the function of unimpaired joints, causing gait deviations [15]. In order to successfully mimic the ankle joint function, the predictions of ankle position and moment during level walking are crucial [15].

A gait cycle (GC) is defined as a sequence of repetitive events that occur during locomotion, starting from the initial contact of a foot with the ground and continuing until its subsequent contact [17]. The main sub-phases of the GC are (i) the stance phase, which represents the 60% of the GC while the foot makes contact with the

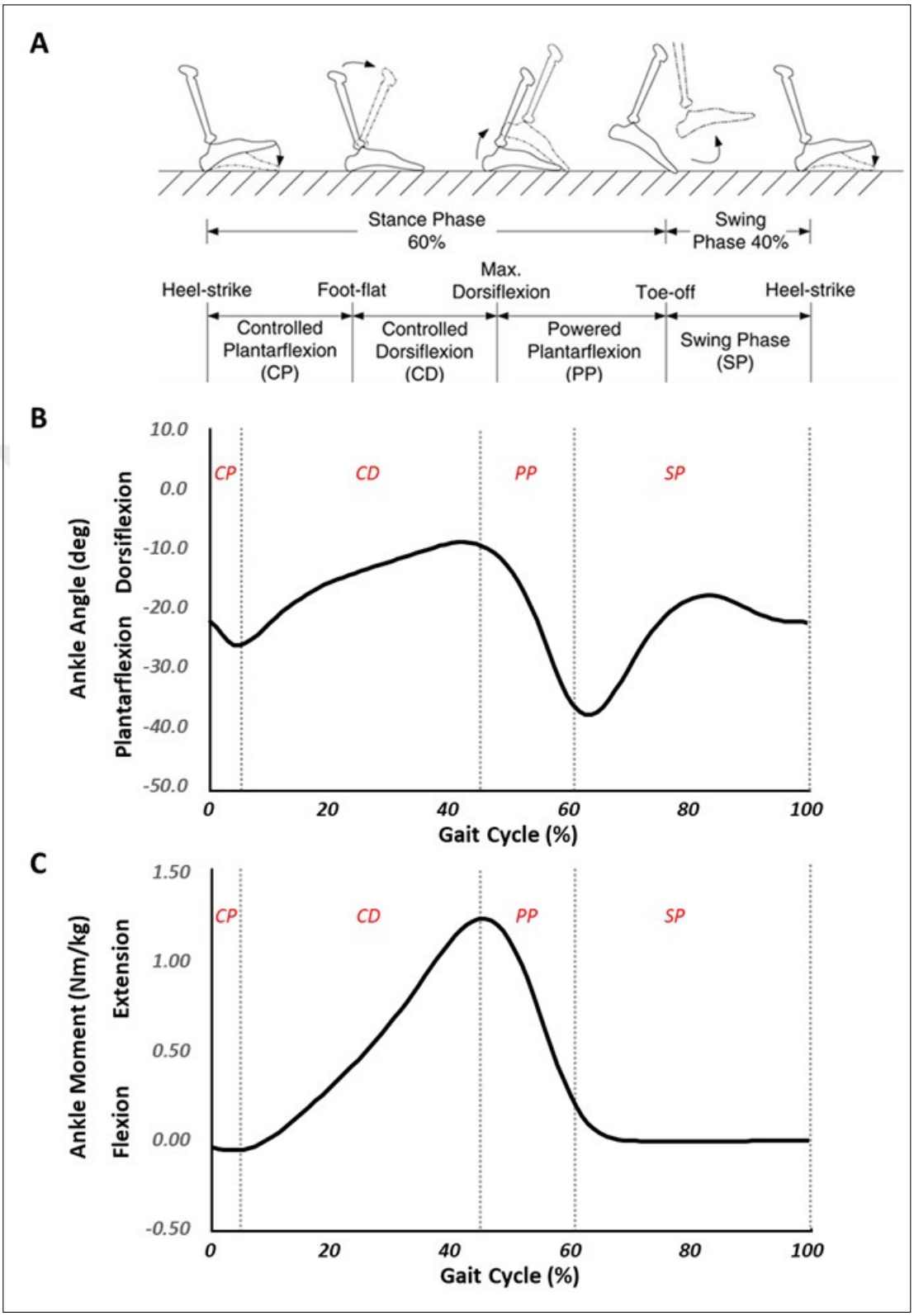


Figure 1.3 Human ankle biomechanics for level walking. In (A), a description of human ankle biomechanics is provided as a function of %GC, according to [10]. In (B) and (C), representative plots of ankle angle and moment for level walking are provided versus %GC for a normal healthy individual walking at a self-selected speed [16]. Ankle moment is normalized by body mass. 0% corresponds to the heel strike and 100% to the heel strike of the same leg.

ground, and (ii) the swing phase (SP), which represents the 40% of the GC while the foot is off the ground [10]. According to [10], the stance phase of level walking is divided into three sub-phases: Controlled Plantarflexion (CP), Controlled Dorsiflexion (CD), and Powered Plantarflexion (PP) (Figure 1.3A).

The CP is the first sub-phase beginning at the heel strike and continuing until the foot is flat. During this sub-phase, the heel and the foot make initial contact with the ground. Ankle moment is proportional to ankle position [10]. The CD begins at foot-flat and continues until the ankle reaches the maximum dorsiflexion. Within this sub-phase, elastic energy is stored for helping propel the body during the phase of PP [10]. The PP begins after CD and ends at the toe-off. Plantarflexors concentrically produce ankle power, propelling the body forward [15]. The SW begins at the toe-off and ends at the heel strike. It represents the portion of the gait cycle when the foot is off the ground. Dorsiflexion of the foot occurs, aiding toe clearance [15].

The total range of motion of the ankle joint approaches 90 degrees, however, during level walking, the entire range of motion is around 30 degrees [18]. As shown in Figure 1.3B, at heel-strike the ankle is slightly plantarflexed and as the body moves over the supporting foot, the ankle starts dorsiflexion. Just prior to SP, the ankle once again becomes plantarflexed. During the SP, there is a second wave of dorsiflexion, which ensures clearance between the toes and the ground. Towards the end of the SP, the ankle becomes plantarflexed prior to heel-strike [18–20].

The ankle moment variation during the gait is demonstrated in Figure 1.3C. To provide a controlled foot rotation, ankle moment is started to be generated after the heel strike. When the foot is flat, the ankle moment is at the maximum with the contractions of plantarflexors. Consequently, the body starts to move forward. Ankle moment occurs until the SP [21–23].

1.1.3 Electromyogram Signal

Electromyography (EMG) is an electrodiagnostic technique used for measuring the response of a muscle in response to nerve stimulation [24]. The EMG signal generation involves a complex biological process consisting of the interaction between the nervous system and muscle fibers [25] (Figure 1.4). Skeletal muscles consist of multiple individual muscle fibers that are stimulated by motor neurons which are nerve cells that control muscle movements and conduct signals from the brain or spinal cord to the muscle [26]. The combination of an individual motor neuron and all of the muscle fibers that it innervates is called a motor unit (MU) [26], and the electrical activity generated from a MU is the motor unit action potential (MUAP) [27]. Upon the arrival of the electrical impulse, the MUs depolarize the cell membrane space of their respective axon terminals, leading to an action potential propagation traveling across the muscle fibers [28]. Considering that an activation impulse may recruit multiple MUs, all the resultant MUAPs become superimposed to form the EMG signal [28] (Figure 1.4). These can be recorded using a surface electrode (non-invasive) that can be placed on the skin close to the target muscle, i.e., surface EMG (sEMG), or by a needle electrode (invasive) inserted in the muscle, i.e., needle EMG (nEMG), [25].

Recent studies have demonstrated the feasibility of using lower extremity sEMG signals for powered ankle prosthesis control in order to achieve natural and seamless ambulation. These also indicated the potential use of sEMG signals in predicting joint kinetics and kinematics [29–33]. Nevertheless, the utilization of sEMG signal presents challenges due to its complexity [34,35]. In order to address these challenges, processing implementations such as normalization and feature extraction have been widely used (e.g., [36]).

Normalization is a technique used to facilitate the comparison of sEMG signals collected from a muscle under various conditions, as well as to compare sEMG activity between different muscles. It provides accurate comparison and interpretation across different individuals and conditions [35]. In normalization, the choice of the reference value to which to normalize the sEMG signals is critical because it should have high

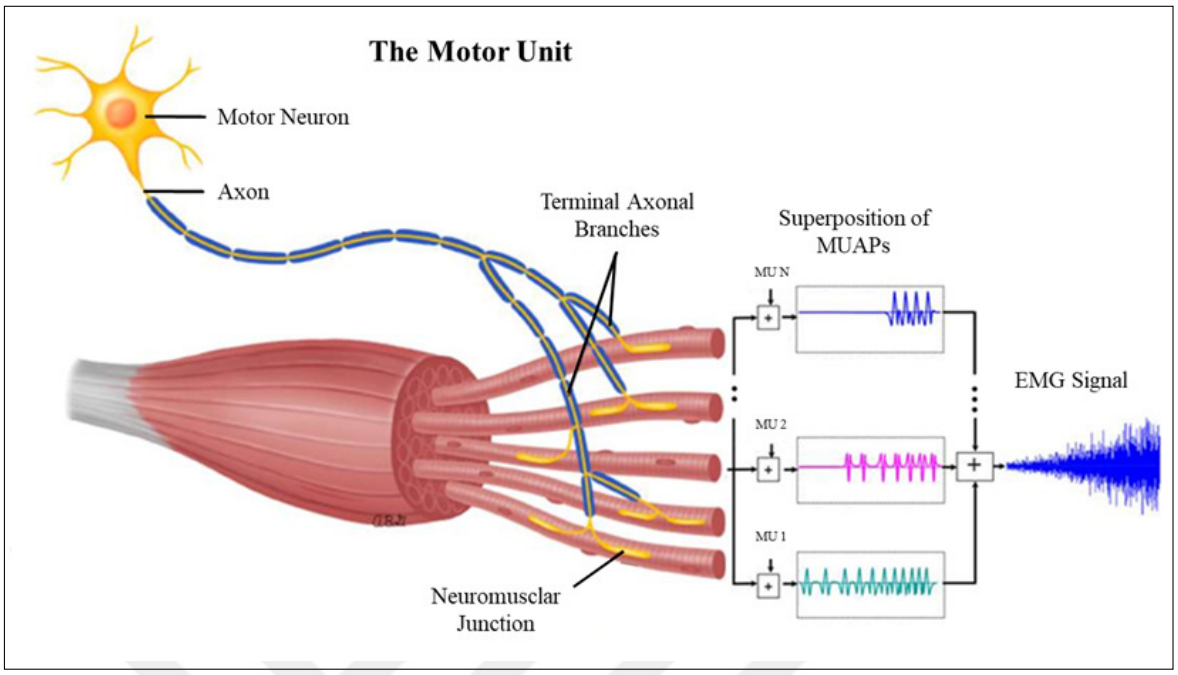


Figure 1.4 A motor unit and the muscle fibers it innervates, according to [28]. When a motor neuron is stimulated, all muscle fibers that it innervates depolarize synchronously to generate a MUAP. Action potentials superimpose to form the EMG signal.

repeatability [37]. Additionally, the choice of the normalization method holds significant importance as it impacts the amplitude and pattern of the normalized sEMG signal [37]. The most commonly used methods to obtain the reference value are (i) determining the maximum activation level during maximum voluntary contraction and (ii) calculating the peak or mean activation level during a specific task [35]. However, the implementation of a real-time amplitude normalization brings additional challenges during the reference value determination and elevates computational cost because of the necessity of the periodic calibration disturbing the real-time use [38]. Additionally, sEMG signal change due to fatigue and walking speeds can misrepresent the reference value over longer periods [39–42] and make the amplitude normalization unsuitable for real-time processing [38].

The feature extraction technique is used to reduce the dimensionality of the signal while preserving and enhancing important information for further analysis. This is done by analyzing the signal within a time segment known as a window. The length of the window determines the temporal resolution of the features to be extracted [43]. The

feature extraction of sEMG signals involves the analysis of the signal within successive overlapping or non-overlapping windows of fixed duration. The overlapping window provides smooth transitions between adjacent windows, whereas non-overlapping windows simplify the processing (Figure 1.5). Within each window, specific information relevant to the application can be extracted and used for further analysis. The features are generally classified into two domains: frequency and time domain features. Frequency domain features require transforming the sEMG signal within the window into the frequency domain using techniques such as Fourier transform or wavelet transform, elevating the computational complexity [44]. Features such as power spectrum density, frequency ratio, and peak frequency can be extracted from the frequency domain [44]. On the contrary, time domain features involve analyzing the sEMG signal in the time domain extracting statistical parameters such as mean, root mean square, waveform length, and zero crossing. Therefore, these features do not require any transformation, consequently, are widely used in research and practice due to their low computational complexity [44].

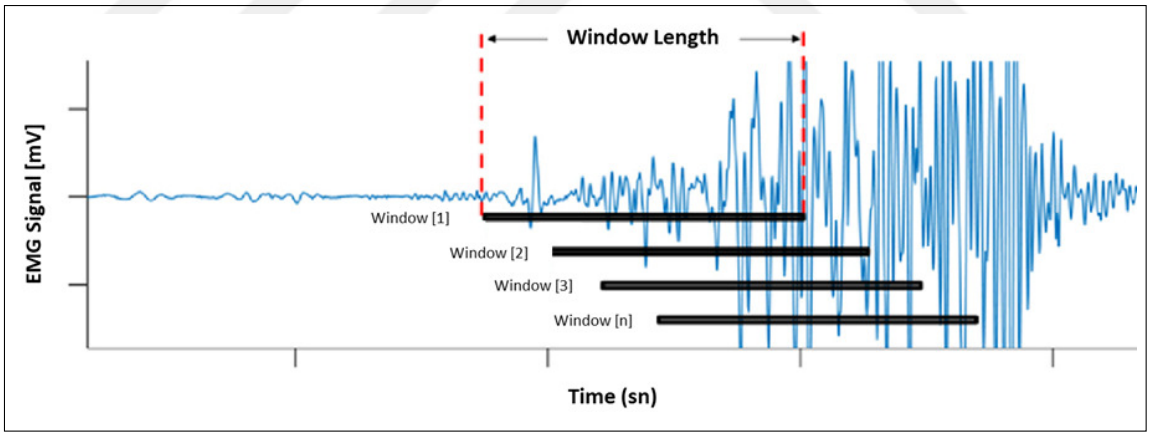


Figure 1.5 The representation of the sliding window for feature extraction [45].

1.1.4 Neural Network Structures

There is a variety of algorithms and infrastructures that have been employed to predict lower limb joint kinetics and kinematics using sEMG signals. Biomimetic models (e.g., [9, 46, 47]), and artificial neural networks (ANNs) including machine learning (e.g., [48–51]), and deep learning architectures (e.g., [52–54]) are commonly utilized

ones. Biomimetic models, despite their efficiency, have drawbacks including complexity, reliance on assumptions, calibration requirements, limited adaptability to different movements, and potential computational demands [55]. Therefore, ANNs have started to be used widely.

ANNs are mathematical models inspired by the architecture and functioning of the biological nervous system and the fundamental unit of the nervous system is the neuron which performs simple tasks like generating a response to an input. A biological neuron consists of dendrites, a nucleus (cell body), and an axon as shown in Figure 1.6. The dendrites are extensions that are connected to the cell body and receive signals from neighboring neurons, whereas the axon is the transmitter of the neuron, sending signals to neighboring neurons. The connection between two neighboring neurons is called a synapse which enables communication [56]. The neuron output is determined within the nucleus based on the cellular assessment of received stimulations. If the total excitation caused by electrochemical signals exceeds a threshold, an action potential is generated for stimulating neighboring neurons, muscles, or glands. Thus, the information is transmitted from one neuron to another [57].

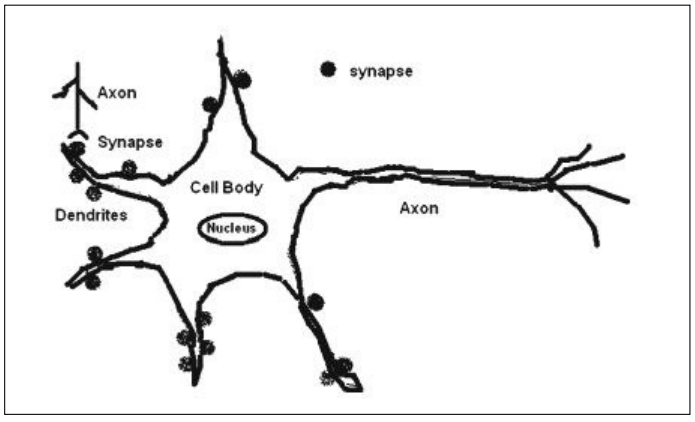


Figure 1.6 A sketch of biological neuron, according to [56].

Similar to the biological nervous system, ANN is formed with the interconnection of nodes and the fundamental unit is the artificial neuron 1.7. Each neuron receives multiple inputs via connections associated with weights, analogous to the strength of the synapse. Additionally, a bias can be defined to offset the output, allowing the

activation function to shift toward the positive or negative side. When the weighted sum of the inputs exceeds the threshold value of the neuron, the signal is passed to output through an activation function, which determines the functional behavior of the neuron. Accordingly, the information is transmitted from one to another [58].

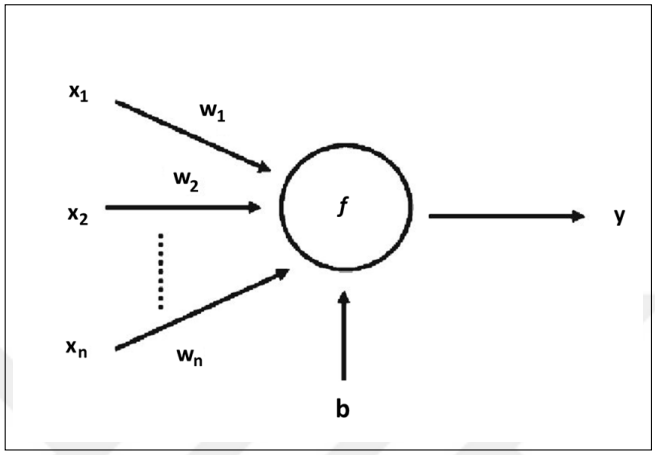


Figure 1.7 A basic model of a single artificial neuron: x_i = input, w_i = weight, b = bias input , f = transfer function, y = output, according to [56].

The mathematical representation of an artificial neuron output is given in Eq.1.1.

$$y = f\left(\sum_{j=1}^{m}(x_j w_j + b)\right) \tag{1.1}$$

An ANN is constructed by interconnected neurons, becoming a powerful tool where the complexity of a data or task makes the design of a model by hand impracticable [58]. Figure 1.8 shows an example of an ANN in which all neurons are interconnected. The ANN has three inputs (x_1, x_2 and x_3) and one output (y), consequently three neurons and one neuron in the input and output layers, respectively. The weights, biases, and activation functions of each neuron are given as w_i, b_i and f_i. The mathematical representation of such an ANN output is given in Eq. 1.2.

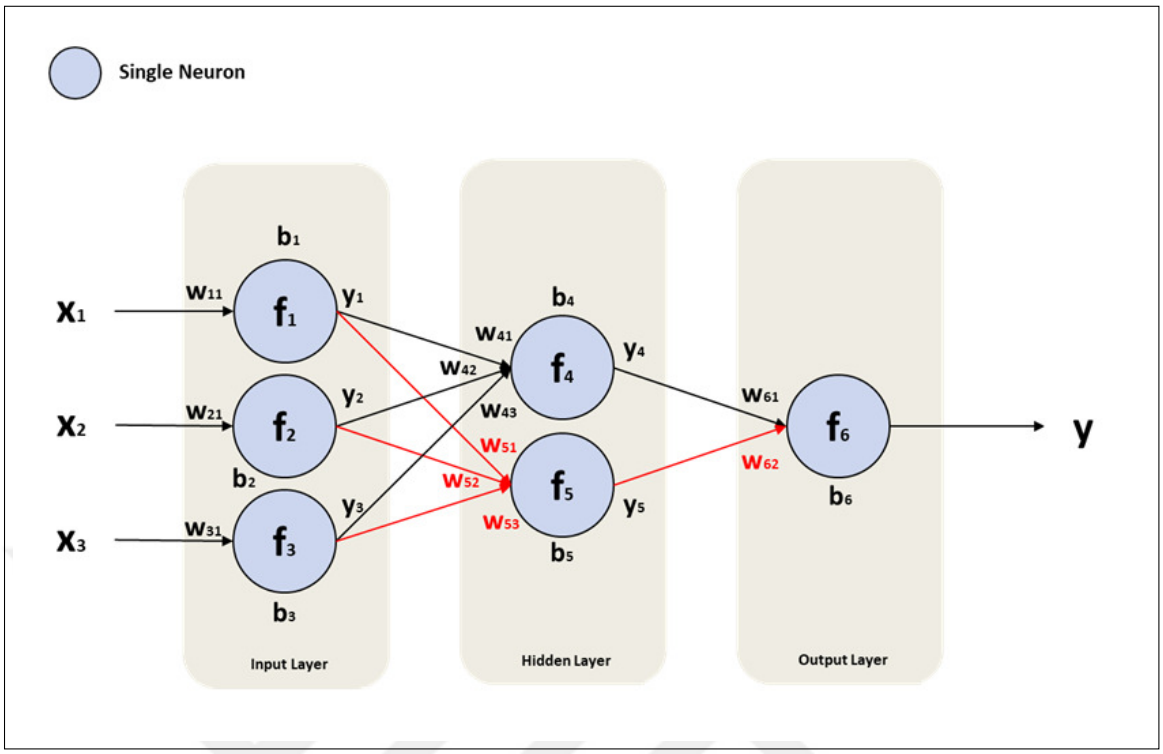


Figure 1.8 An example of an ANN with one hidden layer: x_i = neuron input, w_i = neuron weight, b_i = neuron bias, f_i = neuron transfer function, y_i = neuron output, y = ANN output.

$$
\begin{aligned}
y = f_6 \cdot \Bigg(f_4 \cdot \Big(f_1 \cdot (x_1 w_{11} + b_1) \cdot w_{41} + f_2 \cdot (x_2 w_{21} + b_2) \cdot w_{42} + \\
f_3 \cdot (x_3 w_{31} + b_3) \cdot w_{43} + b_4 \Big) \cdot w_{61} + \\
f_5 \cdot \Big(f_1 \cdot (x_1 w_{11} + b_1) \cdot w_{51} + f_2 \cdot (x_2 w_{21} + b_2) \cdot w_{52} + \\
f_3 \cdot (x_3 w_{31} + b_3) \cdot w_{53} + b_5 \Big) \cdot w_{62} + b_6 \Bigg)
\end{aligned}
\tag{1.2}
$$

Despite the efficiency of traditional ANN in joint kinetic and kinematic estimation by utilizing sEMG signals (e.g., [59]), Souza et al., [60] argued that neuromuscular control schemes merging timing-based approaches could advance the control of powered prostheses. Therefore, the use of architectures such as time-delay neural networks (TDNN) and long short-term memory (LSTM) have been escalated.

TDNN is an extended multilayer ANN architecture designed to handle patterns of time-varying signals [61]. The TDNN is based on the use of time delays, enabling neurons to store the history of input signals. In order to achieve that, each neuron is given the input values at different points in time (Figure 1.9). Thus, the TDNN is able to map a relationship between the current and the former input values during the output generation [61].

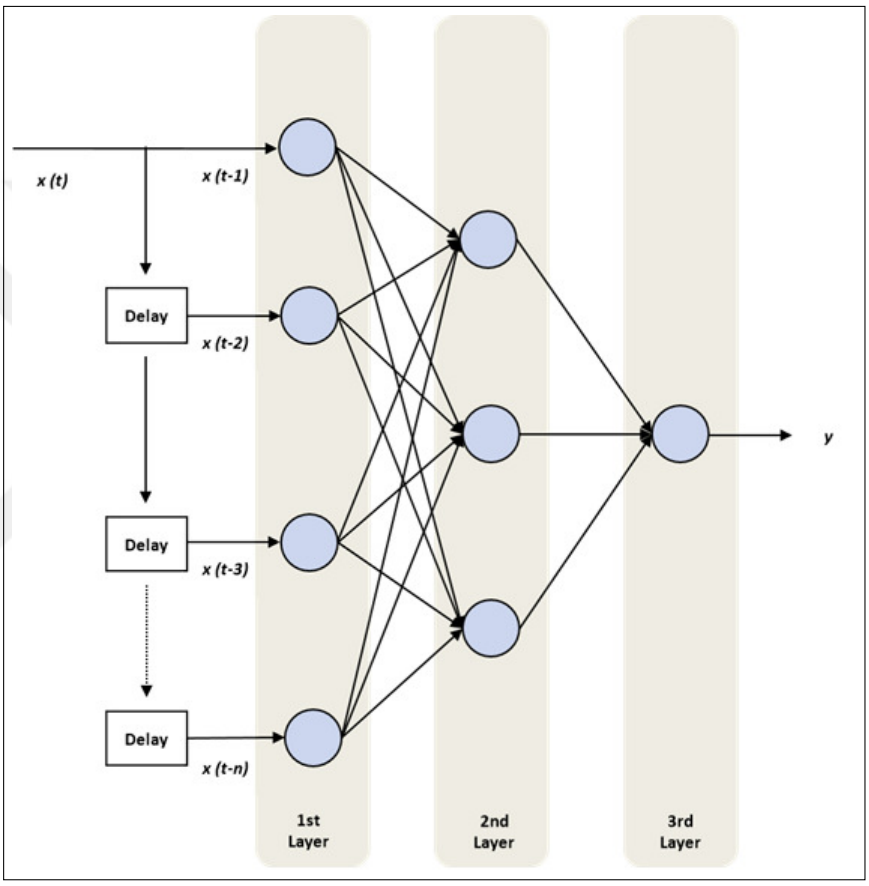


Figure 1.9 An illustration of a TDNN with multiple layers, according to [62]: *x(t)* = input, *x(t - 1:N)* = previous values of *x(t)* until nth sample.

The equation representing the output of the TDNN with n time delays can be seen in Eq. 1.3, where *x(t)* represents the input and *y(t)* denotes the output at a specific time t.

$$y(t) = f\left(x(t), x(t-1), x(t-2), x(t-3), ..., x(t-n) \right) \tag{1.3}$$

LSTM is a deep learning method that is a form of recurrent neural network architecture. Among deep learning models, LSTM has been reported as one of the most effective architectures for predicting time-series data [54]. LSTM is capable of selectively remembering patterns that represent a duration of time [63]. The memory structure can update the information across time to decide what to remember, what to forget, and what to output [54]. This is done with the cell state and corresponding gates within the LSTM called input, output, and forget gates. Cell state allows the information of previous time steps to be carried on to later time steps. As sequence data flows, gates remove or add information to the cell state. The input gate updates the cell state, whereas the output gate determines the hidden state. Forget gate decides which information will be kept or removed [64]. Figure 1.10 shows an illustration of the principle, whereas the mathematical representation of the described process is in Eq. 1.4 - 1.9.

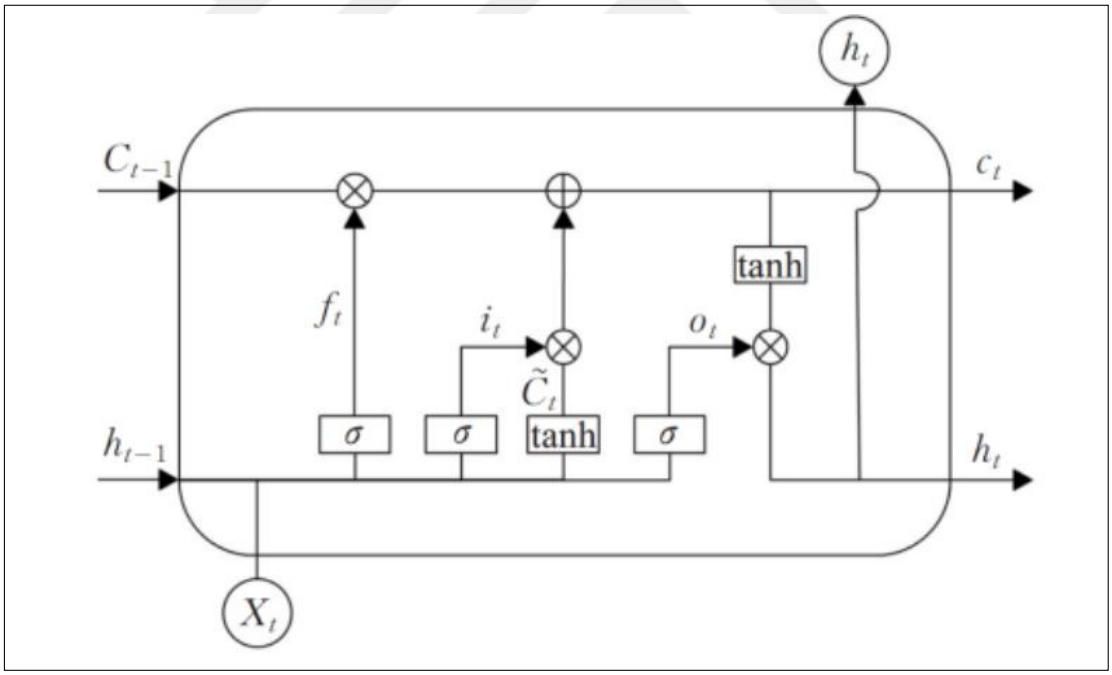


Figure 1.10 Inner structure of LSTM unit, according to [65].

$$f_t = \sigma\big(w_f \cdot [h_{t-1}, x_t] + b_f\big) \tag{1.4}$$

$$i_t = \sigma\big(w_i \cdot [h_{t-1}, x_t] + b_i\big) \tag{1.5}$$

$$\tilde{C}_t = tanh\big(w_c \cdot [h_{t-1}, x_t] + b_c\big) \tag{1.6}$$

$$C_t = f_t \cdot C_{t-1} + i_t \cdot \tilde{C}_t \tag{1.7}$$

$$o_t = \sigma\big(w_o \cdot [h_{t-1}, x_t] + b_o\big) \tag{1.8}$$

$$h_t = o_t \cdot tanh\big(C_t\big) \tag{1.9}$$

f_t, i_t, C_t, and o_t represent forget gate, input gate, cell state, and output gate at time t. w_f, w_i, w_c, and w_o respectively represents the corresponding weights of gates in different states. b_f, b_i, b_c, and b_o represents the corresponding biasing of doors in different states respectively. x_t and h_t represent the input and output of the current node. $\tilde{C}_t$ represents the new alternative value vector in the calculation process. σ and $tanh$ represent the sigmoid and tangent functions.

1.2 Outline of the Thesis

1.2.1 Aim of the Study

The main aim of the thesis was to develop a neural network-based algorithm to predict sagittal ankle position and moment during level walking in silico by utilizing sEMG signals of lower limb muscles and to conduct offline tests for the validation of the results. In the development, the real-time applicability of the algorithm was prioritized. Therefore, we avoided the implementations demanding high computational complexity, while targeting the optimal muscle selection. The specific aims of this research were as follows:

1. Develop a neural network-based algorithm infrastructure to predict ankle position and moment during ground-level walking by utilizing normalized sEMG amplitudes.
2. Develop a methodology to objectively evaluate the performance of all possible muscle combinations as sensor inputs, and rank them according to targeted success definitions, in such a way that this methodology can facilitate a patient specific sensor input selection in later applications.
3. Develop a neural network-based algorithm infrastructure to predict ankle position and moment during ground-level walking by utilizing time-domain features extracted from non-normalized sEMG amplitudes.
4. Optimize and cross-validate the proposed overall structure to ensure its efficiency and repeatability in predicting ankle position and moment.

1.2.2 Overview

The aims of the thesis addressed in the following chapters are:

Chapter 2, entitled *"Development of a Neural Network-based Control Algorithm for Powered Ankle Prosthesis"* addresses the first aim. A time delay feed-forward multilayer neural network architecture is developed by utilizing normalized surface electromyography amplitudes. The performance of the five lower limb muscles is thoroughly evaluated, and a ranking list based on their prediction accuracy is provided.

Chapter 3, entitled *"The Use of non-normalized Surface Emg and Feature Inputs for LSTM-based Powered Ankle Prosthesis Control Algorithm Development"* addresses the second and third aim. A long short-term memory neural network architecture is developed by utilizing time-domain features extracted from non-normalized surface electromyography amplitudes. The performance of the five time-domain features and eight lower limb muscles are respectively evaluated, and ranking lists based on their respective prediction accuracies are provided.

Chapter 4, entitled *"The Optimization of the LSTM-based Ankle Position and Moment Predictor"* addresses the fourth aim. Building upon the findings of Chapters 2 and 3, the feature extraction is optimized, and the overall neural network structure is cross-validated.

1.3 List of Publications Resulting from the Thesis

1.3.1 Journal Articles

1. "Development of a neural network based control algorithm for powered ankle prosthesis", A. D. Keles, and C. A. Yucesoy, *Journal of Biomechanics*, Vol. 113, 110087, 2020.

2. "The use of non-normalized surface EMG and feature inputs for LSTM-based powered ankle prosthesis control algorithm development", A. D. Keles, R. T. Turksoy, and C. A. Yucesoy, *Frontiers in Neuroscience*, Vol. 17, 1158280, 2023.

1.3.2 Conference Proceedings

1. "Development of a neural network based active ankle prosthesis algorithm to address amputation level and minimum sensor requirements", A. D. Keles, and C. A. Yucesoy, The 8^{th} World Congress of Biomechanics (WCB). Dublin, Ireland, 2018.

2. "A neural network based active ankle prosthesis algorithm to minimize sensor requirements accommodating different amputation levels", A. D. Keles, and C. A. Yucesoy, The 9^{th} International Biomechanics Congress. Eskişehir, Turkey, 2018.

3. "Developing a neural network-based active ankle prosthesis algorithm that minimizes emg and eliminates force sensors", A. D. Keles, and C. A. Yucesoy, The 28th Annual Meeting of the European Society for Movement Analysis in Adults and Children (ESMAC). Amsterdam, The Netherlands. *Gait & Posture*, Vol. 73, Suppl 1, pp. 340-341, 2019.

2. DEVELOPMENT OF A NEURAL NETWORK-BASED CONTROL ALGORITHM FOR POWERED ANKLE PROSTHESIS

2.1 Introduction

Recent technological developments particularly in embedded computing, sensors, and batteries have advanced the field of assistive robotics to restore legged locomotion for individuals suffering from lower limb amputations [66]. The first examples of assistive devices were energy-storing and return prosthetics, which provided a great improvement over purely passive prostheses with and without joints and are being used successfully, still dominating the commercial lower limb prostheses currently available. Owing to their relative simplicity, low cost, and robust design, these devices are practical tools to enable the functional recovery of gait pathologies stemming from several conditions. Passive elastic energy storage and return ankle prostheses restore some ankle function, but especially in fast walking external energy input is necessary to achieve close to normal gait patterns. Their inherent shortcomings include the inability to generate positive mechanical power and lacking autonomous adaptation to the user's changing needs [8, 67].

Recently, powered prostheses have been developed to assist normal gait beyond slow walking speeds [68–70]. Surface electromyograms (sEMG) assist the prediction of joint position and moment changes [51, 71], and are used to control assistive robotic systems [72–75]. Biomimetic models, neural networks, fuzzy logic, and genetic algorithms are used for sEMG classification [76]. Sepulveda et al. [57] developed a neural network with the back-propagation algorithm to model the relationship between muscle activity and joint motion. Note that, sEMG is influenced by noise due to, e.g., crosstalk, changes in skin conductivity, and artifacts originating from, e.g., movement at the skin-electrode interface and signal amplifiers [77]. As the condition of the remaining lower leg muscles strongly depends on the type of amputation surgery performed and

the trauma experienced, the sEMG signal quality varies from patient to patient. Unlike in ankle disarticulation, which does not interfere with lower leg muscles, less lower leg muscle mass remains intact in transtibial amputation. Moreover, amputation level in transtibial amputations differs among patients being performed near the knee or closer to the ankle. Therefore, minimizing the number of sEMG muscle sources utilized will make the powered prosthesis controller economic, and limiting the use of specifically the lower leg muscles will make it flexible ideally for both ankle disarticulation and transtibial amputation. However, for predicting position and moment changes in lower extremity joints via sEMG, Sepulveda et al. [57] used 16 muscles involving six lower leg muscles including extensor digitorum longus, peroneus longus, tibialis anterior, medial gastrocnemius, lateral gastrocnemius and soleus. Similarly, Zhang et al. [78] used five of those muscles to control an ankle exoskeleton (excluding the extensor digitorum longus). Au et al. [10] used additional force feedback to the sEMG of tibialis anterior, medial gastrocnemius, and lateral gastrocnemius to accurately estimate joint position however, the additional sensors required increased device cost and weight. Fleischer and Hommel, [74] utilized six upper leg muscles, but also force feedback, whereas Sup et al. [79] eliminated sEMG by using three force sensors instead. Therefore, current control algorithms for powered ankle prostheses utilize either a large number of sEMG sensors involving numerous lower leg muscles or several force sensors, or a combination. Development of a low-cost, user-friendly assistive powered ankle prosthetic device requires a flexible control algorithm, which can minimize sEMG sensors, and reduce the need for lower leg muscles while avoiding force sensors.

The aims of using healthy population data were to (1) test the feasibility of the neural network (NN) approach for developing a powered ankle prosthesis control algorithm that successfully predicts real-time sagittal ankle angle and moment during walking using exclusively lower limb sEMG, and (2) rank all muscle combination variations according to their success to determine the economic and flexible NN's.

2.2 Materials and Methods

2.2.1 Dataset

Gait data are required for developing, training, and testing NNs. For that purpose, sEMG amplitudes, sagittal ankle angle, and moment of walking trials were acquired from the open database by Bovi et al. [16]. In this database, data from forty able-bodied subjects were classified into two age groups: young (9 males, 11 females, 6-17 years, mean (SD) 10.8 (3.2) years, body height 1.47 (0.20) m) and adult (9 males, 11 females, 22-72 years, mean (SD) 43.1 (15.4) years, body height 1.71 (0.10) m). The subjects walked over level ground at a self-selected speed (normalized for body height (BH): adult 71.4 $\pm$ 10.2 and young 87.7 $\pm$ 15.8 %BH/s), and faster speeds (v) classified as very slow (v/BH $<$ 0.6), slow (0.6 $\leq$ v/BH $<$ 0.8), medium (0.8 $\leq$ v/BH $<$ 1), and fast (v/BH $>$ 1). Mean data of three trials per speed were utilized.

sEMG data of tibialis anterior (TA), medial gastrocnemius (MG), rectus femoris (RF), biceps femoris (BF) and gluteus maximus (GMax) were recorded unilaterally on the dominant side with electrode locations in agreement with SENIAM [80]. In a recent work by the same group [81], specifics of the sEMG acquisition were described: self-adhesive Ag-AgCl electrodes (Medtronic Kendall, USA, 24 mm electrode diameter, 10 mm active part diameter, bipolar configuration, 20 mm inter-electrode distance) were used and sEMG data were bandpass filtered (10-400 Hz) before sampling to reduce the aliasing effect. Bovi et al. [16] applied rectification and low-pass filtering (Butterworth 5th order, 3 Hz cutoff frequency). Additionally, sEMG data for each subject's channel individually was normalized for the maximum of the root mean square values of 2% intervals across each trial. Joint moments calculated using simultaneously collected gait data (SMART-E motion capture system, BTS, Italy utilizing total-body LAMB marker set and force plates, Kistler, Switzerland) were normalized by body mass. Data for each speed class per age group were averaged yielding a total of 10 datasets for further analyses.

2.2.2 Neural Network Development

All NNs developed feature the following: (1) A time delay feed-forward multi-layer NN architecture was used. This enables the networks to generate an sEMG-based continuous estimation of joint kinematics based on time-varying inputs [82, 83] and capability of accounting for the delay between the onset of EMG activity and mechanical movement [84]. (2) In addition to an input and an output layer, one hidden layer was used. This was shown to be sufficient for joint movement predictions [82, 83]. The hidden layer has 32 neurons with a nineteen-data-tapped delay. This was determined as the outcome of a systematical variation of the number of neurons and the time delay between 5-50 and 5-20, respectively yielding the highest correlations for ankle position and moment changes in the sagittal plane for five sEMG inputs. For each NN, a sigmoidal transfer function was used in the hidden layer. The number of neurons in the input layer varies according to the number of sEMG inputs. In the output layer, a linear transfer function was used so that the neural outputs could take on any value. A basic representation of the NN structure developed is shown in Figure 2.1A.

In order to predict the ankle position and moment, sEMG amplitudes of the following five lower extremity muscles were used as NN inputs: the TA and MG in the lower leg and the RF, BF, and GMax in the upper leg. To test the success of NN variations all possible muscle combinations were studied (in total 31: 5 single, 10 two, 10 three, 5 four, and 1 five muscle combinations).

The best-performing variations including (i) the minimum total number of muscle inputs and (ii) the smallest number of lower leg muscles were sought after. The former is referred to as the *economic variation* and the latter representing applicability for both amputation levels is referred to as the *flexible variation*. A variation including only upper leg muscles is classified as *ideally flexible*.

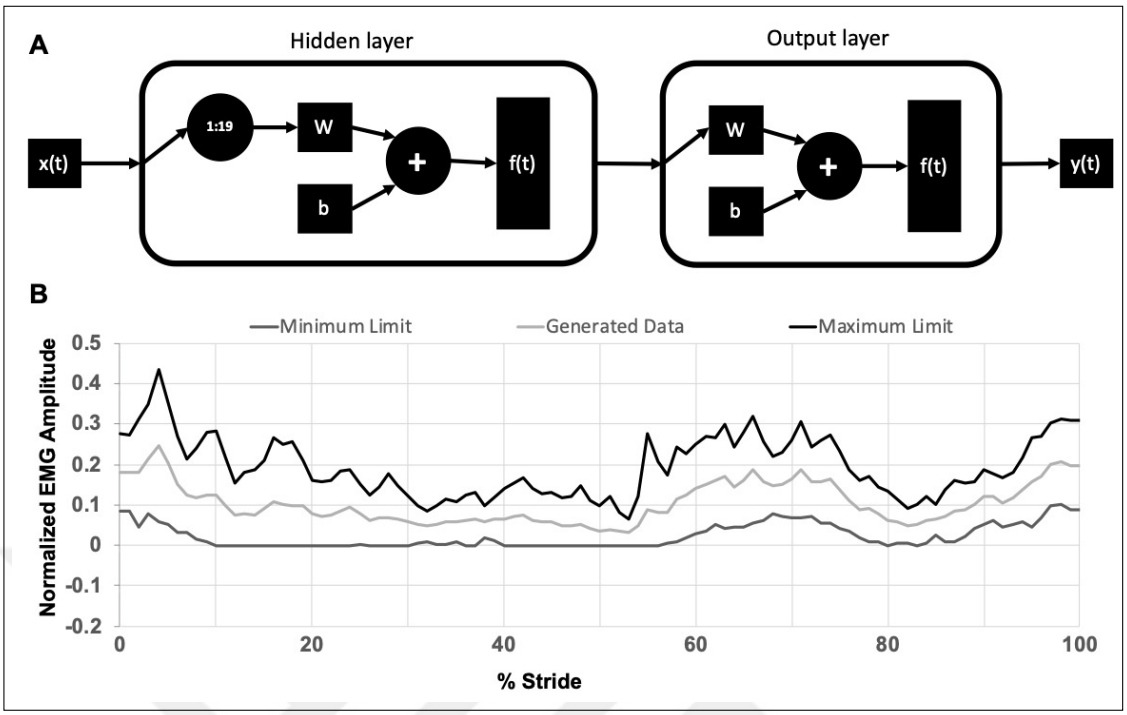


Figure 2.1 NN structure and data generation for training. (A) A basic representation of the proposed NN structure. *x(t)* and *y(t)* represent the sEMG amplitude and, position and moment estimations as NN inputs and outputs, respectively. *f(t)* represents the artificial neuron function specified for each layer (sigmoidal transfer function and linear transfer function in the hidden and output layer, respectively) in the NNs. (1:19) shows the nineteen-data-tapped delay in the hidden layer which has 32 neurons. The weight and bias of each neuron in the hidden and output layer are represented by w and b. (B) A sample normalized sEMG amplitude of the tibialis anterior (TA) muscle (medium speed, adult group): the maximum (black line), minimum (dark grey line), and a generated (light grey line) signal are shown.

2.2.3 Neural Network Training

2.2.3.1 Main and Versatility Implementations. The dataset involving five speed classes was split into training (four speed classes) and test (the remaining one speed class) datasets. The testing was first conducted on the *main implementation*: datasets for very slow, slow, medium, and fast speed classes were used in NN training, whereas those for self-selected speed class were used for testing. This was used to evaluate all NN variations. Subsequently, on the economic and flexible variations determined, *versatility implementations* were tested: for each of the very slow, slow, medium, and fast speed classes assessed for implementation, the remaining speed classes were used as training datasets (Table 2.1).

Table 2.1
Training and test datasets for the main and versatility implementations.

Main Implementation	
Training Datasets	**Test Dataset**
Very slow, Slow, Medium and Fast speed classes	Self-Selected speed class
Versatility Implementation	
Training Datasets	**Test Dataset**
Slow, Medium, Self-selected and Fast speed classes	Very slow speed class
Very slow, Medium, Self-selected and Fast speed classes	Slow speed class
Very slow, Slow, Self-selected and Fast speed classes	Medium speed class
Very slow, Slow, Medium and Self-selected speed classes	Fast speed class

2.2.3.2 Data Augmentation. Per each speed class, sEMG data of both young and adult groups were averaged per muscle. Therefore, out of the 10 datasets, a total of 8 training datasets were available for each implementation. However, in order to increase the training efficiency and to avoid its inadequacy (even five muscle combination in the main implementation yielded correlations <70% for both position and moment estimations), a protocol was devised for extending those and reproducing new training datasets. To do this, for each muscle input from each of the training datasets, three new ones were generated randomly, but by maintaining data distribution among the input and training datasets as bound by the minimum and maximum limits of data (Figure 2.1B). Consequently, the total number of training datasets was increased to 32. Possible bias in correlation assessment due to such data augmentation was avoided by applying magnitude warping and noise-adding techniques to sEMG data [85].

2.2.3.3 Training. Networks were trained in MATLAB by using the Bayesian regularization back-propagation algorithm, which is a supervised learning method that requires known, desired outputs for each input. The back-propagation algorithm updates the weight and bias values of each neuron in a NN according to Levenberg-Marquardt optimization. The algorithm minimizes a linear combination of squared errors and weights and subsequently determines optimal parameters for a NN structure that generates the desired outputs [86].

2.2.4 Evaluation of the Developed Neural Networks

To evaluate the outcome of the developed NN variations for joint position and moment, the following were used: (1) Pearson's correlation coefficient (r) between the actual and estimated outputs was calculated for the position (Pos Corr) and moment (Mom Corr) prediction and r = 0.95 was selected to represent the threshold for successful correlations (e.g., [49]). A miscorrelation score (MisCorr Score) was defined as the sum of the deviation of correlation values from one. (2) Root-mean-square errors (RMSE) between the actual and the estimated outputs were calculated for the position (Pos RMSE) and moment (Mom RMSE) prediction. An RMSE score was defined as the mean of position and moment RMSE values normalized to their respective peak value among all variations. (3) An overall error score was defined as the product of miscorrelation and RMSE scores.

2.2.4.1 Main Implementation. Using the overall error score, all variations were ranked and the economic and flexible variations were determined.

2.2.4.2 Versatility Implementation. Normal Q-Q plots for the residuals between original data and NN response were used to illustrate if the residuals follow a normal distribution. One-way ANOVA was used for temporal success assessment based on one-dimensional statistical parametric mapping (SPM) using F-statistics [87]. Differences between the original data and estimated outputs were considered significant at $P < 0.05$.

2.3 Results

2.3.1 Main Implementation

Table 2.2 shows correlation coefficients (see Appendix A for their visualization) and RMSE values of all variations, and provides their ranking based on their overall error score.

The five muscle combination (TA + MG + BF + RF + GMax) ranks 1^{st} amongst all variations ($r_{position}$ and $r_{moment} > 0.9850$).

Four muscle combinations: all variations show successful correlations ($r_{position}$ and $r_{moment} > 0.9720$) except TA + RF + BF + GMax.

Three muscle combinations: TA + MG + BF, TA + MG + RF, TA + MG + GMax, MG + BF + GMax and MG + RF + GMax show successful correlations ($r_{position}$ and $r_{moment} > 0.9540$). The remaining variations were unsuccessful.

Two muscle combinations show that only TA+MG ($r_{position} = 0.9520$, $r_{moment} = 0.9970$) yields successful correlations whereas, no NN comprised of a single muscle shows successful correlations.

Therefore, the economic variation is TA + MG + BF ($r_{position} = 0.9810$, $r_{moment} = 0.9960$). As all variations including only upper leg muscles were unsuccessful, no ideally flexible variation is possible, whereas the flexible variation is MG + BF + GMax ($r_{position} = 0.9550$, $r_{moment} = 0.9950$).

Table 2.2
The comparison of the NN variations. Shaded cells show unsuccessful variations. TA: tibialis anterior, MG: medial gastrocnemius, RF: rectus femoris, BF: biceps femoris, GMax: gluteus maximus, RMSE: root-mean-square error.

Rank	Muscle Variations	Pos Corr [r]	Mom Corr [r]	Pos RMSE [deg]	Mom RMSE [Nm/kg]	Overall Error Score
1	TA+MG+BF+RF+GMax	0.9870	0.9950	1.3880	0.0530	0.0030
2	TA+MG+RF+BF	0.9830	0.9950	1.4710	0.0400	0.0034
3	TA+MG+RF+GMax	0.9800	0.9970	1.4660	0.0430	0.0036
4	TA+MG+BF	0.9810	0.9960	1.5370	0.0380	0.0038
5	TA+MG+RF	0.9780	0.9940	1.5100	0.0470	0.0046
6	TA+MG+BF+GMax	0.9730	0.9960	1.9420	0.0420	0.0060
7	TA+MG+GMax	0.9730	0.9950	2.0710	0.0520	0.0068
8	MG+RF+BF+GMax	0.9740	0.9910	1.8430	0.0630	0.0075
9	MG+BF+GMax	0.9550	0.9950	2.2510	0.0420	0.0106
10	MG+RF+GMax	0.9600	0.9940	2.4660	0.0500	0.0111
11	TA+MG	0.9520	0.9970	2.3570	0.0410	0.0115
12	MG+RF+BF	0.9440	0.9950	2.6510	0.0510	0.0157
13	MG+RF	0.9070	0.9950	3.4720	0.0430	0.0296
14	MG+BF	0.9090	0.9910	3.1170	0.0630	0.0305
15	TA+RF+BF+GMax	0.9540	0.9410	2.2660	0.1490	0.0367

16	MG+GMax	0.8690	0.9950	3.4210	0.0430	0.0411
17	TA+BF	0.9350	0.9340	2.4610	0.1570	0.0491
18	TA+RF+GMax	0.9540	0.9190	2.3720	0.1710	0.0491
19	TA+RF+BF	0.9420	0.9210	2.6350	0.1600	0.0537
20	TA+BF+GMax	0.9330	0.9270	2.4660	0.1800	0.0570
21	TA	0.9210	0.9230	2.9260	0.1550	0.0635
22	MG	0.8210	0.9930	3.9310	0.0590	0.0664
23	TA+RF	0.9220	0.9130	3.0710	0.1760	0.0734
24	TA+GMax	0.9090	0.8680	3.0530	0.2020	0.1058
25	RF+BF	0.9010	0.8200	3.6010	0.2640	0.1656
26	RF+BF+GMax	0.8930	0.8150	3.6330	0.2500	0.1685
27	RF+GMax	0.7500	0.5940	5.1620	0.3380	0.5241
28	BF+GMax	0.6010	0.7270	6.0010	0.3040	0.5486
29	RF	0.5870	0.6390	5.8170	0.3250	0.6423
30	BF	0.4420	0.5360	5.7020	0.3740	0.9031
31	GMax	0.4100	0.3590	6.9540	0.3950	1.2302

2.3.2 Versatility Implementation

TA + MG + BF and MG + BF + GMax were able to produce estimation correlations above 0.950 for both position and moment (Table 2.3 and 2.4, respectively) after being subject to the implementation of very slow, slow, medium and fast speed classes. SPM showed no significant localized differences between the actual and estimated outputs for both TA + MG + BF (Figure 2.2) and MG + BF + GMax (Figure 2.3).

Table 2.3
TA+MG+BF versatility per different implementation datasets. TA: tibialis anterior, MG: medial gastrocnemius, BF: biceps femoris.

Implementation Dataset	Pos Corr [r]	Mom Corr [r]	Pos RMSE [deg]	Mom RMSE [Nm/kg]
Very Slow	0.9860	0.9980	1.3100	0.0250
Slow	0.9650	0.9950	2.0700	0.0460
Medium	0.9710	0.9850	2.3000	0.0900
Self-selected	0.9810	0.9960	1.5400	0.0380
Fast	0.9900	0.9970	1.1300	0.0320

Table 2.4
MG+BF+GMax versatility per different implementation datasets. MG: medial gastrocnemius, BF: biceps femoris, GMax: gluteus maximus.

Implementation Dataset	Pos Corr [r]	Mom Corr [r]	Pos RMSE [deg]	Mom RMSE [Nm/kg]
Very Slow	0.9750	0.9970	1.5800	0.0350
Slow	0.9740	0.9970	1.6600	0.0350
Medium	0.9810	0.9960	1.5900	0.0370
Self-selected	0.9810	0.9960	1.5400	0.0380
Fast	0.9740	0.9950	1.7000	0.0390

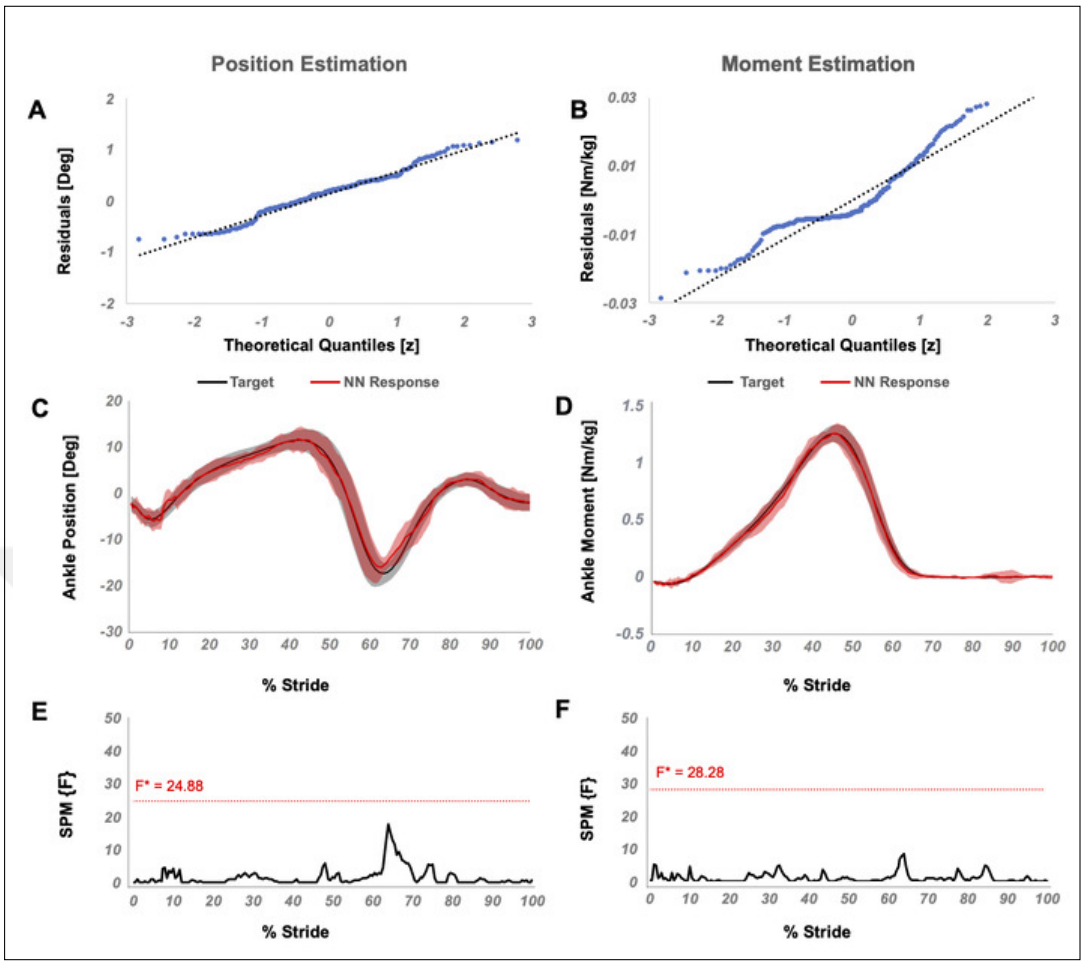


Figure 2.2 Temporal success assessment for TA + MG + BF. The normal Q-Q plots for the residuals between original data and estimated NN response for ankle (A) position and (B) moment. Mean and standard deviation of estimated NN response vs. original data for ankle (C) position and (D) moment, as a function of % stride. Statistical parametric mapping using F-statistics (SPMF) for the ankle (E) position and (F) moment as a function of % stride shows values below the threshold (i.e., for $P < 0.05$, $F^*_{position} = 24.88$, $F^*_{moment} = 28.28$). TA abbreviates tibialis anterior, MG abbreviates medial gastrocnemius and BF abbreviates biceps femoris muscles.

2.4 Discussion

Souza et al. [60] argued that the evolution of motorized knee and ankle components of powered prostheses has introduced a need for more advanced approaches to achieve prosthetic control. They also indicated that although myoelectric control schemes can be applied to the lower extremity, they must be merged with mechanical and timing-based control methods in order to achieve seamless and natural ambulation. Within this scope, contrary to the standard multilayer feed-forward NN approach, Rahmatian et al. [83] showed that by using time delay feed-forward multilayer NN with

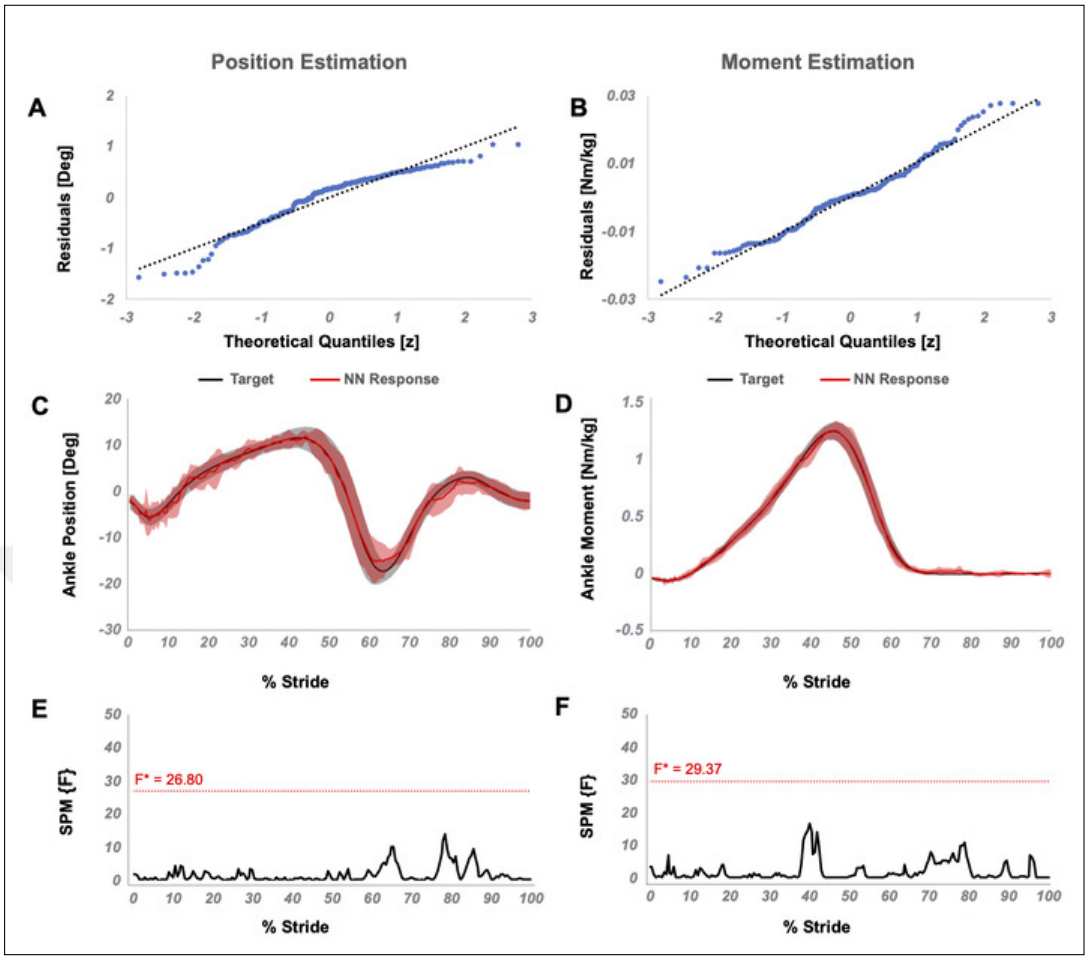


Figure 2.3 Temporal success assessment for MG + BF + GMax. The normal Q-Q plots for the residuals between original data and estimated neural NN response for ankle (A) position and (B) moment. Mean and standard deviation of estimated NN response vs. original data for ankle (C) position and (D) moment, as a function of % stride. Statistical parametric mapping using F-statistics (SPMF) for the ankle (E) position and (F) moment as a function of % stride shows values below the threshold (i.e., for $P < 0.05$, $F^*_{position} = 26.80$, $F^*_{moment} = 29.37$). MG abbreviates medial gastrocnemius, BF abbreviates biceps femoris and GMax abbreviates gluteus maximum muscles.

sEMG inputs collected from TA, MG, and lateral gastrocnemius muscles, the intended motion of a subject can be estimated. Although the detection of the ankle movements was not aimed at, that study showed that an accurate sEMG classification for the estimation of the ankle movement is plausible by using a shift-invariant classification. Also, Liu et al. [82] was able to achieve an sEMG-based continuous and simultaneous estimation of arm kinematics in able-bodied individuals and stroke survivors by using this type of NN. Based on such earlier indicated promise of that approach, a time delay feed-forward multilayer NN architecture that produces outputs using sequential inputs was implemented in the present study. The NNs developed to have 32 neu-

rons with a nineteen-data-tapped delay in their hidden layer, which allows accurate ankle movement estimations. Unlike previous studies [10, 74, 79, 88], the developed NN structure is capable of providing ankle movement estimations without the need for an extra mathematical model, a supportive NN or a force feedback implementation. Note that achieving 0.95 correlation in ankle position estimation, Chen et al. [49] reported an RMSE of 2.45°, and for 0.97 correlation in ankle moment estimation, Hahn and O'Keefe [89] reported an RMSE of 0.10 Nm/kg. However, they utilized 7-10 muscles. Utilizing only three muscles, our present algorithm yields 1.53°and 0.04 Nm/kg RMSE for over 0.98 correlation in position and moment estimations indicating compatible or improved success compared to previous studies.

A key use of sEMG amplitudes in the development of the powered prosthesis is to pre-determine the movement of the ankle during level ground walking. Bovi et al. [16] showed for different walking types that lower extremity muscles generate specific and consistent sEMG patterns in each gait cycle. Additionally, Huang and Ferris [3] showed that sEMG amplitudes of also upper leg muscles in transtibial amputations are consistent. They used sEMG of the residual limb muscles within the prosthetic socket limb interface as collected by surface electrodes. Their results support the potential use of myoelectric controllers for direct feed-forward control of powered prostheses. Consequently, sEMG was proven useful as control inputs for powered prostheses for an accurate prediction of the intended joint motion in terms of position and moment changes. However, elaboration on which muscles are to be utilized has been lacking. Au et al. [9, 10] used TA, soleus, MG, and lateral gastrocnemius muscles not only to estimate ankle movements in transtibial amputations but also to detect the locomotion task. Fleischer and Hommel [74] used RF, vastus medialis, vastus lateralis, semimembranosus, semitendinosus, and BF muscles to control a powered leg exoskeleton. Zhang et al. [78] designed a feed-forward NN model to control an ankle exoskeleton using sEMG amplitudes from TA, MG, soleus, lateral gastrocnemius, and peroneus longus muscles. Huang et al. [90] used sEMG amplitudes from sartorius, RF, vastus lateralis, vastus medialis, gracilis, biceps femoris long head, semitendinosus, biceps femoris short head, and adductor magnus to recognize locomotion modes for transfemoral amputees. Hargrove et al. [69] used semitendinosus, BF, tensor fasciae latae, RF, vastus later-

alis, vastus medialis, sartorius, adductor magnus, and gracilis to control a powered knee-ankle prosthetics. Spanias et al. [70] developed an intent recognition algorithm for a powered knee/ankle prosthesis using sEMG amplitudes collected from RF, tensor fasciae latae, semitendinosus, and adductor magnus. Nevertheless, none of those studies provided a specific reason other than their being activated during walking nor did a systematic analysis for the selection of the targeted muscles to be used as control inputs for their systems. Presently, possible combinations of TA and MG muscles in the lower leg and RF, BF, and GMax muscles in the upper leg were studied comprehensively. Note that despite its key role in ankle movement, collecting accurate sEMG data from the soleus can be problematic using surface electrodes. Hence, this muscle was excluded, which agrees with Huang and Ferris [3]. Those authors showed that the use of TA, MG, lateral gastrocnemius, vastus lateralis, RF, BF, and gluteus muscles' myoelectric signals provide successful control for robotic lower limb prostheses.

The present study shows the feasibility of the time delay feed-forward NNs for predicting ankle angle and moment using exclusively sEMG amplitudes for level walking of a healthy population. For the sake of minimizing the use of sEMG muscle sources, it is notable that the TA + MG combination alone yields successful correlations. The assessment showed that the *economic* variation i.e., the best-performing NN including the minimum total number of muscle inputs (TA + MG + BF) also involves those muscles. Another important finding is that the use of solely upper leg muscles is not feasible. However, successful three muscle combinations involving only the GMax were shown, with the *flexible* variation to minimize the number of lower leg muscles determined as MG + BF + GMax. Although the present findings are not directly transferrable to people with amputations or disease, they suggest that plausible NN variations exist for ankle disarticulation, confirmation of which requires specific studies. Yet, they also suggest that for a NN approach using exclusively sEMG amplitudes, involvement of lower leg muscles is inevitable for transtibial amputation. Note that, Huang and Ferris [3] showed in transtibial amputees that artifact-free and consistent sEMG can be recorded from lower leg muscles within the prosthetic socket-limb interface. However, in long-term use, walking with electrodes beneath the socket can compromise the comfort for persons with limb amputation, and the repeated applica-

tion of electrodes can affect the sensor lifetime adversely. Use of e.g., sEMG knit band sensor [91] can make implementation much easier and may help compromised comfort. On the other hand, high-density sEMG can help to avoid problems related to bipolar sEMG electrode placement and signals [92], and improve data quality [93,94]. Clites et al. [95] and Srinivasan et al. [96] showed that surgically constructed agonist-antagonist myoneural interfaces in the residual limb serve efficiently on torque-controlled tasks. This is promising for conceivable restoration of natural sensation to prosthetic joints, but targeted muscle re-innervation should be accounted for.

Commercially available powered ankle-foot prosthesis controllers are rare and improving the function in amputees is challenging. A neuromuscular model-based controller utilized in bionic ankle-foot prosthesis [97] is capable of normalizing gait during level walking for amputees. A bioinspired control algorithm has recently been proposed to provide adaptive control of level walking and stair ascent [13]. However, utilization of the provided power by the users with transtibial amputation, in a way to reduce the metabolic cost of motion requires care [98]. In addition, uphill and downhill walking as well as stair ascent/descent movements not only require more power [99,100], but also an improved leg work symmetry, and control over the contributions of ankle, knee, and hip joint work needs to be achieved [101, 102]. Therefore, more systematic work is necessary to improve powered ankle-foot prosthesis controllers. The present study aims at contributing to that with a neural network approach using sEMG as the sensor source, which requires additional studies and testing in amputees. Note that, the overall error score we used for ranking combines miscorrelation and RMSE between the actual and the estimated outputs into a single metric and takes ankle position and moment errors into account being equally weighted. This is suitable for our aim of testing the feasibility of the algorithms in the present development study conducted in a healthy population. However, uphill/downhill walking and stair ascent/descent movements and mobility of amputees may require differential weighting, which also needs to be studied.

Limitations of the developed methodology need to be addressed. Presently the NN structures developed and tested remain in reference to healthy individuals only.

The open database by Bovi et al. [16] involving suitably processed sEMG data of various muscles is very useful and is a rarity. However, although for level ground walking a sufficient number of data sets were available for NN training and implementation, this was limited to only two for toe-walking, heel-walking, step ascending, and step descending. Therefore, the NN-based control algorithm needs to be extended by the estimation of the intended movement after it is re-trained with a sufficient number of datasets for different locomotion tasks. The lack of an open database that consists of data on amputees limits further testing of the control algorithm developed. One plausible source of inconsistency is that the size of the residual limb, hence the volume of the lower leg muscles may differ across amputees. This hinders the use of a standard sEMG sensor placement, which yielded a low cross-correlation between sEMG patterns of transtibial amputees and controls particularly for the BF [3]. However, after determining suitable electrode locations using palpation, the authors successfully measured sEMG of TA, MG, and lateral gastrocnemius and four upper leg muscles of transtibial amputees during walking and reported that they were able to voluntarily activate their residual lower leg muscles with several of them producing activation profiles similar to healthy controls. Training their control algorithm using sEMG of the lateral gastrocnemius, MG, and TA in bilateral transtibial amputees, Au et al. [10] achieved ankle position and moment patterns comparable to those of a healthy subject during level ground walking. Similarly, Huang et al. [90] reported highly accurate powered prosthesis control by using sEMG of nine residual limb muscles of transfemoral amputees including the BF. The presently best-performing variation, TA + MG + BF may not therefore be prone to significant implementation problems, but this needs to be tested. However, the use of normalized sEMG data may bear difficulties for practical applicability in a real system, which imposes a major time limitation for the required computation. Yet, competent use of non-normalized sEMG in joint position and moment estimation has been reported e.g., in upper limb amputees [103]. Huang et al.'s [90] ankle movement estimation accuracy using non-normalized sEMG is comparable to our present findings. This is promising and limiting the preprocessing to bandpass filtering and rectification [10] is a more practical alternative. Overall, the accuracy of ankle movement estimations should be studied after re-training the developed control algorithm with a large database including non-normalized sEMG data

collected from lower extremity amputees.

2.5 Conclusion

A novel NN approach utilizing exclusively lower limb sEMG was developed. Its feasibility for predicting ankle angle and moment during level walking of a healthy population was evaluated comprehensively by testing all muscle combinations among TA, GMax, RF, BF, and MG muscles. NN variations TA + MG + BF and MG + BF + GMax showed the best predictive performances while minimizing the total number of muscle sEMG sources and minimizing the use of lower leg muscles, respectively. Following further development, this approach can be applicable in powered ankle prosthesis control algorithms. For this purpose, after extending their implementation with other movement types, the algorithms should be trained and tested for data acquired from amputees in new studies.

3. THE USE OF NON-NORMALIZED SURFACE EMG AND FEATURE INPUTS FOR LSTM-BASED POWERED ANKLE PROSTHESIS CONTROL ALGORITHM DEVELOPMENT

3.1 Introduction

Lower limb amputations include transtibial amputation i.e., a surgical procedure to fully remove the lower limb below the knee, and ankle disarticulation i.e., surgical removal of the foot at the ankle joint. The incidence rates of these interventions are high, reaching e.g., over 11500 cases alone in the UK each year [4], and from 2003 to 2013, about half of those were transtibial amputations [1]. Ascribed to a simple, low economic cost and robust design, energy storing and returning prostheses with elastic and damping characteristics [104] dominate the commercial lower limb prostheses market [105]. However, because of a lack of mechanical power generation and autonomous adaptation, they can only provide lower than normal gait speeds with high metabolic energy costs that lead to early fatigue [104, 106]. Central to these limitations is the absence of sensory feedback to characterize user-dependent needs [8].

Current studies on powered prostheses, which devices overcome the indicated shortcomings and assist users' gait at walking speeds close to normal [107] do utilize several sensors including inertial measurement units [68,108], pressure sensors [109,110], force sensors [79, 111, 112], and mechanical sensors e.g., load cells, position, velocity, and current sensors [70, 90, 113]. However, such sensors can be energy-demanding and feature latency in signal outputs for matching human motion resulting in compromised autonomous adaptation [114]. On the other hand, sEMG can be used in assistive robotic system controllers [70,115–122] gait classification [113,123–126] and predicting lower limb joint kinetics and kinematics [31,48,49,51,57], which serve well the purpose of the autonomous adaptation. Asif et al., [127] and Fleming et al., [128] reported that

biomimetic models, artificial neural networks, and support vector machines are widely used for such applications. However, there are several issues to take into account in using sEMG for such purpose one related to preprocessing or avoiding that, and two related to the number of sensors to be utilized.

First, sEMG signals have complicated and random patterns, making real-time analysis difficult [25, 129]. Halaki and Ginn [35] reported that amplitude normalization can make the interpretation of raw sEMG more accurate for detecting muscle activation. However, the implementation of a real-time normalization imposes additional difficulties in determining the reference value and leads to an elevated computational cost as the necessary periodic calibration of such reference can take several minutes [38] and disrupt real-time use. Fluctuations across sEMG channels caused by muscle fatigue and variability in skin impedance can also obscure the reference value over longer periods of time [39–42] and make sEMG normalization unsuitable for real-time processing [38]. One possibility could be finding static reference values for each targeted muscle through some pre-testing such as a few minutes of stable walking at a certain condition and normalizing the sEMG signals to those references in the real-time implementation. In the amputee prosthesis users, this could be utilized before adding any control to the device provided that it can work passively. This can serve to limit the computation cost of normalization, which needs to be tested in new studies. However, prolonged walking has been shown to cause muscle fatigue [130] and consequently decreased sEMG amplitudes [131]. More importantly, studies have shown variations in sEMG amplitudes with changes in walking speed [132], which may compromise the accuracy of static reference values. Currently, the use of non-normalized sEMG supported by feature extraction implementation is the plausible method to be utilized [128]. With the aim of achieving autonomous adaptation to improve the human-machine coordination performance in exoskeletons, Ma et al., [133] used time-domain features of sEMG of eight leg muscles collected from healthy subjects in order to estimate the knee joint angle by using a long short-term memory structure (LSTM). A similar approach was used by Foroutannia et al., [134] to develop an LSTM architecture that utilizes time-domain features of leg muscles in the prediction of hip joint kinematics.

Second, sEMG signals can be contaminated by noise caused by cross talk and skin conductivity change, or artifacts originating at the skin-electrode interface, signal amplifiers, and external sources [77]. Therefore, using a large number of sEMG sensors may cause processing complexity [135], complications in sensor setup design, and impose difficulty in daily use [128]. In different studies, the number of sEMG amplitudes utilized for predicting joint kinematics and kinetics varies from eleven (e.g., [90, 124, 136–139]) to four (e.g., [70, 140]). Zaffir et al., [141] developed and compared different types of neural network models for estimating dorsiflexion for robotic ankle-foot orthoses with similar concerns of minimizing the number of muscle inputs and eliminating mechanical sensors. They utilized sEMG data of four leg muscles of healthy participants. Extracted time-domain features were used as inputs, and the best performance was shown by the LSTM neural network.

Third, the original cause of the amputation, the choice of surgical technique, and factors such as residual limb length, shape, and subsequent muscle atrophy can affect muscle activity and, consequently, sEMG signals [142–144]. In transtibial amputation, the residual limb muscle availability gets compromised if the amputation is performed closer to the knee [3], whereas most muscle mass remains intact in ankle disarticulation [4].

Therefore, minimizing the number of sEMG muscle sources utilized in a joint kinematics and kinetics prediction algorithm will make the controller of a powered ankle prosthesis economic, and limiting the use of lower leg muscles will make it practical for both ankle disarticulation and transtibial amputation. Recently, we developed neural network-based algorithms to predict ankle position and moment using all combinations of sEMG amplitudes of several lower leg muscles [145]. This approach methodologically paved the way for achieving a user-specific algorithm development procedure as the most suitable sEMG variations that either minimizes the total number of sensors or those of lover leg muscles could be identified. However, the use of normalized sEMG exclusively impedes real-time applicability. In addition, the number of available muscles limited to five restricts versatile applicability, given the inter-individual differences of potential users. In the present study, the methodology is extended for competency

by (i) utilizing non-normalized sEMG signals coupled with feature extraction and (ii) making muscle input selection comprehensive via the usage of eight lower leg muscles.

The aims were to (1) implement our extended methodology for developing algorithms that predict sagittal ankle kinematics and kinetics during level walking using non-normalized lower limb sEMG signals, and (2) rank the extensive range of muscle combination variations according to their success to facilitate a user-specific selection of sensor inputs for economic and practical control algorithms that can be used in powered ankle prostheses.

3.2 Materials and Methods

3.2.1 Data Utilized and Summary of Data Collection Procedures

Gait data are required for developing, training, and testing neural networks. For that purpose, sEMG amplitudes, sagittal ankle angle, and moment of level walking trials were acquired from the open access data by Lencioni et al. [81]. The data includes (I) trials of level walking at different speeds (0.3 - 2.3 m/s) collected from fifty able-bodied subjects (25 males, 25 females, age range: 6 - 72 years, body mass: 18.2 - 110 kg, body height: 116.6 - 187.5 cm) and (II) in addition to joint kinematics and kinetics data also non-normalized sEMG data of tibialis anterior (TA), soleus (SO), medial gastrocnemius (MG), peroneus longus (PL), rectus femoris (RF), vastus medialis (VM), biceps femoris (BF) and gluteus maximus (GMax), which were recorded simultaneously with motion capturing during the level walking trials. Ankle joint kinematics and kinetics data were recorded using a 9-camera motion capture system (SMART system, BTS, Garbagnate Milanese, Italy), total-body LAMB marker set, and two force plates (Kistler, Winterthur, Switzerland). The sEMG amplitudes were recorded using an 8-channel wireless EMG recording system (ZeroWirePlus, Cometa, Bareggio, Italy) unilaterally on the dominant side with electrode locations in agreement with SENIAM [80], using pre-amplified self-adhesive Ag-AgCl electrodes (Medtronic Kendall, USA, 24 mm electrode diameter, 10 mm active part diameter, bipolar configuration, 20 mm

inter-electrode distance). sEMG amplitudes were band-pass filtered (10 Hz - 400 Hz) before sampling to reduce the aliasing effect, but not normalized. Synchronous data acquisition was managed by the proprietary software of the motion capture system.

In each experiment, the subjects were equipped with the LAMB total-body marker set, which includes retro-reflective markers (12 mm diameter) on lower limbs. As required by the LAMB protocol, additional markers were placed on the medial part of the lower limbs for the preliminary static calibration trial and were removed during the dynamic trials. Subjects were required to wear tight clothes or swimsuits and markers were attached to the skin above bony landmarks with double-sided adhesive tape.

For the level-ground walking task, subjects were initially asked to walk five trials at their natural speed. Then, they were asked to perform the following ten trials while progressively increasing (first 5 trials) or decreasing (latter 5 trials) their speed. No precise indications about gait speed or cadence in order not to induce gait alterations were given.

3.2.2 Neural Network Development

All neural networks to be developed feature the following: (1) The LSTM neural network architecture was used. LSTM is a deep learning method that is a form of the recurrent neural network model that can make predictions for time series in real-time [146, 147]. This architecture has been shown to be highly efficient in sEMG-based human motion pattern recognition for identifying the user's movement [148]. (2) sEMG features, calculated over sEMG amplitudes of leg muscles, were used as LSTM inputs to predict ankle position and moment (see Figure 3.1 for a block diagram). A similar input integration into LSTM has been shown to be highly efficient in estimating joint angles [133, 134, 141]. Presently, two separate LSTMs were developed and trained for predicting ankle joint position and moment. The reason for not using a single LSTM with multiple outputs was (i) to reduce complexity so that LSTMs can be

trained and tuned efficiently [149], (ii) to avoid possible over-fitting, which can cause inaccurate predictions for new data [150, 151] and (iii) to achieve better computational performance [150].

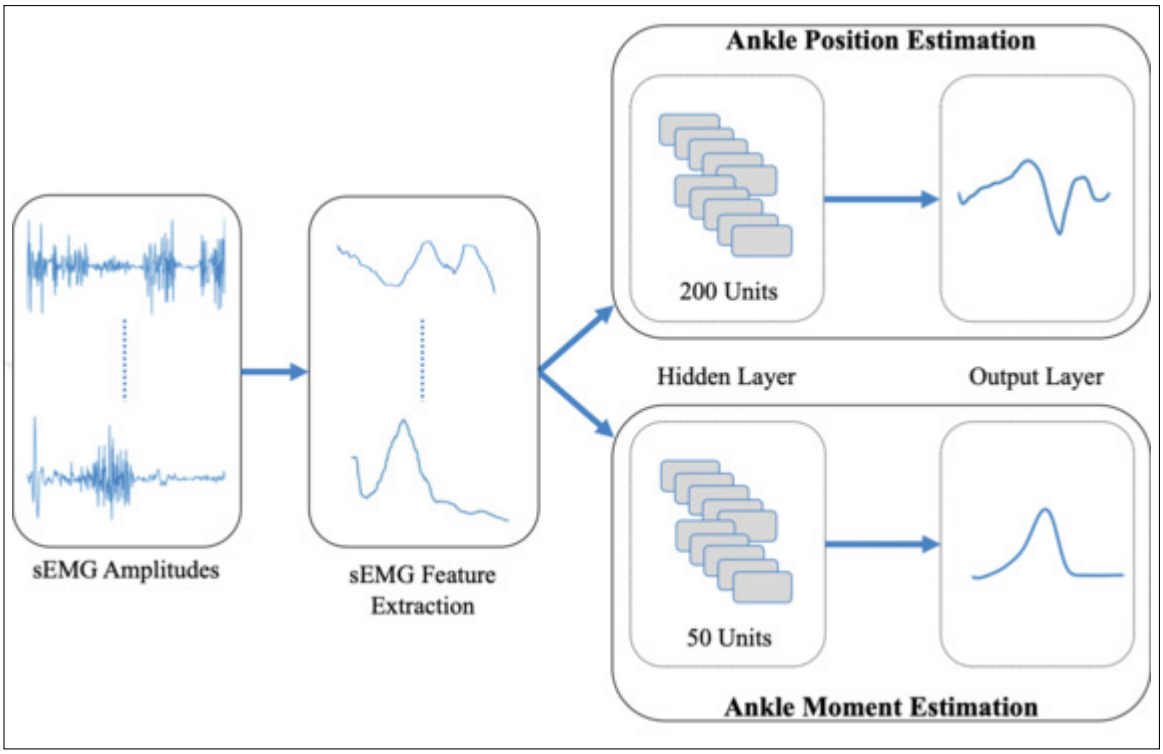


Figure 3.1 Block diagram of the LSTM structures for ankle position and moment prediction.

sEMG Feature Selection: sEMG features have been used widely as inputs for sEMG-based robotic controllers [103, 152]. Presently, five time-domain sEMG features that can be used efficiently in real-time applications [153] were tested and evaluated, which are: *integrated EMG (IEMG), mean absolute value (MAV), Willison amplitude (WAMP), root mean square (RMS)* and *waveform length (WL)*. Their mathematical definitions are presented in Table 3.1. Since the window size to calculate sEMG features should be less than 300 ms for real-time implementation [153], the window size was selected as 150 ms [90]. To test the success of sEMG features, all possible combinations (in total 31) were studied: 5 single features (e.g., IEMG), 10 two feature combinations (e.g., IEMG+MAV), 10 three feature combinations (e.g., IEMG+MAV+WAMP), 5 four feature combinations (e.g., IEMG+MAV+WAMP+RMS) and 1 five feature combination (i.e., IEMG+MAV+WAMP+RMS+WL). In order to determine the best-performing

sEMG feature variation, sEMG amplitudes of the muscle combination MG+BF+GMax were used based on the success of this muscle combination in ankle position and moment predictions [145].

Table 3.1
Mathematical definition of the sEMG feature extraction methods.x_n represents the sEMG signal in a segment n. N denotes the length of the sEMG signal. IEMG; the sum of the absolute values of the signal in a sliding window. MAV; mean of the absolute values of the signal in a sliding window. RMS; the square root of the average power of the sEMG amplitude in a sliding window. WL; the cumulative length of the sEMG amplitude within a sliding window. WAMP; the total number of stages resulting from amplitude change between two adjacent points that exceed a defined threshold in a sliding window. The threshold value for WAMP is chosen as 50 mV [153].

Integrated EMG	$\text{IEMG} = \sum_{n=1}^{N} \lvert x_n \rvert$
Mean Absolute Value	$\text{MAV} = \frac{1}{N} \sum_{n=1}^{N} \lvert x_n \rvert$
Root Mean Square	$\text{RMS} = \sqrt{\frac{1}{N} \sum_{n=1}^{N} x_n^2}$
Waveform Length	$\text{WL} = \sum_{n=1}^{N-1} \lvert x_{n+1} - x_n \rvert$
Willison Amplitude	$\text{WAMP} = \sum_{n=1}^{N-1} f(\lvert x_n - x_{n+1} \rvert)$ $f(x) = \begin{Bmatrix} 1, if x \geq threshold \\ 0, otherwise \end{Bmatrix}$

Muscle Selection: sEMG amplitudes of the eight lower extremity muscles included in the dataset were used: the TA, SO, MG, and PL in the lower leg and the RF, BF, VM, and GMax in the upper leg. To test the success of the use of sEMG amplitudes in neural networks inputs for the prediction of ankle position and moment, all possible combinations (in total 255) were studied: 8 single muscles (e.g., TA), 28 two muscle combinations (e.g., TA+SO), 56 three muscle combinations (e.g., TA+SO+MG), 70 four muscle combinations (e.g., TA+SO+MG+PL), 56 five muscle combinations (e.g., TA+SO+MG+PL+RF), 28 six muscle combinations (e.g., TA+SO+MG+PL+RF+BF), 8 seven muscle combinations (e.g., TA+SO+MG+PL+RF+BF+VM), and 1 eight muscle combination (i.e., TA+SO+MG+PL+RF+BF+VM+GMax).

The best-performing variation including the minimum total number of muscle

inputs is referred to as the *economic variation*. The variation performing better than the economic variation and including the minimum number of lower leg muscle inputs is referred to as the *flexible variation*. The best-performing variation including the minimum total number of only upper leg muscles is classified as *practical variation*.

3.2.3 Neural Network Training

The open access data [81] contains 844 level walking trials at various walking speeds. Randomly selected 675 datasets (80% of the total) were classified and used as training datasets and the rest were classified and used as validation datasets. Both training and validation datasets contain the same range of walking speed data (0.3 - 2.3 m/s) which enabled the LSTMs to be trained and tested for a wide range of walking speeds. The feature extraction function outputs for the TA muscle are exemplified in Figure 3.2 (see Appendix B for the remainder of the muscles). For each muscle within each dataset, the features were extracted and were used in the training and validation of LSTMs developed, which was done separately for ankle joint position and moment predictions. LSTMs were trained within MATLAB, using the Adam optimizer because of its computational efficiency and its success in non-stationary data [154]. The training was stopped after 200 epochs (e.g., [155]). The selection of the number of hidden units for joint position and moment predictor LSTMs was based on previous studies aiming at the utilization of sEMG in joint kinetics and kinematics predictions [156, 157], such that a range of 250 units was chosen for both. 200 hidden units for joint position and 50 hidden units for joint moment predictor LSTMs were determined (Figure 3.1) as the outcome of a systematical variation of the number of hidden units within this range to yield the highest correlations for ankle position and moment changes in the sagittal plane.

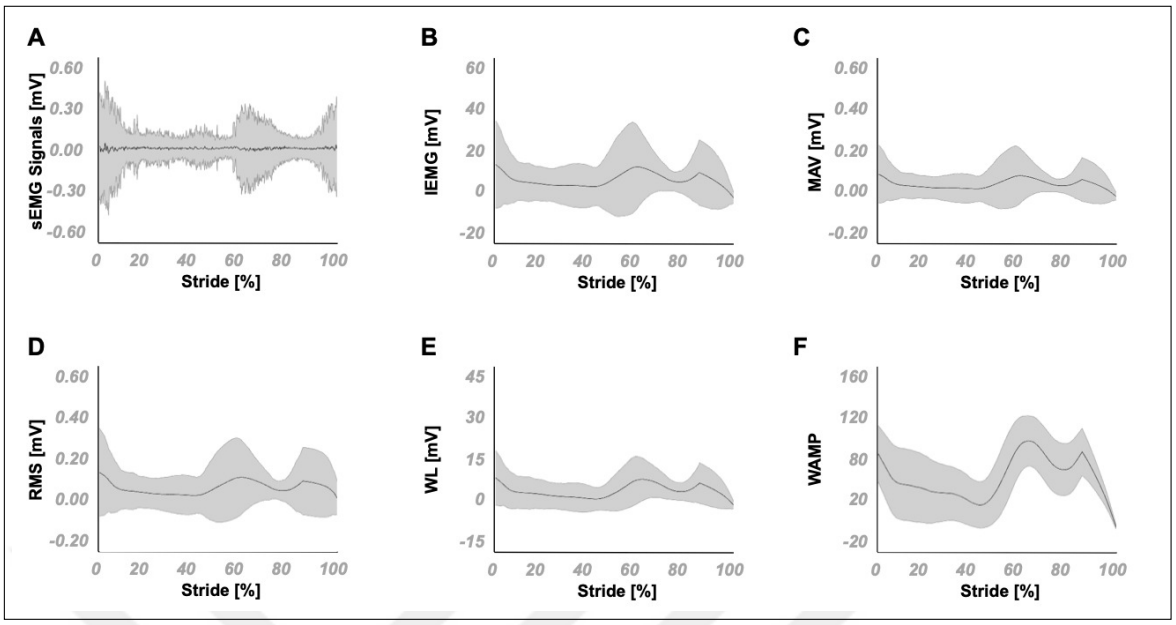


Figure 3.2 Mean and standard deviation of sEMG signals and its extracted features for the TA muscle. (A) the sEMG signals and the corresponding (B) IEMG, (C) MAV, (D) RMS, (E) WL, and (F) WAMP features.

3.2.4 Evaluation of the Developed Neural Networks

Normal Q-Q plots for the residuals between the original data and LSTM response were used to illustrate if the residuals follow a normal distribution. Two-way ANOVA for repeated measures (factors: %GC and muscle combination) was performed separately for joint position and moment predictions based on correlation coefficients. If significant main effects were found, Bonferroni post hoc tests were performed to further locate significant within-factor differences. One-way ANOVA was further used for temporal success assessment based on one-dimensional statistical parametric mapping (SPM) across the gait cycle (GC) using F-statistics [87]. Differences between the original data and estimated outputs were considered significant at $P < 0.05$.

To evaluate the outcome of the developed sEMG feature and muscle combinations (i.e., the best-performing one out of all possible 31 sEMG feature combinations x all 255 possible muscle combinations) for joint position and moment predictions, the following were used: (1) Pearson's correlation coefficient (r) between the original data

and LSTM response was calculated for the position (Pos Corr) and moment prediction (Mom Corr). r = 0.90 was selected as a strong correlation threshold. A *miscorrelation score* (Mis Corr) was defined as the sum of the deviation of correlation values from one. (2) Root-mean-square errors (RMSE) between the original data and LSTM response were calculated for the position (Pos RMSE) and moment prediction (Mom RMSE). An *RMSE score* was defined as the mean of position and moment RMSE values normalized to their respective peak value among all sEMG features or muscle combinations. (3) SPM analysis was conducted to localize significantly different %GC points between the original data and LSTM response, the total number of which are expressed as a percentage of the entire GC for the position (Pos SPM) and moment prediction (Mom SPM). An *SPM Score* was defined as the mean of those percentages for ankle position and moment predictions. (4) An *overall error score* was defined as the product of miscorrelation, RMSE, and SPM scores.

3.3 Results

3.3.1 sEMG Feature Selection

Table 3.2 shows the correlation coefficients, RMSE values, and SPM results of all sEMG feature combinations calculated over sEMG amplitudes of MG+BF+GMax and provides their ranking based on their overall error score.

The five feature combination (IEMG+MAV+RMS+WAMP+WL) shows a strong correlation ($r_{position}$ = 0.9006 and r_{moment} = 0.9663) and ranks 19^{th} amongst all.

Four feature combinations: Only IEMG+MAV+RMS+WL shows a strong correlation ($r_{position}$ = 0.9095 and r_{moment} = 0.9747) and ranks 6^{th} amongst all.

Three feature combinations: 2 of 10 variations show strong correlations ($r_{position}$ > 0.90 and r_{moment} > 0.97). IEMG+RMS+WL shows the strongest correlation ($r_{position}$ = 0.9031 and r_{moment} = 0.9710) and ranks 4^{th} amongst all variations.

Two feature combinations: 2 of 10 variations show strong correlations ($r_{position}$>0.90 and r_{moment}>0.97). IEMG+WL shows the strongest correlation ($r_{position}$ = 0.9006 and r_{moment} = 0.9742) and ranks 1^{st} amongst all variations.

Single features: Only WL shows a strong correlation ($r_{position}$ = 0.9006 and r_{moment} = 0 .9814) and ranks 11^{th} amongst all.

Results show that IEMG+WL yields the best position and moment prediction performance. SPM analysis of the IEMG+WL (Figure 3.3) showed that significant localized differences between the actual and estimated outputs are limited to 10 points (1-3%, 8-9%, 25-28%, and 54%GC) for ankle position, whereas no significantly different points were localized for ankle moment.

3.3.2 Muscle Selection

ANOVA (factors: %GC and muscle combination) showed significant main effects on joint position predictions, but no interaction. ANOVA (factors: %GC and muscle combination) showed significant main effects on joint moment predictions and significant interaction. *Post hoc* testing showed significant effects of muscle combination based on comparisons of correlation coefficients for (i) 239 out of 465 combinations for joint position predictions, and (ii) 227 out of 465 combinations for joint moment predictions.

Table 3.3 shows the correlation coefficients, RMSE values, and SPM results of best-performing 30 muscle combinations determined utilizing the sEMG feature IEMG+WL followed by selected exclusively upper leg muscle combinations, and provides their ranking based on their overall error score (see Appendix C for all variations).

Table 3.2

The comparison of the performance of sEMG feature variations utilizing the muscle combination MG+BF+GMax. Grey-shaded cells show feature variations that do not provide strongly correlated position and moment predictions (i.e., r <0.90). IEMG: integrated EMG, MAV: mean absolute value, WAMP: Willison amplitude, RMS: root mean square; WL: waveform length.

Rank	sEMG Feature Variations	Pos Corr [r]	Mom Corr [r]	Pos RMSE [deg]	Mom RMSE [Nm/kg]	Pos SPM [%GC]	Mom SPM [%GC]	Overall Error Score
1	IEMG+WL	0.9006	0.9742	4.6781	0.1094	0.1000	0.0000	0.0027
2	IEMG+MAV+RMS+WAMP	0.8948	0.9718	4.8151	0.1158	0.0600	0.1200	0.0054
3	MAV+RMS+WAMP	0.8933	0.9732	4.8809	0.1129	0.0600	0.2500	0.0093
4	IEMG+RMS+WL	0.9031	0.9710	4.6766	0.1154	0.0300	0.3300	0.0101
5	IEMG	0.8955	0.9780	4.9175	0.1090	0.1500	0.2200	0.0104
6	IEMG+MAV+RMS+WL	0.9095	0.9747	4.6147	0.1096	0.2000	0.2500	0.0112
7	IEMG+MAV+WL	0.8962	0.9758	4.7377	0.1083	0.2100	0.2000	0.0114
8	IEMG+RMS+WAMP	0.8940	0.9727	4.6181	0.1160	0.1400	0.2500	0.0115
9	WAMP	0.8884	0.9763	4.9206	0.1109	0.1800	0.2200	0.0121
10	RMS	0.8888	0.9757	5.0877	0.1142	0.1500	0.2700	0.0132
11	WL	0.9006	0.9814	4.8743	0.1020	0.2400	0.3200	0.0142
12	MAV+WAMP+WL	0.8860	0.9734	4.9387	0.1154	0.3200	0.1300	0.0145
13	RMS+WAMP+WL	0.8987	0.9706	4.7733	0.1145	0.1900	0.3100	0.0146
14	IEMG+MAV+RMS	0.9034	0.9800	4.7612	0.1076	0.0300	0.6100	0.0162
15	RMS+WL	0.9023	0.9782	4.8670	0.1062	0.2300	0.4000	0.0164
16	MAV+RMS+WL	0.8961	0.9671	4.8736	0.1122	0.3400	0.2000	0.0166

17	MAV	0.8824	0.9758	5.1429	0.1147	0.1900	0.3200	0.0168
18	IEMG+MAV	0.8885	0.9745	5.0225	0.1142	0.2000	0.3500	0.0173
19	IEMG+MAV+RMS+WAMP+WL	0.9006	0.9663	4.5362	0.1204	0.1100	0.4900	0.0179
20	WAMP+WL	0.8927	0.9665	4.7689	0.1196	0.0800	0.5600	0.0206
21	MAV+RMS+WAMP+WL	0.8965	0.9567	4.8439	0.1252	0.1000	0.5400	0.0222
22	RMS+WAMP	0.8776	0.9730	5.0264	0.1168	0.3900	0.2600	0.0225
23	MAV+RMS	0.8765	0.9766	5.2271	0.1132	0.3000	0.4000	0.0240
24	IEMG+MAV+WAMP+WL	0.8935	0.9605	4.6255	0.1275	0.1400	0.5700	0.0241
25	IEMG+RMS	0.8952	0.9744	4.9570	0.1120	0.1800	0.6800	0.0253
26	IEMG+RMS+WAMP+WL	0.8910	0.9709	4.8587	0.1202	0.6100	0.2100	0.0262
27	IEMG+WAMP	0.8751	0.9705	5.0310	0.1155	0.5500	0.2200	0.0275
28	MAV+WAMP	0.8827	0.9766	4.9713	0.1144	0.3600	0.5200	0.0283
29	IEMG+WAMP+WL	0.8906	0.9619	4.8330	0.1214	0.6200	0.2300	0.0291
30	MAV+WL	0.8924	0.9796	4.9329	0.1064	0.5900	0.5800	0.0329
31	IEMG+MAV+WAMP	0.8768	0.9611	4.9993	0.1304	0.4800	0.5900	0.0424

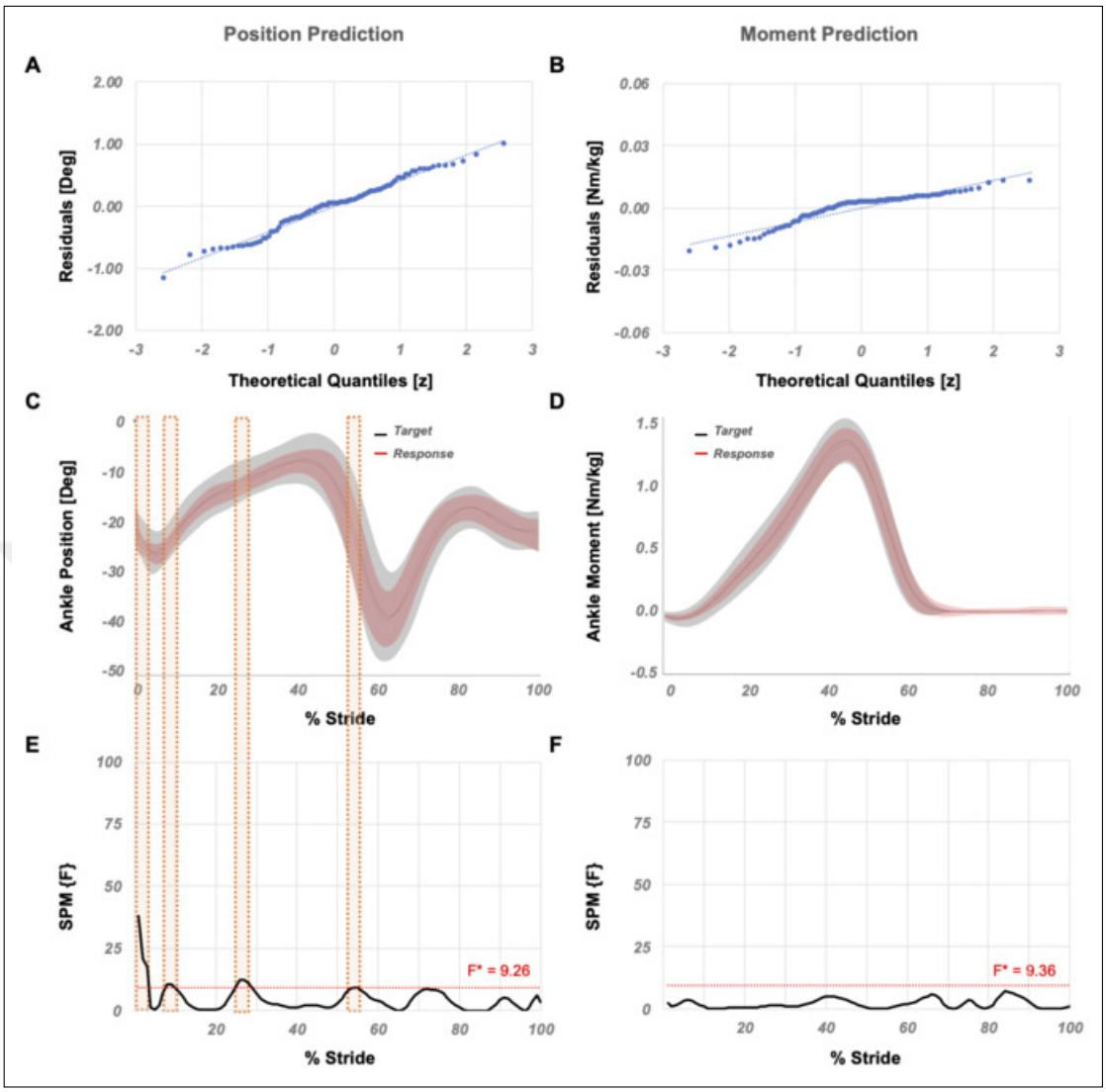


Figure 3.3 Temporal success assessment for IEMG+WL. The normal Q-Q plots for the residuals between original data and LSTM response for ankle (A) position and (B) moment. Mean and standard deviation of estimated NN response vs. original data for ankle (C) position and (D) moment, as a function of % stride. Statistical parametric mapping using F-statistics (SPMF) for the ankle (E) position and (F) moment as a function of % stride shows values below the threshold (i.e., for $P < 0.05$, F*position = 9.26, F*moment = 9.36). IEMG abbreviates integrated EMG and WL abbreviates waveform length.

Table 3.3

The best-performing 30 muscle combinations determined by utilizing the sEMG feature IEMG+WL. Darker Grey-shaded cells show muscle variations that do not provide strongly correlated position and moment predictions (i.e., r <0.90). Lighter gray hatched cells exemplify solely upper leg muscle variations that provide strongly correlated position and moment predictions (i.e., r >= 0.90). Based on significantly different correlation coefficients [r] (i.e., if any one of the position or moment correlations, or both are significantly different for a muscle variation), (*) and (^) indicate significantly different muscle variations from the flexible (MG+RF+VM) and practical (GMax+VM) muscle variations, respectively. TA: tibialis anterior, SO: soleus, MG: medial gastrocnemius, PL: peroneus longus, RF: rectus femoris, BF: biceps femoris, VM: vastus medialis, GMax: gluteus maximus.

Rank	Muscle Variations	Pos Corr [r]	Mom Corr [r]	Pos RMSE [deg]	Mom RMSE [Nm/kg]	Pos SPM [%GC]	Mom SPM [%GC]	Overall Error Score
1	MG+RF+VM^	0.9099	0.9707	4.5923	0.1072	0.0300	0.0400	0.0018
2	GMax+RF+SO	0.8978	0.9716	4.8759	0.1151	0.0500	0.0100	0.0018
3	BF+MG+GMax+PL+RF+SO^	0.9134	0.9714	4.3291	0.1067	0.0700	0.0200	0.0022
4	BF+MG+GMax+RF+SO+TA+VM^	0.9246	0.9803	4.1877	0.1012	0.1200	0.0000	0.0023
5	MG+GMax+PL+VM^	0.9101	0.9725	4.5901	0.1085	0.1000	0.0000	0.0026
6	BF+MG+GMax*^	0.9006	0.9742	4.6781	0.1094	0.1000	0.0000	0.0028
7	BF+MG+GMax+PL+RF+SO+TA+VM*^	0.9205	0.9695	4.2841	0.1060	0.0100	0.1200	0.0030
8	MG+GMax+RF+TA^	0.9123	0.9789	4.5078	0.1034	0.1100	0.0300	0.0033
9	MG+GMax+PL+RF+SO+TA^	0.9267	0.9733	4.1133	0.1079	0.0500	0.1100	0.0034
10	MG+GMax+TA*^	0.9164	0.9782	4.4843	0.1059	0.1200	0.0300	0.0034
11	RF+TA*^	0.9174	0.9776	4.6396	0.1081	0.0300	0.1200	0.0035
12	MG+SO+TA*^	0.9197	0.9769	4.4188	0.1072	0.1100	0.0500	0.0036
13	BF+MG+GMax+PL+SO+TA^	0.9166	0.9760	4.3324	0.1070	0.0200	0.1400	0.0037
14	BF+PL+RF+TA^	0.9161	0.9734	4.4649	0.1119	0.1000	0.0500	0.0037

15	PL+SO+TA+VM*^	0.9216	0.9768	4.4417	0.1104	0.1200	0.0600	0.0040
16	MG+PL+TA*^	0.9203	0.9757	4.3252	0.1083	0.1200	0.0700	0.0043
17	MG+GMax+PL+RF+TA^	0.9099	0.9779	4.3088	0.1068	0.1200	0.0600	0.0043
18	BF+MG+RF+SO+TA+VM^	0.9169	0.9754	4.2226	0.1048	0.1400	0.0600	0.0045
19	MG+GMax+PL+RF+SO+VM*	0.9136	0.9734	4.5057	0.1078	0.0900	0.1000	0.0047
20	MG+GMax+RF+SO+TA^	0.9196	0.9725	4.3227	0.1090	0.0600	0.1500	0.0049
21	BF+GMax+VM^	0.8904	0.9668	5.0332	0.1212	0.1300	0.0100	0.0049
22	GMax+PL+RF*^	0.9068	0.9689	4.7873	0.1143	0.1700	0.0000	0.0049
23	BF+MG+PL+RF*^	0.9102	0.9692	4.5424	0.1074	0.0800	0.1100	0.0050
24	BF+MG+GMax+PL+VM*^	0.9097	0.9788	4.4883	0.1065	0.1000	0.1100	0.0051
25	MG+GMax+RF+SO+VM	0.9119	0.9765	4.5431	0.1079	0.1000	0.1100	0.0052
26	BF+RF+TA*^	0.9164	0.9744	4.5841	0.1124	0.0600	0.1500	0.0052
27	BF+PL+SO+VM*^	0.9156	0.9649	4.5507	0.1183	0.0400	0.1600	0.0055
28	MG+PL+RF+SO+TA*^	0.9212	0.9589	4.3659	0.1113	0.1600	0.0500	0.0055
29	BF+MG+GMax+PL+SO+VM*^	0.9213	0.9748	4.2727	0.1077	0.0100	0.2400	0.0055
30	BF+MG+VM*^	0.9201	0.9769	4.4867	0.1083	0.0300	0.2300	0.0059
106	GMax+VM*	0.9010	0.9718	4.8927	0.1193	0.0900	0.2600	0.0107
154	BF+GMax+RF+VM*^	0.9018	0.9659	4.8817	0.1186	0.3300	0.1100	0.0139
247	RF+VM*^	0.9009	0.9712	4.8933	0.1181	0.3900	0.5800	0.0296

The eight muscle combination (BF+MG+GMax+PL+RF+SO+TA+VM) shows strong correlation ($r_{position}$ = 0.9205 and r_{moment} = 0.9695) and ranks 7^{th} amongst all variations.

Seven muscle combinations: All variations show strong correlations ($r_{position}$ > 0.90 and r_{moment} > 0.97). BF+MG+GMax+RF+SO+TA+VM shows the strongest correlation and ranks 4^{th} amongst all variations ($r_{position}$ = 0.9246 and r_{moment} = 0.9803).

Six muscle combinations: 26 of 28 variations show strong correlations ($r_{position}$ > 0.90 and r_{moment} > 0.95). BF+MG+GMax+PL+RF+SO shows the strongest correlation and ranks 3^{rd} amongst all variations ($r_{position}$ = 0.9134 and r_{moment} = 0.9714).

Five muscle combinations: All variations show strong correlations ($r_{position}$ > 0.90 and r_{moment} > 0.95). MG+GMax+PL+RF+TA shows the strongest correlation and ranks 17^{th} amongst all variations ($r_{position}$ = 0.9099 and r_{moment} = 0.9779).

Four muscle combinations: 66 of 70 variations show strong correlations ($r_{position}$ > 0.90 and r_{moment} > 0.96). MG+GMax+PL+VM shows the strongest correlation and ranks 5^{th} amongst all variations ($r_{position}$ = 0.9101 and r_{moment} = 0.9725).

Three muscle combinations: 45 of 56 variations show strong correlations ($r_{position}$ > 0.90 and r_{moment} > 0.96). MG+RF+VM shows the strongest correlation and ranks 1^{st} amongst all variations ($r_{position}$ = 0.9099 and r_{moment} = 0.9707).

Two muscle combinations: 21 of 28 variations show strong correlations ($r_{position}$ > 0.90 and r_{moment} > 0.96). RF+TA shows the strongest correlation and ranks 11^{th} amongst all variations ($r_{position}$ = 0.9174 and r_{moment} = 0.9776).

Single muscles: 2 of 8 variations show strong correlations ($r_{position}$ > 0.90 and r_{moment} > 0.97). PL shows the strongest correlation and ranks 69^{th} amongst all variations ($r_{position}$=0.9001 and r_{moment} = 0.9703).

Economic variation is PL which ranks 69th amongst all variations. SPM analysis (Figure 3.4) showed that significant localized differences between the actual and estimated outputs are limited to 1-3%, 12-13%, 30-31%, and 97-100% GC for the position and, 45-53% and 91-98% GC for the moment prediction.

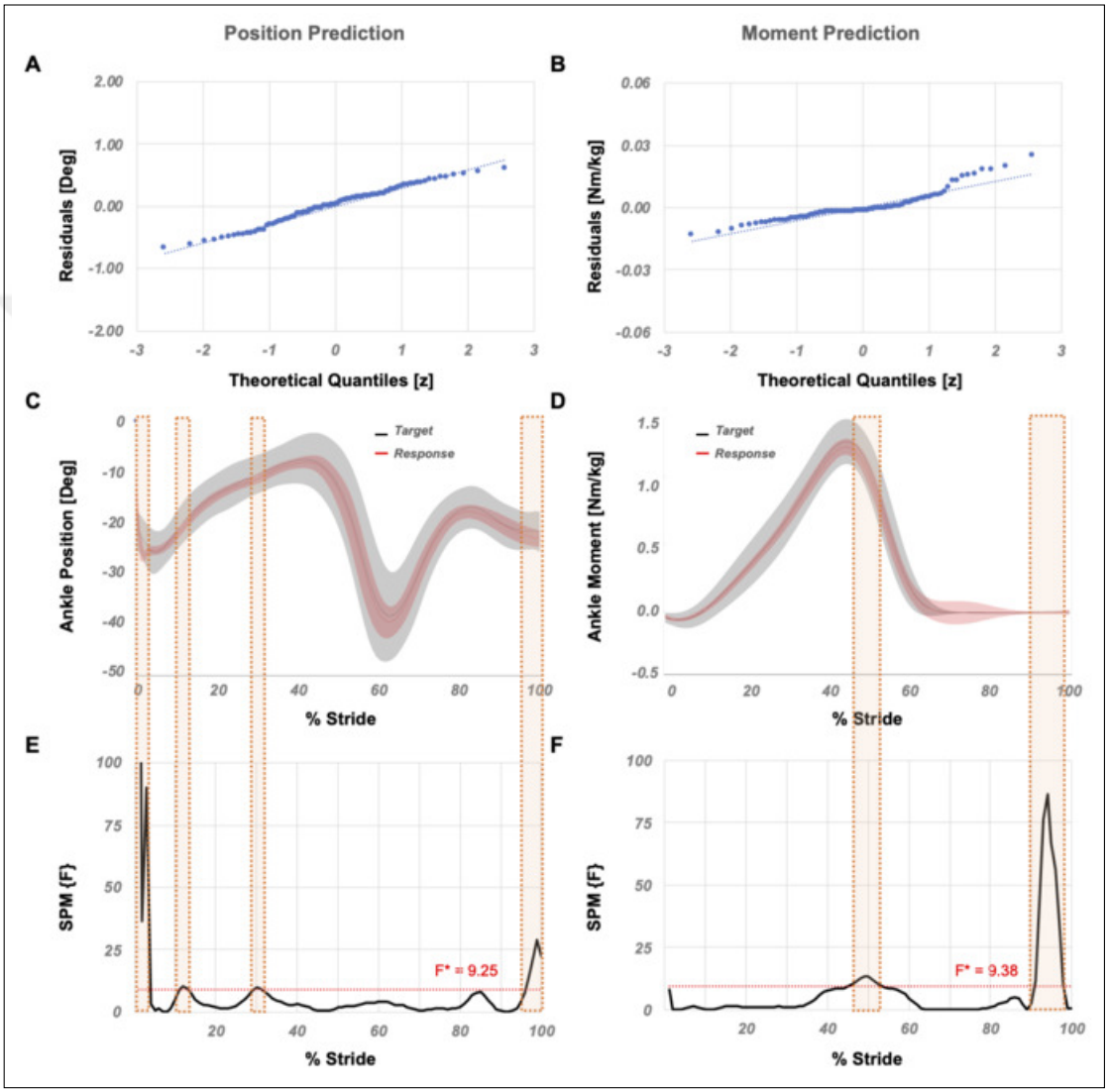


Figure 3.4 Temporal success assessment for PL. The normal Q-Q plots for the residuals between original data and LSTM response for ankle (A) position and (B) moment. Mean and standard deviation of estimated NN response vs. original data for ankle (C) position and (D) moment, as a function of % stride. Statistical parametric mapping using F-statistics (SPMF) for the ankle (E) position and (F) moment as a function of % stride shows values below the threshold (i.e., for $P < 0.05$, F*position = 9.25, F*moment = 9.38). PL abbreviates peroneus longus.

Flexible variation is MG+RF+VM, which ranks the 1st amongst all variations. Table 3.3 further shows muscle variations with significantly different correlation coefficients compared to MG+RF+VM. SPM analysis (Figure 3.5) showed that significant

localized differences between the actual and estimated outputs occur between 1-3% GC for the position and, 83-86% GC for the moment prediction.

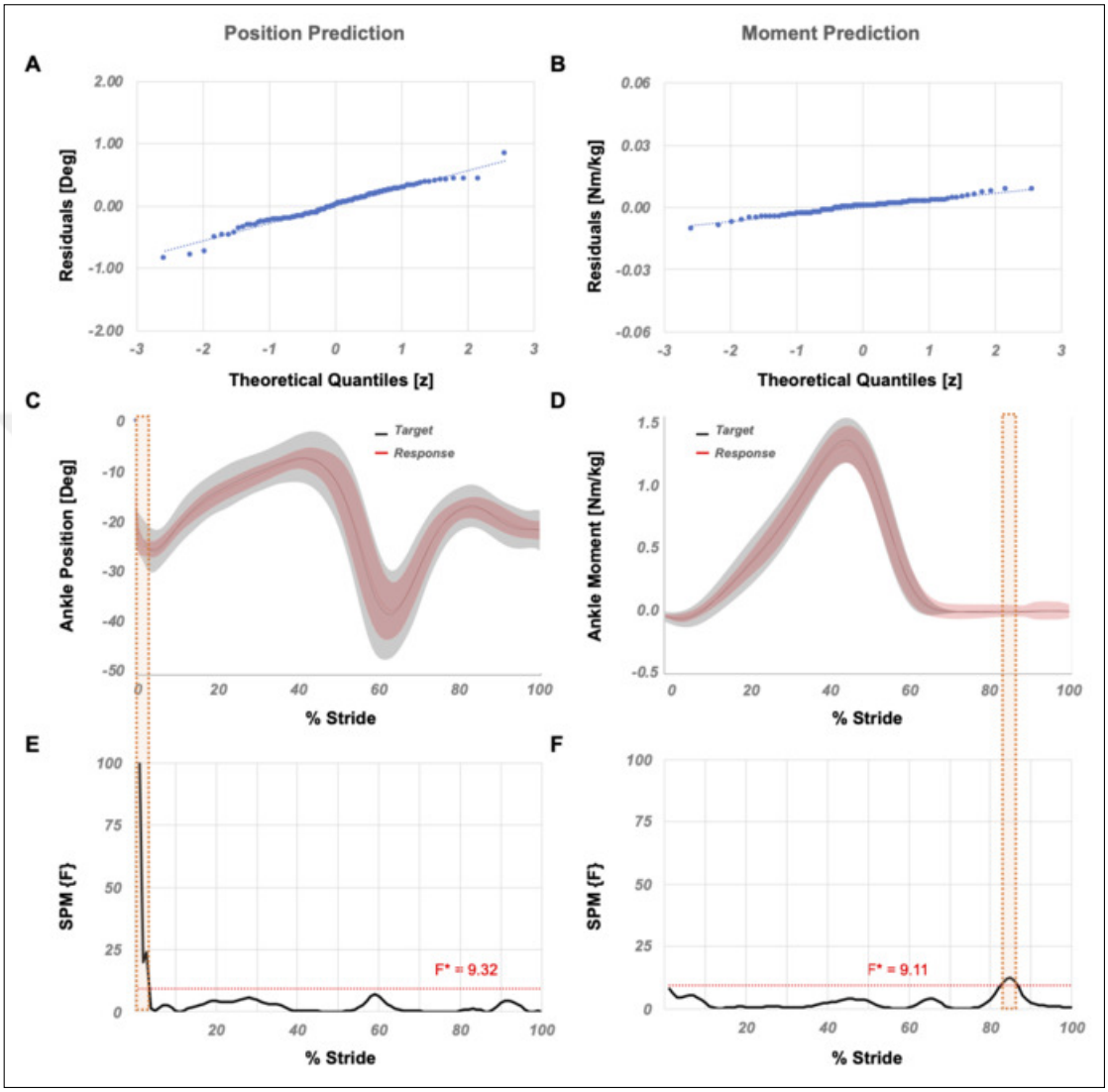


Figure 3.5 Temporal success assessment for MG+RF+VM. The normal Q-Q plots for the residuals between original data and LSTM response for ankle (A) position and (B) moment. Mean and standard deviation of estimated NN response vs. original data for ankle (C) position and (D) moment, as a function of % stride. Statistical parametric mapping using F-statistics (SPMF) for the ankle (E) position and (F) moment as a function of % stride shows values below the threshold (i.e., for $P < 0.05$, F*position = 9.32, F*moment = 9.11). MG abbreviates medial gastrocnemius, RF abbreviates rectus femoris, and VM abbreviates vastus medialis.

Practical variation is GMax+VM, which ranks the 106th amongst all variations. Table 3.3 further shows muscle variations with significantly different correlation coefficients compared to GMax+VM. SPM analysis (Figure 3.6) showed that significant localized differences between the actual and estimated outputs occur between 1-2%, and 89-95% GC for the position and 63-68% 74-91%, and 99-100% GC for the moment

prediction.

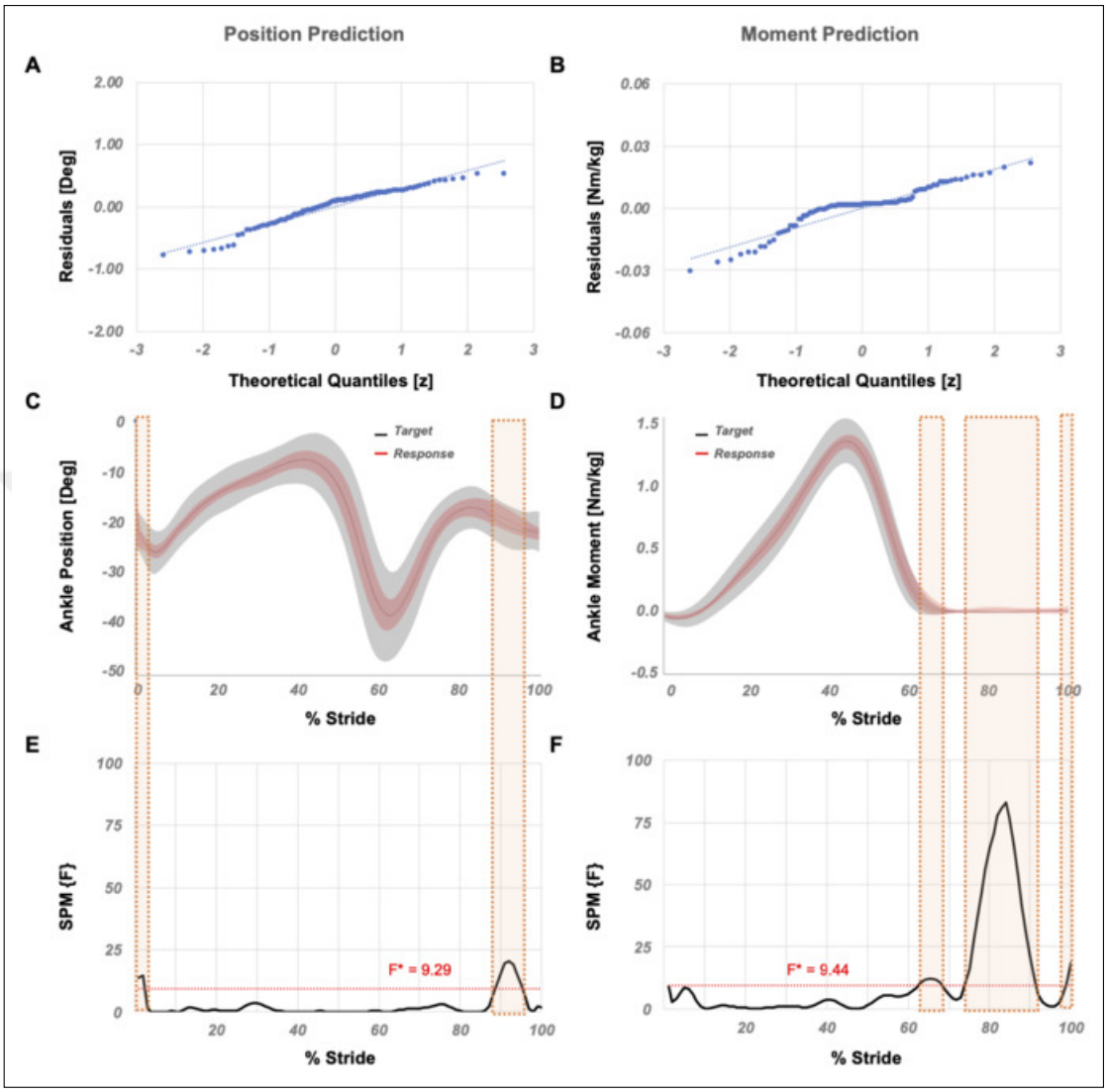


Figure 3.6 Temporal success assessment for GMax+VM. The normal Q-Q plots for the residuals between original data and LSTM response for ankle (A) position and (B) moment. Mean and standard deviation of estimated NN response vs. original data for ankle (C) position and (D) moment, as a function of % stride. Statistical parametric mapping using F-statistics (SPMF) for the ankle (E) position and (F) moment as a function of % stride shows values below the threshold (i.e., for $P < 0.05$, F*position = 9.29, F*moment = 9.44). GMax abbreviates gluteus maximus and VM abbreviates vastus medialis.

3.4 Discussion

Recent technological improvements in hardware development have advanced the field of lower limb prostheses [158–160]. However, an advanced autonomous adaptation is still required to achieve seamless and natural ambulation [128]. Therefore, studies

focused on sEMG-based algorithms for prosthesis controllers have started to accumulate [70, 117, 161, 162]. Recently, we developed neural networks showing that ankle position and moment changes during level walking can be predicted by using normalized sEMG amplitudes of leg muscles [145]. However, the use of normalized sEMG amplitudes was a limitation that is addressed in the present study.

Souza et al., [60] indicated that neuromuscular control schemes merging timing-based approaches could advance prosthesis control. Since the action patterns of walking occur in a time series [148] and sEMG amplitudes show variability in time and are cyclic [60], in order to make accurate predictions of joint movement using data from the past is essential. LSTM architecture contains a set of memory blocks [133] that can maintain its state over time [163], enabling the structure to remember the previous inputs [148]. Consequently, LSTM is widely used owing to its capability of generating accurate outputs for time series: the action patterns of walking occur in a time series [148], and LSTM generates outputs based on the inputs from the past [163], making it suitable for predicting joint kinematics and kinetics [133]. Also, the sEMG feature extraction is used widely, where features are extracted within a sliding window and used as inputs to predict joint kinetics or kinematics [52, 164–168]. Previous studies have shown that using sEMG features as input (e.g., [70, 75]), the LSTM structure (e.g., [169]), and their combined implementations (e.g., [148]) provide a successful prediction of intended motion. Although the prediction of ankle position and moment was not sought after, these studies demonstrated that accurate predictions using time-domain sEMG features and LSTM is plausible. Therefore, an LSTM structure that predicts ankle position and moment during level walking using features extracted from non-normalized sEMG amplitudes was implemented in the present study. Results showed that the developed LSTMs can predict ankle position and moment during level walking with up to 0.9292 and 0.9813 correlations, respectively. Note that, Huihui et al., [170] reported an RMSE of 4.80° in ankle position prediction, whereas Hahn and O'Keefe, [89] reported an RMSE of 0.10 Nm/kg in ankle moment prediction. However, those authors utilized 5 and 7 muscles, respectively. Ma et al., [133] estimated the knee joint angle using 8 muscles with an RMSE of 4.60°, whereas Farmer et al., [30] estimated the ankle joint angle using 3 lower leg muscles and reported an RMSE of 5.40°. By utilizing only three

muscles, the present LSTM structure yielded a compatible success with 4.5923° and 0.1072 Nm/kg RMSE.

Although studies aiming to develop sEMG-based lower limb prosthesis controllers have increased in the last decade, there is still no commercialized product that relies on neuromuscular input [128]. Song et al., [148] predicted the movement patterns using normalized sEMG amplitudes of RF, VM, vastus lateralis, and semitendinosus muscles to extract features within a sliding window size of 1024 ms. However, a window size of less than 300 ms was suggested to support the implementation of feature extraction in real-time prosthetic control [153]. Also, sEMG normalization is a non-specific method in terms of the required data to determine the reference value [35], e.g., the large window size can be a major limitation for the required computation and real-time applicability. Spanias et al., [75] and Spanias et al., [70] utilized the same number of neuromuscular inputs and achieved the use of non-normalized sEMG amplitudes collected from RF, tensor fasciae latae, semitendinosus, and adductor magnus to extract features within a window size lower than 300 ms. Nonetheless, they have implemented the additional mechanical sensor, which can be energy-consuming and could be a trade-off in autonomous adaptation due to its latency in generating the output for human locomotion [114] (Zhang et al., 2019). Utilizing solely non-normalized sEMG amplitude was achieved but the number of neuromuscular inputs was increased. In order to recognize the locomotion modes, Huang et al., [90] utilized sEMG amplitudes of RF, VM, sartorius, vastus lateralis, gracilis, biceps femoris long head, semitendinosus, biceps femoris short head, and adductor magnus muscles. Hargrove et al., [137] developed a pattern recognition algorithm using sEMG amplitudes of BF, RF, VM, vastus lateralis, sartorius, gracilis, adductor magnus, and tensor fasciae latae. Chen et al., [49] developed a deep belief network-based algorithm to estimate lower limb joint angles including the ankle, and utilized sEMG amplitudes collected from BF, VM, RF, MG, TA, SO, MG, semitendinosus, vastus lateralis, and sartorius. Huihui et al., [170] implemented the use of feature extraction and non-normalized sEMG amplitudes collected from the external gastrocnemius, gastrocnemius, SO, TA, and tibialis longus in order to estimate ankle joint angle. Wang et al., [171] used sEMG amplitudes of RF, VM, BF, semitendinosus, and gastrocnemius to estimate knee joint angles. These studies show

that the prosthesis controller can be advanced with several sEMG inputs. However, such implementation may bear difficulties regarding processing complexity [135]. Au et al., [10] limited the use of neuromuscular input size and utilized TA and gastrocnemius muscles in order to develop a powered ankle prosthesis controller, whereas Au et al., [9] and Farmer et al., [30] used the same muscles and included the SO to predict the ankle position. Similarly, Zabre-Gonzalez et al., [31] developed a neural network-based algorithm to predict ankle position and moment using TA and MG muscles. Jephil et al., [51] utilized the same muscles with the addition of the lateral gastrocnemius to estimate the ankle joint torque and angle. These studies show that the neuromuscular input size can be reduced by using the lower leg muscles. However, Huang and Ferris, [3] showed that sEMG amplitudes patterns of the TA, gastrocnemius medial head, and gastrocnemius lateral head in transtibial amputees, recorded within the prosthetic socket during walking, have high inter-subject variability. Therefore, limiting lower leg muscle inputs or using solely upper leg muscles can increase the compatibility of the prediction algorithms for different levels of amputations. In the present study, with the goal of real-time applicability, we developed LSTMs to predict ankle position and ankle moment using time-domain features extracted within 150 ms from non-normalized sEMG amplitudes. The proposed LSTM structure eliminates the need for external mechanical sensor inputs which cause high processing complexity. Also, the presented structure is capable of generating strongly correlated predictions by using sEMG amplitudes of GMax and VM muscles, addressing the compatibility issue. Furthermore, none of the previous studies provided a systematic analysis for the selection of muscles to be used as input. We recently developed a methodology to systematically study all possible variations of sEMG inputs from lower leg muscles [145]. Yet, the implementation of this methodology to level walking was limited to the usage of five muscle inputs (TA, MG, RF, BF, and GMax) and more importantly to normalized sEMG data exclusively. Presently, we extended the systematic analysis by including also SO, PL, and VM muscles. Note that, indeed the PL muscle was shown to be relevant as even a single input, whereas the analyses indicated that VM is important in limiting the usage of lower leg muscles. However, the bigger contribution of the present study was the extension of the methodology to make it suitable for real-time implementation, which now involves the utilization of features extracted from non-normalized sEMG signals

as inputs to the LSTM architecture. Integration of the SPM analysis outcome into the performance metric is also a new approach allowing for better tracking of specific %GC's showing significant differences between the original data and LSTM response. These present achievements provide good versatility by increasing the choices of upper and lower leg muscles and improving the user-specific applicability of sEMG-based ankle position and moment prediction procedures in powered ankle prosthesis control algorithms.

The present study shows that the LSTM is suitable for ankle position and moment prediction by using the time-domain features extracted from the non-normalized sEMG amplitudes as input. Our comprehensive time-domain sEMG feature selection analysis showed that the best-performing variation is IEMG+WL, which is frequently implemented in sEMG-based prosthesis controller studies [128] and is feasible to be used in real-time applications [153]. Presently, we used the muscle combination MG+BF+GMax for sEMG feature selection. Previous studies with a similar aim of utilizing sEMG in predicting joint kinematics and kinetics conducted either a feature (e.g., [153]) or a muscle combination selection (e.g., [172]), or report only the utilized feature per muscle [153, 173]. Note that, taking into account the challenging nature of determining which specific parameter or combination of parameters is responsible for an improved neural network output [174], a separate evaluation of the effects of multiple parameters has been suggested [175]. The complexity of the neural networks can consequently be reduced for efficient training [149]. Our present approach, which involves already a large space of possible muscle combinations (255) is in concert with that. To the best of our knowledge studies combining the possible sets of both sEMG feature selection and muscle selection are very rare and one which did cover both involves only 11 muscle combinations [176]. In the present study, the muscle combination (i.e., MG+BF+GMax) used in the sEMG feature selection process was chosen based on our previous study [145], which was shown to provide successful predictions, while minimizing the use of lower leg muscles. The feature combination IEMG+WL selected as a result if put to the test with also other muscle combinations that stood out in Keles and Yucesoy [145] yields consistently the preferable results (see Appendix D for details): for BF+MG+TA (the three muscle combination providing improved predic-

tions without aiming at minimizing the use of lower leg muscles), for MG+TA (the successful combination with minimum muscle inputs) and for BF+MG+GMax+RF+TA (the best-performing muscle combination), IEMG+WL shows the best performance among other feature combinations yielding strongly correlated predictions (minimally, $r_{position} = 0.9161$ and $r_{moment} = 0.9739$). Our comprehensive muscle selection analysis showed that 225 of 255 variations provide strong correlations for ankle position and moment prediction, ascribed to the flexibility of using all combinations of a wide range of muscles. A specific assessment seeking the economic variation showed that PL alone provides the best performance in minimizing the number of muscle inputs. This is a lower leg muscle with limited accessibility but, strongly correlated predictions were shown to be achievable by utilizing solely upper leg muscles. The practical variation achieving the best performance by minimizing utilized upper leg muscles is comprised of GMax+VM which are highly relevant for sEMG-based prosthesis controller development [128]. On the other hand, the flexible variation, i.e., MG+RF+VM showed that the best performance can be achieved by using a combination of upper and lower leg muscles.

The limitations of the present study need to be addressed. The position and moment predicting LSTMs were developed, trained, and tested using data from healthy subjects only. Note that, the open database by Lencioni et al., [81] involving non-normalized sEMG amplitudes of various leg muscles is a rarity, but the lack of an open database that consists of amputee data limits further testing. However, Huang and Ferris, [3] reported that transtibial amputees are able to voluntarily activate their leg muscles with several of them producing activation profiles similar to healthy controls during voluntary dorsiflexion and plantar flexion. They also demonstrated that amputees are capable of generating consistent sEMG amplitude patterns from stride to stride, which supports the approach utilized in this study for developing position and moment predicting LSTMs. On the other hand, in case sEMG amplitude patterns show differences in amputees compared to those of healthy subjects, the proposed infrastructure can be adapted by re-training it with data collected from amputees. This will also facilitate patient-specific algorithm development. Also, the present study focuses on the prediction of ankle position and moment during level walking only, yet

the LSTMs can be advanced for different locomotion tasks such as stair ascending and descending. Training their LSTM and using time-domain features extracted from non-normalized sEMG amplitudes of eight muscles involving RF, BF, TA, and SO, Lu et al., [53] achieved lower limb joint angles prediction for additional locomotion tasks. Therefore, the developed methodology is suitable for such prediction algorithms. Overall, the accuracy of ankle movement predictions should be studied after re-training the developed LSTM structure with a large database including non-normalized sEMG amplitudes collected from lower extremity amputees and different locomotion tasks can be adapted. Note that, unlike surface electrodes, electrodes within the socket of the prosthetic device may compromise the user's comfort, and long-term use may negatively affect the sensor's lifetime. The use of e.g., sEMG knit band sensor [91] i.e., a silver-plated conductive yarn for electrodes knitted with a moisture-wicking technical yarn can make implementation much easier and improve comfort. Additionally, high-density sEMG can help avoid problems related to bipolar electrode placement [92] and improve data quality [93].

In bodily motion, humans have the sensation of position and moment changes in their limbs and such proprioception is essential to human motor control [95]. Consequently, to support natural ambulation, powered prostheses require advanced autonomous adaptation, which can be achieved with the real-time implementation of joint position and moment prediction [128]. The present study serves this purpose by utilizing non-normalized sEMG amplitudes and LSTM architecture for ankle joint position and moment predictions in level-ground walking. This structure can be implemented in real-time robotic control applications (e.g., [173]) and used to generate reference inputs for advanced powered prosthesis controllers such as impedance control [177, 178].

3.5 Conclusion

A novel LSTM approach utilizing exclusively lower limb non-normalized sEMG amplitudes was developed. Its feasibility for predicting ankle angle and moment during

level walking of a healthy population was evaluated by testing five time-domain features (IEMG, MAV, WAMP, RMS, and WL) and eight leg muscle combinations (TA, SO, MG, PL, RF, VM, BF, and GMax). PL and GMax+VM performed best in predicting ankle motion while minimizing the total number of sEMG inputs and minimizing the use of lower leg muscles, respectively. The best-performing variation MG+RF+VM combines upper and lower leg muscle inputs. The versatile LSTM architecture utilizing non-normalized sEMG inputs makes the algorithms get closer to being implemented in a real-time implementation. Moreover, the comprehensive testing protocol developed involving ranking of all muscle combinations according to their success will facilitate user-specific solutions. However, in order to translate an offline application into online applicable powered ankle prosthesis control algorithms, the present implementation needs to be extended with other movement types, followed by training and testing of the algorithms for data collected from amputee participants in future studies.

4. THE OPTIMIZATION OF THE LSTM-BASED ANKLE POSITION AND MOMENT PREDICTOR

4.1 Introduction

In recent years, there have been significant advancements in powered ankle prostheses, enhancing the quality of life for individuals suffering from lower limb amputations. However, in order to achieve seamless interaction between the prosthetic and the user, the implementation of autonomous adaption is still a requirement [179]. The main aim is to establish a direct connection between the amputee and the prosthesis controller, enabling a smooth transmission of user commands to the prosthetic [128]. In order to achieve this, surface electromyography (sEMG) has emerged as a promising method for analyzing muscle activity in the residual limb and translating them into inputs for the prosthesis controller [180]. Even though these signals have been utilized as controller inputs for powered upper limb prostheses for decades [181], the utilization of sEMG-based control for lower limb prostheses is still in its early stages. Therefore, various methods have been proposed, particularly to predict lower limb joint kinetics and kinematics. Two dominant approaches are the use of biomimetic models and deep learning infrastructures [54]. Biomimetic models have been proven to be efficient (e.g., [9, 46, 47]), however, their implementation is challenging due to their complexity, reliance on assumptions, and calibration requirements [55]. On the other hand, the use of deep learning infrastructures such as long short-term memory (LSTM) is promising since it has been reported as among the most effective and robust for predicting time-series data [182–184].

Recent studies on joint movement prediction using LSTM network focused on employing feature extraction, instead of directly utilizing sEMG signals. Feature extraction involves the sliding window technique that is used for dividing the sEMG signal into smaller time windows of equal size. The sliding windows enable capturing temporal information regarding the target muscle activity, and from each window, application-

specific information can be extracted and used as inputs to the LSTM for the sake of accurate prediction [185]. However, the size of the window is a decisive parameter for prediction accuracy. A small window size provides detailed information such as rapid changes in muscle activity but causes high computational complexity due to the need of processing a large number of windows. Conversely, a large window size provides a global perspective of the sEMG signal and reduces computational complexity, but it may miss specific muscle activations [186]. Siu et al., [50] developed an LSTM-based algorithm to predict ankle torque during locomotion by utilizing sEMG signals. A window of 500 ms was used in extracting two features from eight muscles. However, it is reported that the total response time for myoelectric control should not exceed 300 ms [187, 188]. Consequently, a window size of less than 300 ms was suggested for the implementation of feature extraction in real-time prosthetic control [153]. Therefore, Chen et al., [189] used a 50 ms window to extract one feature from each of the five leg muscles in the ankle movement prediction study. Truong et al. [52] increased the window size and used a 100 ms window to extract eight features. Features of seven muscles were then utilized as inputs to predict the kinetics and kinematics of the ankle and knee joints. Similarly, Liu et al. [190] used the same window size to extract four features from each of the six leg muscles in order to estimate the knee joint. Huang et al., [90] developed a prosthesis controller algorithm, in which eleven muscles' sEMG signals were used. From each muscle, four features were extracted within a window of 150 ms and used as inputs. Li et al., [191] increased the window size to 210 ms in order to extract seven features. Four muscles' sEMG signals were used to predict ankle movement. Hargrove et al., [192] used a window size of 250 ms in the development of a controller of a powered transfemoral prosthesis, in which five muscles' sEMG signals were utilized to extract five features.

Therefore, there is a variety of window sizes ranging from 50 to 250 ms for the feature extraction of sEMG signals [128]. Thus, the best-performing window size should be determined according to the application, the infrastructure, the input, and the desired output. Recently, we developed an LSTM-based algorithm to predict ankle position and moment [193]. Inputs were two features extracted from sEMG signals of eight leg muscles in different combinations. A window size of 150 ms was used for

feature extraction. In the present study, the effect of the use of different window sizes on prediction accuracy will be investigated. This approach will allow for a comprehensive evaluation of the LSTMs' performance across different window sizes, enabling the selection of the optimal window size for accurate position and moment prediction.

The aims were to (1) test the effect of different window sizes for extracting sEMG features that are used as input to predict sagittal ankle kinematics and kinetics during level walking, (2) rank the window sizes to their success, and (3) validate the overall LSTM structure.

4.2 Materials and Methods

4.2.1 Gait Data Utilized

The open-access data provided by Lencioni et al. [81] was utilized to develop, train, and test LSTMs. The purpose was to obtain sEMG amplitudes, sagittal ankle angle, and moment from level walking trials. The open-access data consists of 844 level walking trials at different speeds (0.3 - 2.3 m/s) collected from fifty able-bodied subjects (25 males, 25 females, age range: 6 - 72 years, body mass: 18.2 - 110 kg, body height: 116.6 - 187.5 cm). In each trial, ankle joint kinematics and kinetics were collected along with simultaneously recorded non-normalized sEMG signals of tibialis anterior (TA), soleus (SO), medial gastrocnemius (MG), peroneus longus (PL), rectus femoris (RF), vastus medialis (VM), biceps femoris (BF) and gluteus maximus (GMax). Joint kinematics and kinetics data were recorded using a 9-camera motion capture system (SMART system, BTS, Garbagnate Milanese, Italy), total-body LAMB marker set, and two force plates (Kistler, Winterthur, Switzerland). The sEMG amplitudes were recorded using an 8-channel wireless EMG recording system (ZeroWirePlus, Cometa, Bareggio, Italy) unilaterally on the dominant side with electrode locations in agreement with SENIAM [80], using pre-amplified self-adhesive Ag-AgCl electrodes (Medtronic Kendall, USA, 24 mm electrode diameter, 10 mm active part diameter, bipolar configuration, 20 mm inter-electrode distance). sEMG amplitudes were band-pass filtered

(10 Hz - 400 Hz) before sampling to reduce the aliasing effect, but not normalized.

4.2.2 Neural Network Development

The LSTM structure in the previous study was preserved [193]. Two separate LSTMs were developed, trained, and tested in order to predict sagittal ankle position and moment. sEMG features, calculated over sEMG amplitudes were used as inputs. The selection of muscles for sEMG signals and the features to be extracted was determined based on the ranking provided in our previous study [193]. The sEMG signals of MG, RF, and VM were utilized as inputs for the feature extraction. Integrated EMG (IEMG) i.e., the sum of the absolute values of the signal in a sliding window (Eq. 4.1), and waveform length (WL) i.e., the cumulative length of the sEMG amplitude within a sliding window (Eq. 4.2) were then calculated for each muscle to serve as input for the LSTMs. 200 and 50 hidden units for position and moment predictor LSTMs were used based on our previous study [193].

$$MAV = \frac{1}{N}\sum_{n=1}^{N}|x_n| \tag{4.1}$$

$$WL = \sum_{n=1}^{N-1}|x_{n+1} - x_n| \tag{4.2}$$

In order to determine the best-performing window size for the feature extraction that is employed in the LSTMs, a systematical analysis was conducted. The analysis involved the development of position and moment predictor LSTMs that utilize IEMG and WL feature inputs which are extracted within different window sizes. The window sizes varied from 25 to 250, with an increment of 25. Thus, ten position and moment predictor LSTMs were developed.

4.2.3 Neural Network Training

The open-access data [81] contains 844 level walking trials at various walking speeds. 80% of the trials were used as training datasets, whereas the rest were used as validation datasets. LSTMs were trained within MATLAB, using the Adam optimizer because of its computational efficiency and its success in non-stationary data [154]. The training was stopped after 200 epochs (e.g., [155]).

4.2.4 Evaluation of the Developed Neural Networks

Normal Q-Q plots for the residuals between the original data and LSTM response were used to illustrate if the residuals follow a normal distribution. Two-way ANOVA for repeated measures (factors: %GC and window size) was performed separately for joint position and moment predictions. If significant main effects were found, Bonferroni post hoc tests were performed to further locate significant within-factor differences. One-way ANOVA was further used for temporal success assessment based on one-dimensional statistical parametric mapping (SPM) across the gait cycle (GC) using F-statistics [87]. Differences between the original data and estimated outputs were considered significant at $P < 0.05$.

To evaluate the outcome of the developed LSTMs, the following were used: (1) Pearson's correlation coefficient (r) between the original data and LSTM response was calculated for the position (Pos Corr) and moment prediction (Mom Corr). $r = 0.90$ was selected as a strong correlation threshold. A *miscorrelation score* (Mis Corr) was defined as the sum of the deviation of correlation values from one. (2) Root-mean-square errors (RMSE) between the original data and LSTM response were calculated for the position (Pos RMSE) and moment prediction (Mom RMSE). An *RMSE score* was defined as the mean of position and moment RMSE values normalized to their respective peak value among all LSTMs. (3) SPM analysis was conducted to localize significantly different %GC points between the original data and LSTM response, the total number of which are expressed as a percentage of the entire GC for the position

(Pos SPM) and moment prediction (Mom SPM). An *SPM Score* was defined as the mean of those percentages for ankle position and moment predictions. (4) An *overall error score* was defined as the product of miscorrelation, RMSE, and SPM scores.

The overall error score was used to rank window sizes according to their success. The best-performing one was further evaluated with cross-validation, in which LSTMs were re-trained and tested with different datasets four more times.

4.3 Results

ANOVA (factors: %GC and window size) showed significant main effects of both factors on joint position and moment predictions, but significant interaction for only position prediction. *Post hoc* test showed significant differences of window sizes for (i) 44 out of 45 comparisons for joint position predictions, and (ii) 42 out of 45 comparisons for joint moment predictions (Figure 4.1).

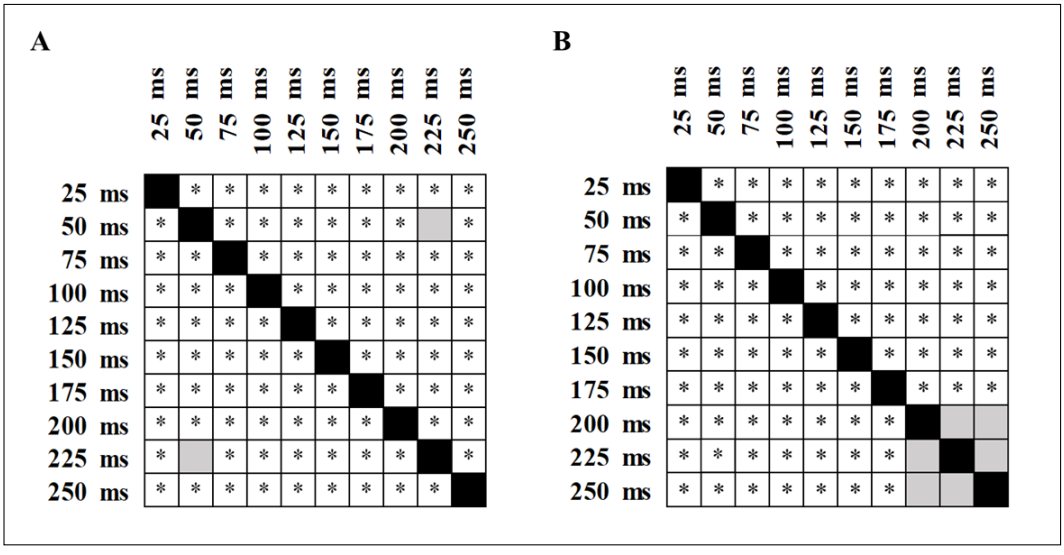


Figure 4.1 *Post hoc* test results for the effect of window sizes on joint position (A) and moment (B) prediction. (*) indicates a significantly different comparison of window sizes, whereas grey-shaded cells show otherwise.

Table 4.1 shows the correlation coefficients, RMSE values, and SPM results of all LSTMs with different window sizes and provides their ranking based on their overall

Table 4.1
The performance comparison of window sizes for the IEMG+WL feature combination utilizing the sEMG signals of MG+RF+VM muscle combination. Grey-shaded cells show window sizes that do not provide strongly correlated position or moment predictions (i.e., r <0.90).

Rank	Window Size	Pos Corr [r]	Mom Corr [r]	Pos RMSE [deg]	Mom RMSE [Nm/kg]	Pos SPM [%GC]	Mom SPM [%GC]	Overall Error Score
1	150ms	0.9099	0.9707	4.5923	0.1072	0.0300	0.0400	0.0019
2	175ms	0.9013	0.9691	4.7393	0.1215	0.0100	0.2700	0.0088
3	250ms	0.9039	0.9692	4.6702	0.1207	0.2800	0.0500	0.0100
4	225ms	0.9057	0.9707	4.6736	0.1215	0.0200	0.3600	0.0113
5	50ms	0.9032	0.9739	4.8765	0.1205	0.2200	0.2300	0.0135
6	100ms	0.9052	0.9692	4.8090	0.1219	0.0300	0.4200	0.0138
7	25ms	0.9027	0.9741	4.8837	0.1189	0.3100	0.2000	0.0153
8	75ms	0.8892	0.9701	4.9890	0.1207	0.4600	0.1200	0.0202
9	200ms	0.8998	0.9722	4.7141	0.1188	0.6700	0.1000	0.0235
10	125ms	0.9072	0.9665	4.7676	0.1230	0.3800	0.4600	0.0259

Table 4.2
Cross-validation results. Trial "0" refers to the main validation result from the performance comparison of window sizes, while the rest refers to the cross-validation results.

Trial	Pos Corr [r]	Mom Corr [r]	Pos RMSE [deg]	Mom RMSE [Nm/kg]	Pos SPM [%GC]	Mom SPM [%GC]
0	0.9099	0.9707	4.5923	0.1072	0.0300	0.0400
1	0.9139	0.9767	4.7029	0.1122	0.0300	0.6600
2	0.9159	0.9701	4.5611	0.1095	0.0800	0.3400
3	0.9114	0.9743	4.6823	0.1109	0.1600	0.3500
4	0.9085	0.9761	4.8517	0.1068	0.0300	0.2700
Mean	0.9119	0.9736	4.6781	0.1093	0.0660	0.3320

error score. The window size of 150 ms ranks the 1^{st}. SPM analysis (Figure 4.2) showed that significant localized differences between the actual and estimated outputs occur between 1-3% GC for the position and, 83-86% GC for the moment prediction.

Table 4.2 shows the correlation coefficients, RMSE values, and SPM results of LSTMs utilizing features extracted in a window size of 150 ms. The cross-validation results demonstrate strongly correlated position and moment predictions for each trial.

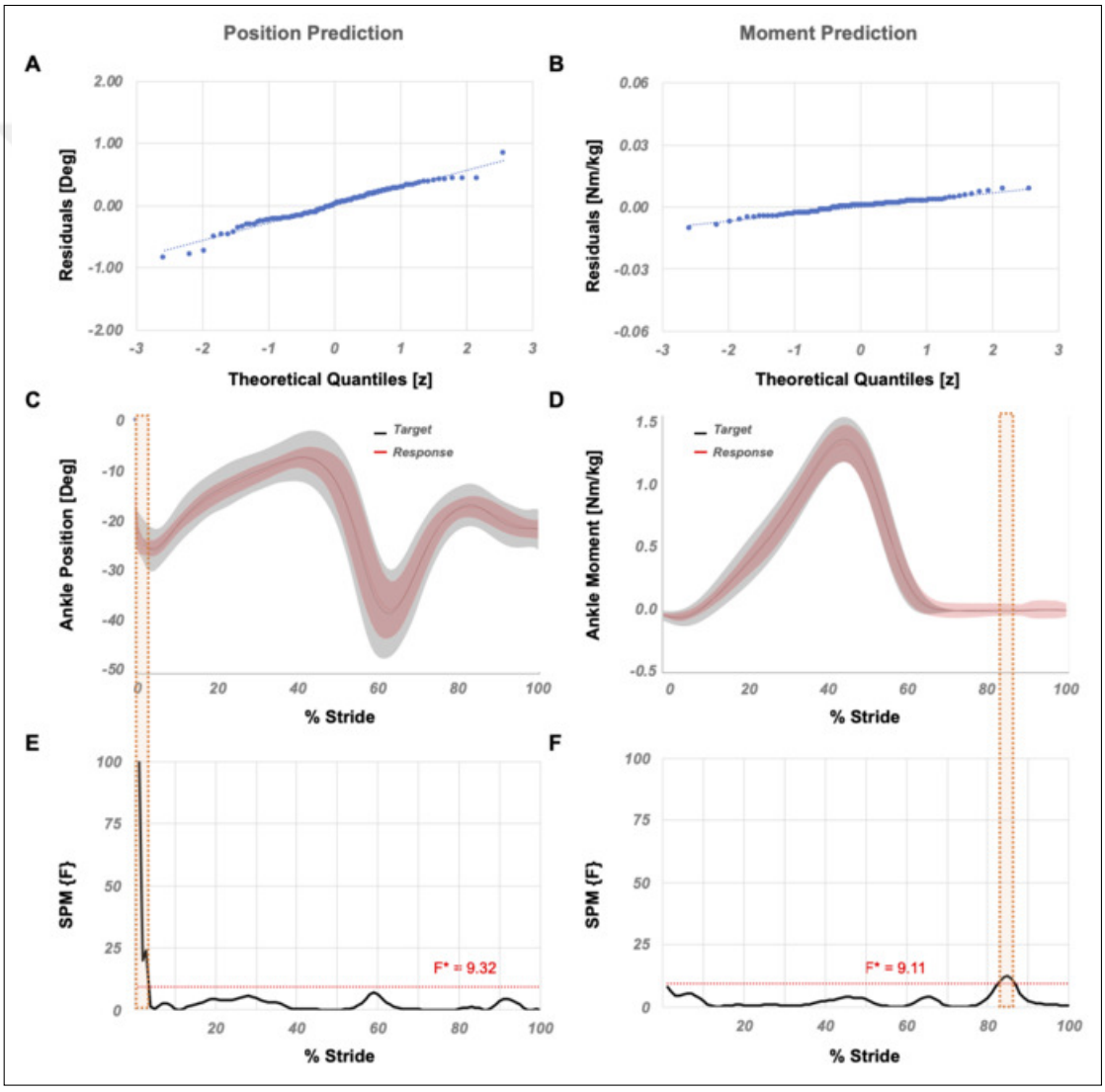


Figure 4.2 Temporal success assessment for the window size of 150 ms. The normal Q-Q plots for the residuals between original data and LSTM response for ankle (A) position and (B) moment. Mean and standard deviation of estimated NN response vs. original data for ankle (C) position and (D) moment, as a function of % stride. Statistical parametric mapping using F-statistics (SPMF) for the ankle (E) position and (F) moment as a function of % stride shows values below the threshold (i.e., for $P < 0.05$, F*position = 9.32, F*moment = 9.11). MG abbreviates medial gastrocnemius, RF abbreviates rectus femoris, and VM abbreviates vastus medialis.

4.4 Discussion

Recent advancements particularly in hardware development have improved the powered prosthesis, whereas autonomous adaptation is still needed. Souza et al. [60] indicated that myoelectric control schemes integrated within timing-based approaches could be applied for natural and seamless ambulation. In this sense, recently, we developed an LSTM-based position and moment predictor showing that ankle position and moment changes during level walking can be predicted by utilizing sEMG features extracted over non-normalized sEMG signals of leg muscles. However, the effect of the window size in sEMG features extraction on prediction accuracy was not evaluated.

The LSTM neural network architecture consists of memory blocks, enabling it to remember inputs from the past [148]. Consequently, it is suitable for predicting joint kinetics and kinematics by utilizing sEMG signals [133]. Furthermore, studies have demonstrated that integrating LSTM with sEMG feature extraction leads to improved prediction accuracy [194]. However, several parameters are to consider in the window size selection for sEMG feature extraction, such as temporal resolution [185]. A shorter window size allows for capturing rapid changes in muscle activity during dynamic movements, whereas a longer window size can be used for analyzing steady movements, as it provides a more comprehensive view of muscle activation patterns [186]. Therefore, the window size should be selected based on the application and the neural network structure to be employed [195]. In the development of a sEMG- based robotic controller for lower limb prostheses, Fleming et al. [128] highlighted the usage of window sizes ranging from 50 to 250 ms. However, it is observed that the window sizes dominantly utilized in this context are typically between 100 and 200 ms (e.g., [10, 124, 136, 196]). Therefore, we aimed to determine the best-performing window size for the features to be extracted and used as inputs to the LSTM structure that we have shown to be efficient in ankle position and moment prediction during level walking by utilizing sEMG signals of leg muscles [193]. Our previous study demonstrated that for such LSTM-based predictors, IEMG+WL features, along with the sEMG signals of MG+VM+RF yielded the best performance. In this study, we conducted a systematic analysis to evaluate the performance of LSTMs when extracting sEMG features within the window size range

of 25 to 250 ms. The results indicated that among the tested window sizes, the best performance for the proposed LSTM structure was achieved with a window size of 150 ms. This finding aligns well with existing literature in the field. The same window size was used by Huang et al., [90] in order to develop a prosthesis controller algorithm, in which eleven muscles' sEMG signals were used. From each muscle, four features were extracted and used as inputs. Suplino et al., [197] extracted sEMG features in a window size of 150 ms to make joint movement estimation using a neural network. Hajian et al., [198] used a similar approach where sEMG features are extracted in a window size of 150 ms to estimate the joint angle and velocity under isotonic, isokinetic, and dynamic conditions. Furthermore, the results demonstrated a competitive performance that is comparable to the findings reported in the literature, whereas the proposed structure predicted ankle position and moment with RMSE values of 4.56°and 0.11 Nm/kg. For joint position prediction, Huihui et al. [170], Ma et al. [133], and Farmer et al. [30] reported RMSE values of 4.80°, 4.60°, and 5.40°, respectively. Hahn and O'Keefe [89] reported an RMSE of 0.10 Nm/kg for joint moment prediction, which aligns closely with our prediction accuracy. These findings reinforce the compatibility of the proposed LSTM structure with the literature in predicting ankle position and moment.

Phinyomark et al. [153] stated the importance of a rapid decision process in sEMG-based robotic controller development, suggesting that the target output generation should be completed within a duration of 1/3 s. Accordingly, for feature extraction, a window size was recommended to be set to less than 300 ms. Similarly, She et al. [199], specified the need for a window size that ensures a response time of less than 300 ms in real-time control studies to provide a seamless prosthesis control and minimize time delay. These insights from the literature underscore the significance of selecting an appropriate window size for real-time control applications. In the evaluation of LSTMs that employed different window sizes in feature extraction, we performed a two-way ANOVA for repeated measures to assess the effect of window size on position and moment prediction. The results revealed a significant effect of window size, indicating that different window sizes in the feature extraction led to significantly different position and moment predictions. This finding underscored the importance of window size selection to optimize prediction accuracy, highlighting the

need for a ranking parameter to determine the best-performing window size. In order to rank the window sizes according to their performance, we utilized the overall error score parameter, combining correlation coefficient, RMSE, and SPM analysis that was conducted between the LSTM response and the target data. This parameter provided a comprehensive assessment for the evaluation of the effect of window size on LSTM accuracy. The correlation coefficient enabled capturing the linear relationship between the LSTM response and the target data, while the use of the RMSE facilitated the measurement of the level of discrepancy and provided a valuable measure of the accuracy of the predictions. SPM analysis provided a statistical comparison of LSTM response and target data, particularly in localizing significantly different %GC points. This enabled to identify of the points where the LSTM response deviated significantly from the target data. The result of our comprehensive analysis highlighted that the best-performing window size is 150 ms to extract sEMG features and to input the proposed LSTM structure. Therefore, the possibility of selecting a window size for enhancing the prediction accuracy that is less than 300 ms reinforced the usability and feasibility of the proposed infrastructure to be used in real-time applications [153, 199]. Cross-validation was performed to further assessment of the repeatability of the proposed structure. The results showed that the window size of 150 ms provided strongly correlated position and moment predictions in each trial ($r_{position} > 0.90$ and $r_{moment} > 0.97$). The means of the position and moment correlations were 0.9119 ± 0.003 and 0.9736 ± 0.003, showing the similarity of results produced in each trial. The mean RMSE values remained consistent and compatible with those reported in prior studies: $RMSE_{position} = 4.6781 \pm 0.1136$ and $RMSE_{moment} = 0.1093 \pm 0.0023$. Therefore, the cross-validation results demonstrated strong evidence of the repeatability of the results achieved by the proposed LSTM structure when utilizing different training and validation datasets. This finding confirmed the robustness and reliability of the proposed approach across various data samples, further validating its effectiveness in the context of the study.

The limitations of the present study need to be addressed. The LSTMs were trained, tested, and validated exclusively using data from able-bodied subjects. Unfortunately, the availability of open-access data containing non-normalized sEMG ampli-

tudes from various leg muscles, such as the one provided by Lencioni et al. [81], is rare and this limits the validation of the proposed structure with amputee data. However, Huang and Ferris [3] reported that transtibial amputees can voluntarily activate their leg muscles, with some generating activation profiles similar to those of able-bodied individuals during dorsiflexion and plantar flexion. It was also highlighted that amputees can produce consistent sEMG amplitude patterns from stride to stride, aligning with the approach employed in this study for developing LSTM models to predict ankle position and moment. Therefore, in the case of different sEMG amplitude patterns, the proposed infrastructure and the window size used in feature extraction can be adapted to data collected from amputees, facilitating patient-specific algorithm development. Furthermore, it is important to note that the present study focused on the prediction of ankle position and moment during level walking. However, the application of LSTM models can be extended to various locomotion tasks, including stair ascending and descending. For such applications, the investigation of an appropriate window size using a similar approach would be valuable. Overall, the accuracy of ankle movement predictions should be studied with a large database including non-normalized sEMG amplitudes collected from lower extremity amputees and different locomotion tasks can be adapted.

In order to facilitate natural walking, powered prostheses require autonomous adaptation, which can be achieved through the real-time implementation of joint position and moment prediction [128]. The objective of this study was to determine the best-performing window size for feature extraction, which is subsequently utilized as input for the LSTMs to predict joint movement during level-ground walking. The selected window size can facilitate seamless prosthesis control and minimize time delays by ensuring a response time of less than 300 ms [199]. Therefore, the proposed LSTM structure can be effectively implemented in real-time robotic control applications (e.g., [173]) and utilized to generate reference inputs for advanced powered prosthesis controllers, including impedance control [177, 178].

4.5 Conclusion

In this study, we conducted a systematic analysis to select the best-performing window size for feature extraction in LSTM-based joint position and moment predictors. The results demonstrated that the window size of 150 ms yielded the best performance when utilizing IEMG+WL features extracted from sEMG signals of MG+RF+VM. However, in the translation of the offline application into online applicable powered ankle prosthesis control, the present implementation needs to be extended with other movement types, followed by optimizing with data collected from amputee participants in future studies.

5. GENERAL DISCUSSION

In this thesis, neural network-based algorithms were developed to predict sagittal ankle position and moment changes during level walking in silico by utilizing sEMG signals of leg muscles and offline tests were conducted to validate the results. The research findings presented a comprehensive perspective on the utilization of neural networks and the significance of muscle selection. The initial part of the thesis made a notable contribution by exploring the implementation of neural networks with timing-based approaches and investigating the impact of different muscle inputs on the accuracy of predictions. Subsequently, the neural network approach was expanded by employing feature extraction techniques, enhancing the real-time usability of ankle position and moment predictors for robotic controllers. Additionally, the thesis discussed the selection of features for such an application. Furthermore, optimization and cross-validation were performed on the overall neural network architecture and input structures, confirming the repeatability and reliability of the proposed models and methodologies employed in the study. These enhancements ensured the thesis addressed crucial aspects of neural network-based prediction of joint position and moment during level walking, leading to valuable insights for future research and applications in this field.

5.1 Neural Network Approach

This thesis investigated the utilization of neural network architectures integrated with the time-varying approach for joint position and moment prediction. Two popular architectures were employed: time-delay neural network (TDNN) and long short-term memory (LSTM). The former utilizes sequential inputs, enabling the use of time delays and consequently storing the input history. The latter one contains a memory structure that is capable of selectively remembering signal patterns for a duration and providing outputs based on the information across time. Both architectures utilized sEMG signals as inputs, but the implementation differed. For TDNN, normalized signals were

employed, whereas, for LSTM, feature extraction was applied to the sEMG signals, which were then used as inputs.

Our findings demonstrated that both TDNN and LSTM architectures performed well in capturing the temporal dynamics of the sEMG signals for predicting joint position and moment during level walking. TDNN exhibited successful correlations ($r_{position,moment} > 0.95$) in position and moment predictions for 11 out of 31 possible input muscle combinations. This primary study emphasized the effectiveness of employing a time-varying approach, which demonstrated enhanced prediction accuracy for sEMG signal inputs. Moreover, this study provided a comprehensive analysis of muscle selection. The classification based on correlation results highlighted the crucial role of lower leg muscles in ankle position and moment predictions. Additionally, the ranking of muscle combinations based on their success offered valuable insights into the selection of muscles for further analysis and consideration. While TDNN demonstrated good precision performance, the reliance on amplitude normalization for sEMG signals might bring limitations in a real-time application. Also, it is crucial to consider a potential embedded implementation, therefore to develop an infrastructure enabling real-time and efficient integration into a robotic application. In light of these considerations, we implemented the sEMG feature extraction and started using LSTM as the infrastructure due to its efficiency in joint movement estimation by utilizing sEMG features and its proven effectiveness in embedded implementation for time series tasks (e.g., [200]). The sEMG features to be extracted as inputs were determined based on systematic analysis. Building upon the findings from TDNN, four successful muscle combinations were utilized to determine the best-performing feature combination. The results indicated that the combination of integrated EMG (IEMG) and waveform length (WL) features, commonly employed in sEMG-based prosthesis controller studies, yielded the highest prediction performance ($r_{position} > 0.90$ and $r_{moment} > 0.97$). Furthermore, an analysis of window size selection for IEMG+WL feature extraction was conducted, demonstrating that a window size of 150 ms was optimal. The cross-validation of the overall structure confirmed the repeatability and reliability of the proposed approach.

In conclusion, this thesis highlights the effectiveness of integrating a time-varying approach into neural network architectures, for accurate prediction of ankle position and moment during level walking, particularly when utilizing sEMG signals as inputs. The utilization of sEMG feature extraction as input for neural networks, rather than amplitude normalization, shows promise in making accurate predictions. The proposed structure holds promise for a wide range of applications in robotic assistive devices, such as prostheses and exoskeletons. However, it should undergo real-time testing to assess its suitability for integration into robotics controllers and to facilitate any necessary re-optimizations. Nevertheless, these findings and insights are expected to make valuable contributions to the advancement and development of future research and applications within this field.

5.2 Muscle Selection

This thesis investigated the utilization of sEMG signals of leg muscles as inputs to neural networks for predicting ankle joint movements. While sEMG signals have been used successfully as inputs for assistive upper-limb robotic controllers, a comparable approach has not yet been employed for lower limbs. One of the primary reasons for this absence is the reliance on several sEMG sensors, which adversely affects real-time usability. Additionally, existing studies on powered ankle prostheses have neglected to provide a systematic analysis of muscle selection, which has crucial importance in the development of the powered ankle prosthesis. In this study, we present a systematic analysis that ranks various muscle combinations based on their effectiveness as inputs to neural networks for predicting ankle position and moment during level walking.

Our findings supported the use of sEMG signals from leg muscles as inputs for predicting ankle joint movement. The initial study focused on normalized sEMG signals from five leg muscles: TA, MG, RF, BF, and GMax. Despite the limited number of muscles and amplitude normalization, the results provided valuable insights into muscle selection for accurate predictions. The results showed that successful position and moment predictions could be only achieved if at least one lower leg muscle was used as

input ($r_{position} > 0.95$ and $r_{moment} > 0.95$). However, this limited the applicability of the proposed approach to different amputation levels. Notably, in transtibial amputation, recording consistent or reliable sEMG signals from lower leg muscles may not be feasible if the amputation is applied closer to the knee. Therefore, the use of lower leg muscles should be limited. In light of these considerations, we expanded our muscle selection analysis to include eight muscles, consisting of four upper and lower leg muscles: TA, SO, MG, PL, RF, VM, BF, and GMax. Our results demonstrated that by implementing sEMG feature extraction, a single muscle input, PL, provided a strongly correlated prediction ($r_{position} = 0.9001$ and $r_{moment} = 0.9703$). Despite its location in the lower leg area, which poses challenges in the implementation of powered ankle prostheses, this finding holds significant importance in reducing the number of sEMG inputs for other assistive devices such as exoskeletons. Furthermore, our analysis showed that GMax+VM, which consisted of only upper leg muscle, could predict ankle position and moment with a strong correlation ($r_{position} = 0.9010$ and $r_{moment} = 0.9718$). This finding is particularly noteworthy as it not only avoids the use of lower leg muscles but also limits the overall number of sEMG inputs. Lastly, the ranking identified the best-performing muscle combination as MG+RF+VM ($r_{position} = 0.9099$ and $r_{moment} = 0.9707$). This further emphasizes the importance of incorporating lower leg muscles in ankle position and moment estimation.

In conclusion, this thesis provides a performance-based ranking of muscle combinations when utilized as inputs for neural network-based algorithms to predict ankle position and moment during level walking in silico. Furthermore, it investigates the impact of muscle selection on the accuracy of joint movement predictions, providing a comprehensive review of the findings. It is expected that the muscle combination ranking will influence the development of robotic assistive devices, such as prostheses and exoskeletons. However, given the variability in muscle physiology, conducting a subject-specific analysis in accordance with the methodology outlined in this study would prove advantageous for real-time implementation. Nevertheless, these findings and insights are expected to make significant contributions to the advancement of research in this field, particularly in terms of prioritizing the selection of input muscles.

5.3 Limitations and Future Directions

This thesis has achieved quite successful outputs by investigating the use of time-varying approach integrated neural networks and the selection of muscles to be utilized as input to predict ankle position and moment during level walking. It is expected that the outcomes will provide significant contributions to the use of sEMG signals and their implementation into neural network structures in the development of robotic assistive devices. However, the methodological limitations should be acknowledged.

In this study, the use of able-bodied data poses a limitation. In order to implement the LSTM architecture in assistive robotic systems, especially powered ankle prostheses, the proposed structure should be tested, and validated with data collected from lower limb amputees. Thus, the potential differences in muscle activation patterns can be investigated, and algorithms can be adapted accordingly, leading to more effective and personalized assistive device development. Even though there are studies reporting that transtibial amputees can voluntarily activate their leg muscles, with some generating activation profiles similar to those of able-bodied individuals during dorsiflexion and plantar flexion, a future study should involve collecting sEMG data from lower limb amputees with different levels of amputations and the data should be used in the optimization of the proposed structure.

The focus on level walking is another limitation, whereas human locomotion involves a diverse range of movements, such as running, stair accenting, and descending. The implementation of the proposed structure into a powered ankle prosthesis controller requires the LSTMs to adapt to different movements. Therefore, future studies should involve collecting gait data for a broader range of movements. Thus, a more comprehensive analysis of muscle selection can be performed in order to accurately predict ankle position and moment during a wide range of locomotion tasks. Hereby, the proposed structure can be advanced to ensure effective assistance to individuals with lower limb amputations in performing various daily tasks.

While the proposed LSTM structure demonstrated promising results in offline

implementation, the transition to real-time application is another important aspect to consider. Future studies should focus on addressing the computational and processing challenges to enable the seamless integration of the developed algorithms into real-time applications. By optimizing the algorithms and utilizing efficient computational techniques, researchers can ensure the feasibility and effectiveness of the proposed structures in real-time applications.

In conclusion, future studies should include gait data collection from amputee populations during a broader range of locomotion types, and focus on the translation of offline implementation to real-time applications. By addressing these limitations, the applicability of the proposed ankle position and moment predictors to the powered ankle prostheses can be enhanced.

APPENDIX A. VISUALIZATIONS OF CORRELATIONS BETWEEN ACTUAL VS. ESTIMATED ANKLE POSITION AND MOMENT

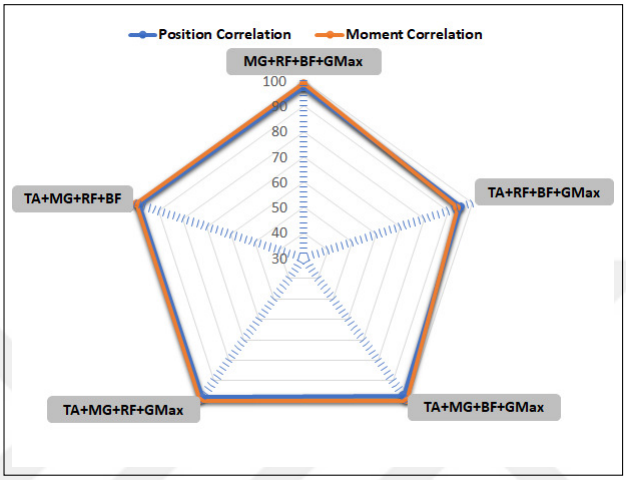


Figure A.1 Four muscle combination averaged results for the self-selected speed classes of adult and young age group. Pearson's correlation coefficients between actual vs. estimated ankle position and moment are shown. The shaded combination indicates successful variations (r > 95). TA, tibialis anterior; MG, medial gastrocnemius; RF, rectus femoris; BF, biceps femoris; GMax gluteus maximus.

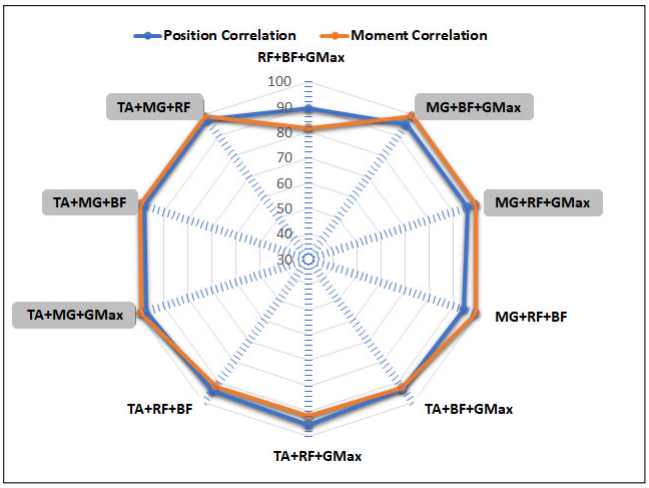


Figure A.2 Three muscle combination averaged results for the self-selected speed classes of adult and young age group. Pearson's correlation coefficients between actual vs. estimated ankle position and moment are shown. The shaded combination indicates successful variations (r > 95). TA, tibialis anterior; MG, medial gastrocnemius; RF, rectus femoris; BF, biceps femoris; GMax gluteus maximus.

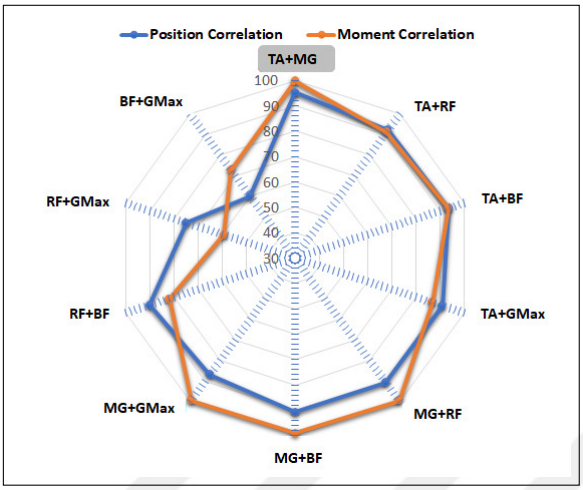


Figure A.3 Two muscle combination averaged results for the self-selected speed classes of adult and young age group. Pearson's correlation coefficients between actual vs. estimated ankle position and moment are shown. The shaded combination indicates successful variations (r > 95). TA, tibialis anterior; MG, medial gastrocnemius; RF, rectus femoris; BF, biceps femoris; GMax gluteus maximus.

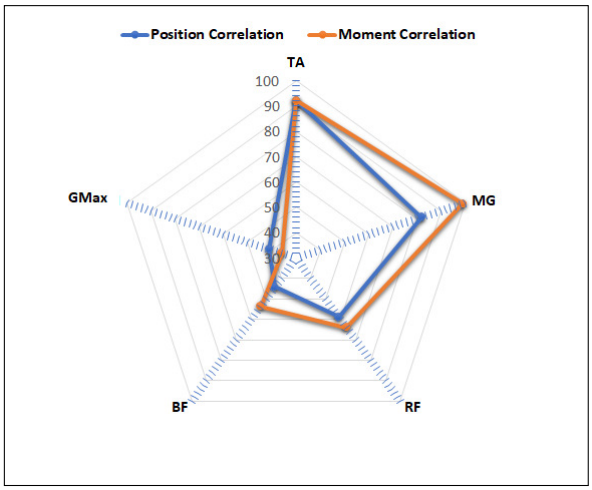


Figure A.4 Single muscle combination averaged results for the self-selected speed classes of adult and young age group. Pearson's correlation coefficients between actual vs. estimated ankle position and moment are shown. The shaded combination indicates successful variations (r > 95). TA, tibialis anterior; MG, medial gastrocnemius; RF, rectus femoris; BF, biceps femoris; GMax gluteus maximus.

APPENDIX B. VISUALIZATIONS OF EXTRACTED FEATURES

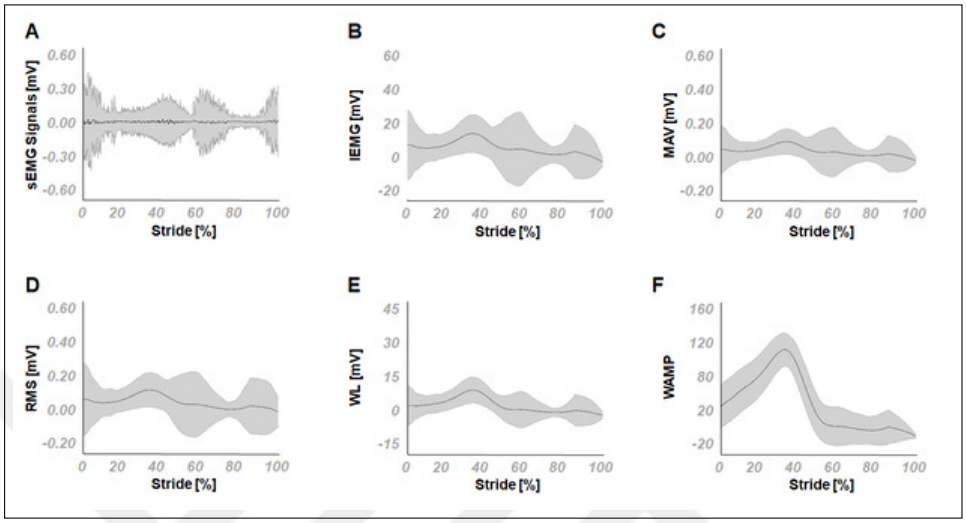


Figure B.1 Mean and standard deviation of sEMG signals and its extracted features for the soleus muscle. (A) the sEMG signals and the corresponding (B) IEMG, (C) MAV, (D) RMS, (E) WL, and (F) WAMP features.

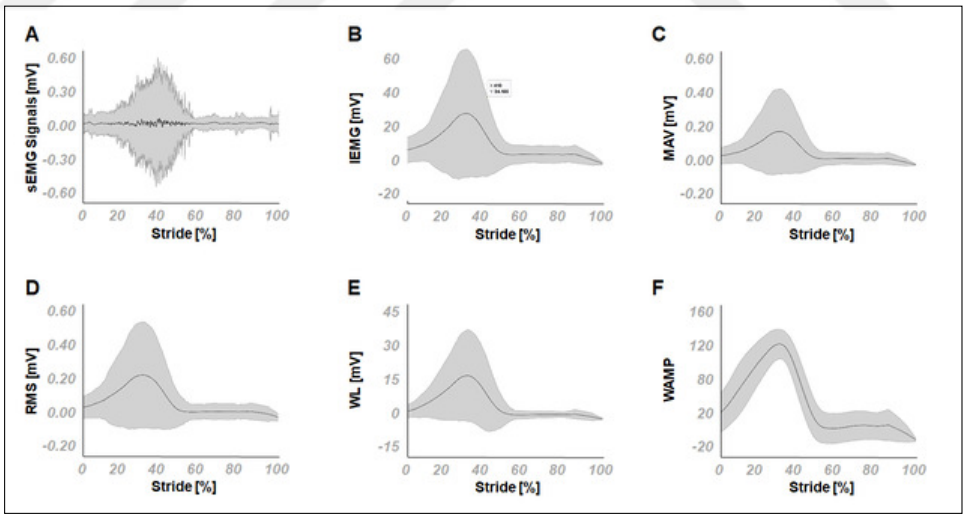


Figure B.2 Mean and standard deviation of sEMG signals and its extracted features for the medial gastrocnemius muscle. (A) the sEMG signals and the corresponding (B) IEMG, (C) MAV, (D) RMS, (E) WL, and (F) WAMP features.

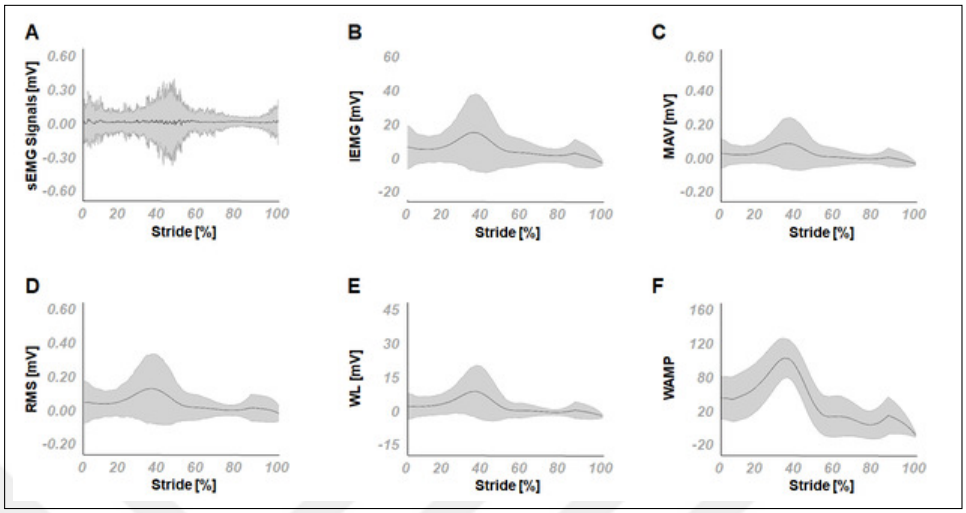


Figure B.3 Mean and standard deviation of sEMG signals and its extracted features for the peroneus longus muscle. (A) the sEMG signals and the corresponding (B) IEMG, (C) MAV, (D) RMS, (E) WL, and (F) WAMP features.

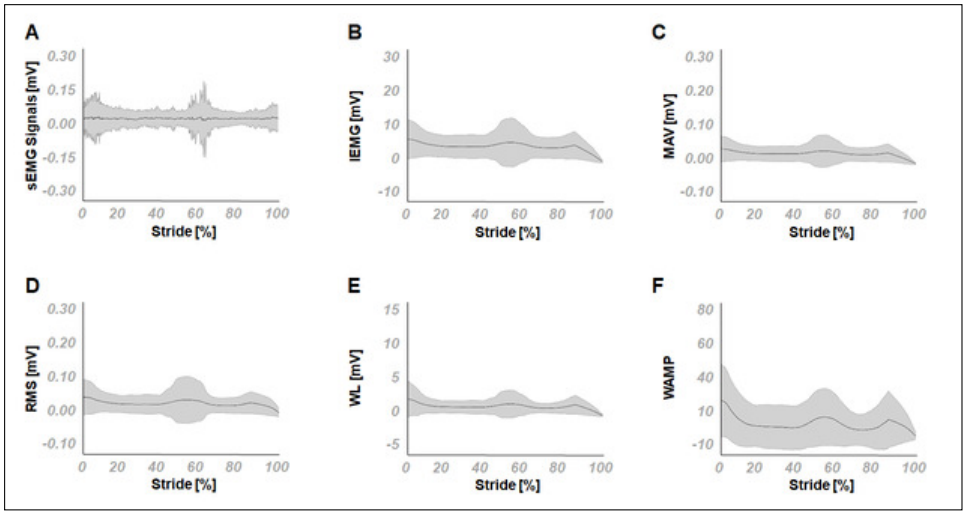


Figure B.4 Mean and standard deviation of sEMG signals and its extracted features for the rectus femoris muscle. (A) the sEMG signals and the corresponding (B) IEMG, (C) MAV, (D) RMS, (E) WL, and (F) WAMP features.

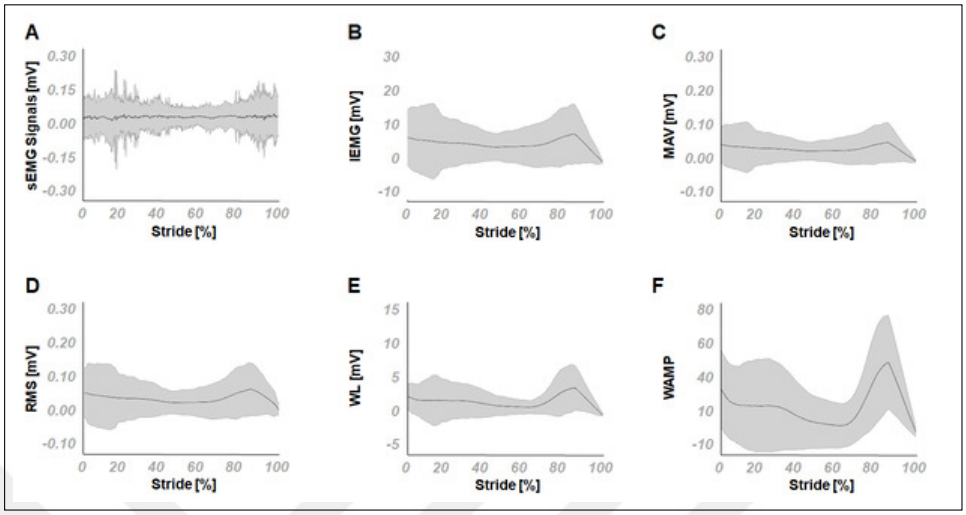


Figure B.5 Mean and standard deviation of sEMG signals and its extracted features for the biceps femoris muscle. (A) the sEMG signals and the corresponding (B) IEMG, (C) MAV, (D) RMS, (E) WL, and (F) WAMP features.

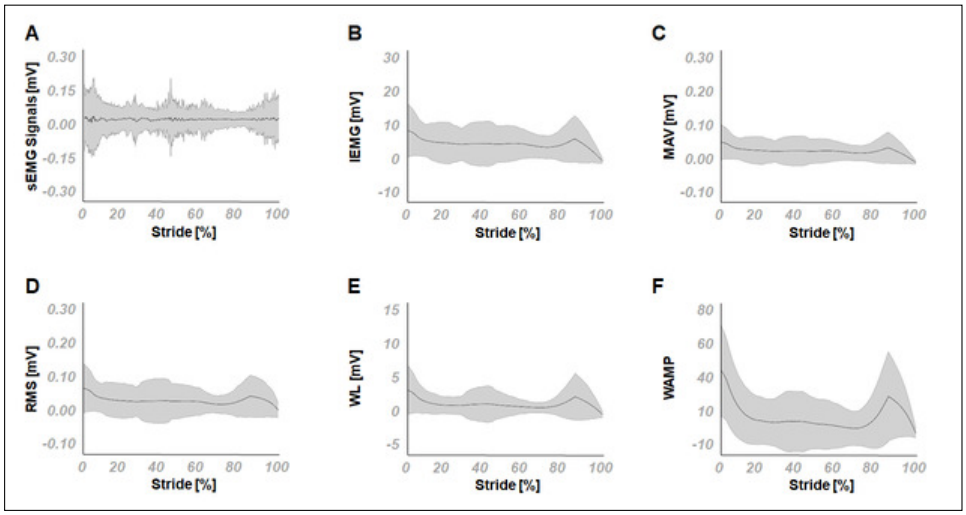


Figure B.6 Mean and standard deviation of sEMG signals and its extracted features for the vastus medialis muscle. (A) the sEMG signals and the corresponding (B) IEMG, (C) MAV, (D) RMS, (E) WL, and (F) WAMP features.

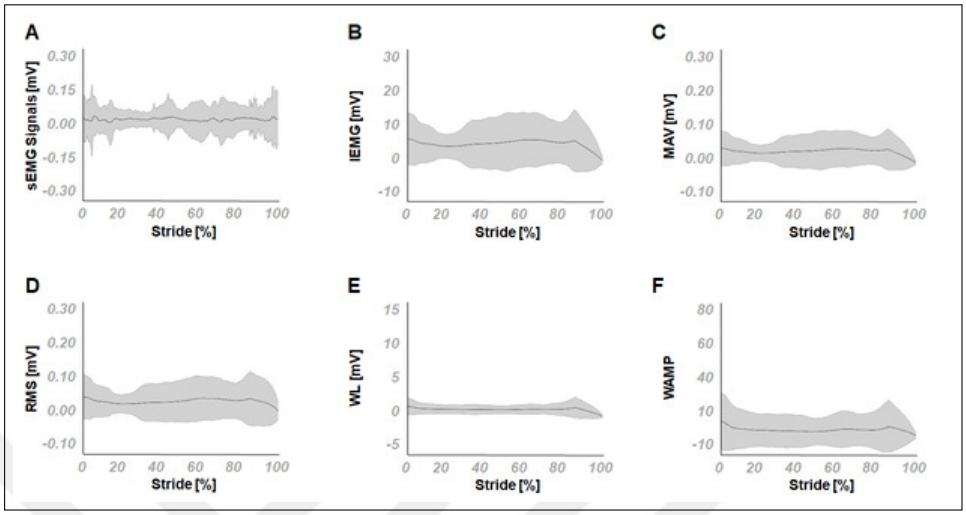


Figure B.7 Mean and standard deviation of sEMG signals and its extracted features for the gluteus maximus muscle. (A) the sEMG signals and the corresponding (B) IEMG, (C) MAV, (D) RMS, (E) WL, and (F) WAMP features.

APPENDIX C. THE COMPARISON OF MUSCLE VARIATIONS

Table C.1
The comparison of the muscle variations. Grey-shaded cells show muscle variations that do not provide strongly correlated position and moment predictions (i.e., r $<$ 0.90). Yellow-shaded cells show the only upper leg muscle variations that provide strongly correlated position and moment predictions (i.e., r $\geq$ 0.90). TA: tibialis anterior, SO: soleus, MG: medial gastrocnemius, PL: peroneus longus, RF: rectus femoris, BF: biceps femoris, VM: vastus medialis GMax: gluteus maximus, RMSE: root-mean-square error.

Rank	**Muscle Variations**	**Pos Corr [r]**	**Mom Corr [r]**	**Pos RMSE [deg]**	**Mom RMSE [Nm/kg]**	**Pos SPM [%GC]**	**Mom SPM [%GC]**	**Overall Error Score**
1	MG+RF+VM	0.9099	0.9707	4.5923	0.1072	0.0300	0.0400	0.0018
2	GMax+RF+SO	0.8978	0.9716	4.8759	0.1151	0.0500	0.0100	0.0018
3	BF+MG+GMax+PL+RF+SO	0.9134	0.9714	4.3291	0.1067	0.0700	0.0200	0.0022
4	BF+MG+GMax+RF+SO+TA+VM	0.9246	0.9803	4.1877	0.1012	0.1200	0.0000	0.0023
5	MG+GMax+PL+VM	0.9101	0.9725	4.5901	0.1085	0.1000	0.0000	0.0026
6	BF+MG+GMax	0.9006	0.9742	4.6781	0.1094	0.1000	0.0000	0.0028
7	BF+MG+GMax+PL+RF+SO+TA+VM	0.9205	0.9695	4.2841	0.1060	0.0100	0.1200	0.0030
8	MG+GMax+RF+TA	0.9123	0.9789	4.5078	0.1034	0.1100	0.0300	0.0033
9	MG+GMax+PL+RF+SO+TA	0.9267	0.9733	4.1133	0.1079	0.0500	0.1100	0.0034
10	MG+GMax+TA	0.9164	0.9782	4.4843	0.1059	0.1200	0.0300	0.0034
11	RF+TA	0.9174	0.9776	4.6396	0.1081	0.0300	0.1200	0.0035
12	MG+SO+TA	0.9197	0.9769	4.4188	0.1072	0.1100	0.0500	0.0036
13	BF+MG+GMax+PL+SO+TA	0.9166	0.9760	4.3324	0.1070	0.0200	0.1400	0.0037
14	BF+PL+RF+TA	0.9161	0.9734	4.4649	0.1119	0.1000	0.0500	0.0037
15	PL+SO+TA+VM	0.9216	0.9768	4.4417	0.1104	0.1200	0.0600	0.0040

16	MG+PL+TA	0.9203	0.9757	4.3252	0.1083	0.1200	0.0700	0.0043
17	MG+GMax+PL+RF+TA	0.9099	0.9779	4.3088	0.1068	0.1200	0.0600	0.0043
18	BF+MG+RF+SO+TA+VM	0.9169	0.9754	4.2226	0.1048	0.1400	0.0600	0.0045
19	MG+GMax+PL+RF+SO+VM	0.9136	0.9734	4.5057	0.1078	0.0900	0.1000	0.0047
20	MG+GMax+RF+SO+TA	0.9196	0.9725	4.3227	0.1090	0.0600	0.1500	0.0049
21	BF+GMax+VM	0.8904	0.9668	5.0332	0.1212	0.1300	0.0100	0.0049
22	GMax+PL+RF	0.9068	0.9689	4.7873	0.1143	0.1700	0.0000	0.0049
23	BF+MG+PL+RF	0.9102	0.9692	4.5424	0.1074	0.0800	0.1100	0.0050
24	BF+MG+GMax+PL+VM	0.9097	0.9788	4.4883	0.1065	0.1000	0.1100	0.0051
25	MG+GMax+RF+SO+VM	0.9119	0.9765	4.5431	0.1079	0.1000	0.1100	0.0052
26	BF+RF+TA	0.9164	0.9744	4.5841	0.1124	0.0600	0.1500	0.0052
27	BF+PL+SO+VM	0.9156	0.9649	4.5507	0.1183	0.0400	0.1600	0.0055
28	MG+PL+RF+SO+TA	0.9212	0.9589	4.3659	0.1113	0.1600	0.0500	0.0055
29	BF+MG+GMax+PL+SO+VM	0.9213	0.9748	4.2727	0.1077	0.0100	0.2400	0.0055
30	BF+MG+VM	0.9201	0.9769	4.4867	0.1083	0.0300	0.2300	0.0059
31	MG+PL+RF+SO+TA+VM	0.9243	0.9766	4.3333	0.1037	0.2000	0.0900	0.0061
32	MG+GMax+SO+TA	0.9179	0.9709	4.4712	0.1081	0.2000	0.0500	0.0061
33	BF+MG+GMax+RF+VM	0.9113	0.9638	4.4414	0.1131	0.0200	0.2000	0.0061
34	BF+MG+RF+TA+VM	0.9230	0.9780	4.4489	0.1038	0.2900	0.0000	0.0061
35	MG+GMax+PL+RF	0.9087	0.9723	4.5340	0.1130	0.1500	0.0800	0.0062

36	MG+GMax+PL+TA	0.9182	0.9721	4.3893	0.1106	0.1600	0.1000	0.0062
37	MG+PL+SO	0.9181	0.9691	4.4428	0.1119	0.0600	0.1900	0.0063
38	BF+RF+SO+TA+VM	0.9222	0.9610	4.3213	0.1164	0.1500	0.0900	0.0063
39	BF+MG+SO+TA	0.9242	0.9774	4.2392	0.1074	0.0200	0.2800	0.0063
40	BF+MG+GMax+TA+VM	0.9196	0.9714	4.4385	0.1091	0.0300	0.2400	0.0064
41	SO+TA+VM	0.9240	0.9774	4.4253	0.1081	0.0100	0.3000	0.0066
42	BF+MG+PL+TA+VM	0.9282	0.9751	4.2314	0.1064	0.1400	0.1900	0.0067
43	GMax+SO+VM	0.9036	0.9719	4.8336	0.1130	0.0500	0.1900	0.0069
44	BF+GMax+SO+VM	0.9082	0.9735	4.6375	0.1145	0.1900	0.0700	0.0070
45	SO+VM	0.9102	0.9757	4.7049	0.1126	0.0500	0.2300	0.0073
46	BF+MG+PL+RF+VM	0.9055	0.9714	4.5869	0.1076	0.1900	0.0800	0.0073
47	MG+PL+SO+TA+VM	0.9261	0.9749	4.1641	0.1090	0.0500	0.3000	0.0073
48	BF+MG+PL+RF+SO	0.9011	0.9738	4.4659	0.1073	0.1400	0.1300	0.0073
49	BF+MG+RF+VM	0.9133	0.9784	4.4769	0.1036	0.0600	0.2600	0.0074
50	BF+GMax+SO	0.9162	0.9688	4.5551	0.1186	0.0300	0.2500	0.0074
51	BF+MG+RF+SO+TA	0.9200	0.9801	4.3880	0.1006	0.2000	0.1600	0.0075
52	GMax+RF+TA	0.9069	0.9725	4.7159	0.1144	0.0300	0.2400	0.0075
53	GMax+PL+SO+TA+VM	0.9192	0.9783	4.4630	0.1067	0.0500	0.2900	0.0076
54	BF+MG+GMax+RF+SO+VM	0.9095	0.9772	4.5465	0.1058	0.1900	0.1200	0.0077
55	MG+GMax	0.8951	0.9762	4.8409	0.1098	0.0300	0.2300	0.0077

56	MG+PL+RF+VM	0.9116	0.9798	4.5032	0.1040	0.1300	0.2000	0.0077
57	BF+MG+PL+SO+VM	0.9190	0.9709	4.4087	0.1104	0.1800	0.1400	0.0077
58	GMax+RF	0.8916	0.9687	5.0415	0.1175	0.1200	0.1100	0.0078
59	MG+GMax+PL+TA+VM	0.9095	0.9764	4.4972	0.1043	0.2000	0.1200	0.0079
60	MG+GMax+SO+VM	0.9138	0.9754	4.4813	0.1124	0.1100	0.2100	0.0079
61	GMax+PL+VM	0.9069	0.9706	4.7042	0.1152	0.1600	0.1200	0.0079
62	BF+MG+GMax+RF+SO	0.9057	0.9704	4.5828	0.1088	0.2600	0.0300	0.0080
63	BF+MG+PL+RF+SO+TA	0.9232	0.9763	4.3223	0.1053	0.1000	0.2800	0.0081
64	PL+TA+VM	0.9148	0.9753	4.5563	0.1138	0.0700	0.2600	0.0082
65	BF+GMax+TA	0.9134	0.9707	4.6710	0.1160	0.0700	0.2400	0.0083
66	RF+SO+TA	0.9158	0.9678	4.5163	0.1138	0.1600	0.1700	0.0087
67	GMax+RF+TA+VM	0.9223	0.9627	4.4178	0.1196	0.0200	0.3100	0.0087
68	MG+GMax+RF	0.8994	0.9768	4.8072	0.1086	0.1400	0.1700	0.0087
69	PL	0.9001	0.9703	4.9396	0.1190	0.1100	0.1700	0.0087
70	GMax+SO	0.8879	0.9708	4.9708	0.1177	0.0900	0.1700	0.0088
71	BF+MG+TA	0.9199	0.9787	4.4577	0.1028	0.1400	0.2700	0.0088
72	BF+PL+TA+VM	0.9162	0.9727	4.5415	0.1166	0.1800	0.1700	0.0089
73	BF+MG+GMax+RF+TA	0.9161	0.9739	4.2673	0.1080	0.0200	0.3600	0.0089
74	GMax	0.8792	0.9732	5.1680	0.1161	0.0800	0.1700	0.0090
75	GMax+PL+RF+SO+VM	0.9104	0.9703	4.6538	0.1145	0.2600	0.0700	0.0090

76	MG+RF+TA	0.9202	0.9806	4.4075	0.0999	0.1900	0.2500	0.0091
77	MG+RF+SO+TA+VM	0.9078	0.9772	4.5132	0.1048	0.2900	0.0800	0.0092
78	MG+RF+SO+TA	0.9144	0.9775	4.4121	0.1041	0.2500	0.1500	0.0092
79	BF+MG+GMax+PL+TA	0.9117	0.9722	4.4084	0.1116	0.0300	0.3300	0.0092
80	GMax+PL+RF+VM	0.9084	0.9718	4.7488	0.1165	0.2100	0.1200	0.0092
81	BF+MG+PL+VM	0.9115	0.9748	4.5681	0.1072	0.3400	0.0300	0.0093
82	MG+TA+VM	0.9235	0.9813	4.3535	0.1003	0.1900	0.2800	0.0093
83	BF+MG+GMax+PL+SO+TA+VM	0.9106	0.9759	4.3949	0.1070	0.2300	0.1500	0.0093
84	RF+SO+TA+VM	0.9237	0.9720	4.4245	0.1136	0.2500	0.1500	0.0093
85	SO	0.9002	0.9756	4.8927	0.1144	0.1300	0.1900	0.0093
86	BF+RF+SO+TA	0.9130	0.9753	4.6492	0.1119	0.3100	0.0600	0.0094
87	BF+TA+VM	0.9194	0.9694	4.5901	0.1157	0.0900	0.2800	0.0094
88	MG+RF	0.9081	0.9793	4.7208	0.1041	0.2600	0.1200	0.0094
89	MG+GMax+RF+SO	0.9066	0.9756	4.7051	0.1076	0.2800	0.0800	0.0095
90	BF+GMax+RF	0.8953	0.9686	5.0077	0.1187	0.1300	0.1600	0.0096
91	MG+GMax+PL+SO+VM	0.9177	0.9645	4.3902	0.1157	0.0400	0.3300	0.0098
92	BF+MG+SO+VM	0.9114	0.9807	4.5606	0.1034	0.1500	0.2700	0.0098
93	MG+PL+RF+TA+VM	0.9172	0.9766	4.4166	0.1068	0.0800	0.3500	0.0099
94	BF+GMax+PL+RF+TA+VM	0.9195	0.9706	4.4626	0.1112	0.4100	0.0000	0.0100
95	PL+RF+SO+TA+VM	0.9269	0.9759	4.2195	0.1112	0.2000	0.2800	0.0101

96	BF+PL+RF+VM	0.9114	0.9704	4.5794	0.1170	0.0600	0.3100	0.0101
97	GMax+PL+RF+TA	0.9147	0.9690	4.5329	0.1167	0.0300	0.3500	0.0101
98	BF+MG+GMax+SO	0.8995	0.9778	4.5888	0.1099	0.0600	0.3100	0.0101
99	MG+PL	0.9119	0.9800	4.6220	0.1050	0.1900	0.2400	0.0102
100	BF+MG+SO+TA+VM	0.9161	0.9789	4.3361	0.1026	0.2800	0.1900	0.0103
101	PL+VM	0.8993	0.9765	4.8307	0.1135	0.1000	0.2600	0.0104
102	GMax+SO+TA	0.9194	0.9659	4.4673	0.1168	0.0600	0.3400	0.0104
103	BF+GMax+PL+RF+TA	0.9230	0.9718	4.3901	0.1091	0.3300	0.1300	0.0105
104	GMax+PL+RF+SO+TA+VM	0.9284	0.9716	4.2607	0.1144	0.0600	0.4200	0.0105
105	BF+TA	0.9107	0.9771	4.6781	0.1096	0.0800	0.3400	0.0106
106	GMax+VM	0.9010	0.9718	4.8927	0.1193	0.0900	0.2600	0.0107
107	BF+PL+SO	0.9112	0.9724	4.5474	0.1174	0.0900	0.3100	0.0107
108	GMax+RF+SO+TA+VM	0.9223	0.9723	4.4744	0.1127	0.1200	0.3400	0.0108
109	BF+PL+RF+SO+TA+VM	0.9152	0.9777	4.3794	0.1072	0.0300	0.4400	0.0108
110	BF+GMax+RF+SO+TA+VM	0.9245	0.9533	4.2731	0.1225	0.0900	0.3000	0.0109
111	BF+PL+RF+SO	0.9152	0.9727	4.5216	0.1159	0.1900	0.2400	0.0110
112	BF+MG+PL+SO+TA	0.9138	0.9741	4.3300	0.1062	0.4300	0.0300	0.0110
113	BF+GMax+PL+RF+VM	0.9121	0.9664	4.5633	0.1205	0.0600	0.3300	0.0111
114	BF+GMax+PL+SO	0.9132	0.9693	4.6473	0.1161	0.3200	0.0900	0.0111
115	BF+MG	0.9045	0.9738	4.6379	0.1101	0.0700	0.3400	0.0112

116	BF+GMax+RF+TA	0.9188	0.9682	4.5879	0.1174	0.2400	0.1900	0.0112
117	PL+SO	0.9057	0.9714	4.7651	0.1169	0.0300	0.3600	0.0112
118	GMax+PL+SO+VM	0.9121	0.9679	4.5963	0.1217	0.0500	0.3500	0.0113
119	GMax+PL+RF+SO	0.9075	0.9679	4.6804	0.1195	0.0500	0.3400	0.0114
120	GMax+PL+TA+VM	0.9237	0.9712	4.4970	0.1118	0.2500	0.2400	0.0115
121	BF+GMax+RF+SO+VM	0.9120	0.9642	4.5707	0.1193	0.2300	0.1700	0.0115
122	BF+PL+SO+TA+VM	0.9037	0.9720	4.6591	0.1108	0.3300	0.0800	0.0115
123	BF+MG+GMax+SO+TA+VM	0.9144	0.9792	4.4039	0.1041	0.3700	0.1400	0.0115
124	MG+GMax+RF+VM	0.9107	0.9644	4.6398	0.1124	0.3100	0.1100	0.0119
125	BF+MG+GMax+VM	0.8951	0.9730	4.8059	0.1099	0.2400	0.1600	0.0120
126	GMax+TA	0.9006	0.9765	4.8459	0.1104	0.1500	0.2800	0.0121
127	PL+RF+TA	0.9202	0.9671	4.4449	0.1196	0.0300	0.4400	0.0122
128	BF+GMax+RF+TA+VM	0.9125	0.9709	4.5796	0.1149	0.0300	0.4300	0.0122
129	GMax+PL+TA	0.9138	0.9771	4.7428	0.1118	0.4900	0.0000	0.0122
130	BF+MG+GMax+PL+TA+VM	0.9226	0.9754	4.2228	0.1071	0.0600	0.5100	0.0123
131	BF+MG+GMax+RF+TA+VM	0.9175	0.9769	4.4509	0.1061	0.5000	0.0400	0.0123
132	BF+SO	0.9021	0.9716	4.7949	0.1146	0.4100	0.0100	0.0124
133	MG+GMax+RF+SO+TA+VM	0.9138	0.9752	4.3504	0.1072	0.3700	0.1600	0.0126
134	MG+GMax+PL+RF+VM	0.9167	0.9750	4.5352	0.1092	0.2400	0.2900	0.0127
135	SO+TA	0.9158	0.9743	4.6204	0.1134	0.1900	0.3200	0.0127

136	MG+GMax+PL+RF+SO+TA+VM	0.9292	0.9735	4.1895	0.1048	0.1500	0.4800	0.0128
137	MG+TA	0.9189	0.9751	4.5525	0.1109	0.0500	0.4900	0.0128
138	MG+GMax+VM	0.9122	0.9761	4.6217	0.1077	0.2600	0.2600	0.0129
139	BF+MG+GMax+PL+RF+SO+TA	0.9200	0.9743	4.2649	0.1041	0.4700	0.1200	0.0131
140	TA+VM	0.9075	0.9755	4.7518	0.1153	0.1500	0.3300	0.0131
141	BF+MG+GMax+RF+SO+TA	0.9143	0.9769	4.4894	0.1076	0.0600	0.4900	0.0131
142	BF+MG+RF+TA	0.9131	0.9779	4.4694	0.1043	0.3100	0.2500	0.0131
143	BF+RF+SO	0.9065	0.9711	4.6543	0.1155	0.1600	0.3100	0.0133
144	MG+SO	0.9113	0.9705	4.6072	0.1112	0.2300	0.2700	0.0133
145	BF+GMax+PL+RF	0.9022	0.9710	4.6566	0.1135	0.0700	0.3900	0.0133
146	MG+PL+RF+TA	0.9193	0.9648	4.4062	0.1166	0.1100	0.4000	0.0133
147	MG+SO+TA+VM	0.9166	0.9763	4.4269	0.1067	0.2300	0.3500	0.0134
148	BF+VM	0.8981	0.9727	4.9269	0.1170	0.0700	0.3700	0.0136
149	BF+GMax+RF+SO	0.9016	0.9649	4.7697	0.1190	0.0600	0.3700	0.0136
150	MG+VM	0.9070	0.9778	4.6597	0.1080	0.2500	0.2800	0.0136
151	MG+GMax+PL+RF+TA+VM	0.9243	0.9710	4.2112	0.1091	0.2400	0.3700	0.0136
152	BF+GMax+PL+VM	0.9092	0.9716	4.6980	0.1185	0.1700	0.3200	0.0137
153	BF+GMax	0.8899	0.9726	5.0756	0.1197	0.0700	0.3400	0.0138
154	BF+GMax+RF+VM	0.9018	0.9659	4.8817	0.1186	0.3300	0.1100	0.0139
155	BF+GMax+PL+TA+VM	0.9242	0.9763	4.3350	0.1086	0.4600	0.1900	0.0139

156	BF+PL+RF+SO+TA	0.9150	0.9708	4.5093	0.1149	0.1200	0.4200	0.0140
157	GMax+PL+RF+TA+VM	0.9231	0.9716	4.4577	0.1113	0.4900	0.1100	0.0140
158	BF+PL	0.9042	0.9693	4.7680	0.1177	0.0900	0.3800	0.0140
159	BF+GMax+PL+SO+TA+VM	0.9127	0.9708	4.3699	0.1164	0.2000	0.3400	0.0141
160	BF+MG+RF+SO	0.9065	0.9789	4.6332	0.1027	0.4400	0.1300	0.0142
161	BF+MG+GMax+PL	0.8995	0.9675	4.6550	0.1120	0.2800	0.1900	0.0142
162	BF+MG+GMax+PL+RF+TA+VM	0.9183	0.9719	4.3469	0.1086	0.2000	0.4000	0.0142
163	GMax+PL+SO	0.9138	0.9739	4.6431	0.1162	0.2100	0.3400	0.0143
164	PL+RF+SO+TA	0.9141	0.9748	4.4986	0.1123	0.2300	0.3500	0.0144
165	GMax+PL	0.9015	0.9753	4.9124	0.1142	0.2000	0.3000	0.0145
166	PL+RF+SO+VM	0.9145	0.9703	4.5870	0.1205	0.0500	0.4900	0.0146
167	GMax+SO+TA+VM	0.9161	0.9744	4.5157	0.1115	0.1300	0.4700	0.0147
168	RF+SO+VM	0.9091	0.9751	4.7473	0.1135	0.1200	0.4300	0.0147
169	PL+RF+VM	0.9129	0.9733	4.6622	0.1167	0.0500	0.5100	0.0148
170	MG+PL+VM	0.9096	0.9727	4.6637	0.1137	0.1000	0.4500	0.0148
171	BF+MG+RF+SO+VM	0.9139	0.9777	4.3484	0.1108	0.0900	0.5400	0.0149
172	MG+PL+SO+VM	0.9148	0.9769	4.4736	0.1093	0.1100	0.5200	0.0150
173	PL+RF+TA+VM	0.9234	0.9601	4.4455	0.1168	0.4700	0.1000	0.0151
174	MG+PL+RF+SO+VM	0.9126	0.9767	4.4760	0.1094	0.2300	0.3900	0.0151
175	GMax+TA+VM	0.9090	0.9714	4.6330	0.1182	0.1700	0.3800	0.0153

176	BF	0.8809	0.9736	5.1351	0.1181	0.1800	0.2500	0.0153
177	BF+MG+RF	0.9039	0.9781	4.6485	0.1069	0.3900	0.2000	0.0154
178	BF+RF+VM	0.8948	0.9724	4.9445	0.1157	0.2600	0.2300	0.0155
179	BF+GMax+PL+RF+SO+TA+VM	0.9196	0.9681	4.4045	0.1169	0.1400	0.4700	0.0155
180	BF+GMax+PL+RF+SO	0.9082	0.9723	4.6203	0.1159	0.1800	0.3900	0.0157
181	MG+RF+SO+VM	0.9136	0.9777	4.5355	0.1051	0.2300	0.4400	0.0158
182	BF+SO+VM	0.9086	0.9695	4.6771	0.1181	0.0800	0.4900	0.0162
183	BF+MG+TA+VM	0.9235	0.9808	4.3637	0.1022	0.4000	0.4100	0.0163
184	MG+RF+TA+VM	0.9185	0.9722	4.4456	0.1128	0.1100	0.5600	0.0163
185	BF+GMax+PL+TA	0.8991	0.9676	4.7726	0.1142	0.3000	0.2300	0.0164
186	BF+MG+GMax+TA	0.9073	0.9778	4.4505	0.1081	0.2100	0.4500	0.0165
187	RF	0.8871	0.9746	5.0989	0.1146	0.3100	0.1900	0.0166
188	MG+GMax+SO	0.9036	0.9731	4.7810	0.1121	0.2500	0.3400	0.0167
189	MG	0.8993	0.9781	4.7901	0.1105	0.0500	0.5500	0.0168
190	PL+RF+SO	0.9050	0.9748	4.7897	0.1164	0.1400	0.4600	0.0169
191	GMax+RF+VM	0.8991	0.9681	4.9157	0.1201	0.1200	0.4100	0.0170
192	MG+GMax+PL+SO	0.9092	0.9622	4.6712	0.1168	0.0800	0.4900	0.0170
193	GMax+RF+SO+TA	0.9156	0.9692	4.6700	0.1165	0.2600	0.3800	0.0171
194	GMax+RF+SO+VM	0.9123	0.9697	4.6599	0.1165	0.0300	0.6000	0.0172
195	BF+GMax+PL+SO+TA	0.9163	0.9715	4.4266	0.1168	0.1700	0.5100	0.0173

196	BF+SO+TA+VM	0.9135	0.9703	4.6599	0.1125	0.5900	0.0700	0.0174
197	BF+MG+GMax+PL+RF+SO+VM	0.9005	0.9803	4.5170	0.1021	0.2900	0.4000	0.0176
198	BF+PL+RF+TA+VM	0.9170	0.9688	4.5476	0.1173	0.2600	0.4100	0.0176
199	TA	0.8998	0.9750	4.8687	0.1149	0.2200	0.3900	0.0179
200	PL+SO+TA	0.9078	0.9723	4.6312	0.1156	0.5800	0.0800	0.0182
201	BF+GMax+SO+TA	0.9201	0.9603	4.3864	0.1195	0.0500	0.6200	0.0183
202	MG+PL+RF	0.8999	0.9761	4.7546	0.1113	0.1600	0.4900	0.0184
203	BF+PL+RF+SO+VM	0.9125	0.9710	4.4740	0.1159	0.2600	0.4400	0.0185
204	MG+RF+SO	0.9119	0.9736	4.5912	0.1139	0.0700	0.6400	0.0185
205	MG+GMax+PL+SO+TA	0.9214	0.9743	4.3686	0.1125	0.3800	0.4300	0.0186
206	PL+RF	0.9019	0.9736	4.8592	0.1156	0.0800	0.5600	0.0188
207	BF+MG+PL+RF+TA	0.9129	0.9729	4.3756	0.1063	0.1200	0.6500	0.0188
208	VM	0.8953	0.9726	4.9771	0.1194	0.0600	0.5300	0.0189
209	MG+GMax+SO+TA+VM	0.9194	0.9764	4.4658	0.1068	0.2700	0.5700	0.0190
210	BF+MG+PL+RF+SO+TA+VM	0.9192	0.9731	4.3243	0.1041	0.5900	0.2500	0.0191
211	BF+MG+SO	0.8959	0.9769	4.8227	0.1075	0.4700	0.2100	0.0196
212	BF+GMax+RF+SO+TA	0.9086	0.9707	4.5512	0.1134	0.3000	0.4200	0.0196
213	MG+GMax+TA+VM	0.9084	0.9761	4.5561	0.1092	0.4900	0.2800	0.0197
214	BF+RF+TA+VM	0.9191	0.9745	4.4867	0.1160	0.2900	0.5300	0.0198
215	BF+GMax+SO+TA+VM	0.9183	0.9686	4.4643	0.1172	0.3500	0.4200	0.0198

216	BF+GMax+TA+VM	0.9146	0.9662	4.6088	0.1175	0.2700	0.4500	0.0199
217	MG+PL+TA+VM	0.9225	0.9802	4.3471	0.1018	0.4700	0.5100	0.0199
218	PL+TA	0.9140	0.9768	4.7066	0.1125	0.3000	0.5000	0.0200
219	BF+GMax+PL+RF+SO+TA	0.9158	0.9722	4.4553	0.1131	0.3800	0.4200	0.0200
220	BF+MG+GMax+PL+RF+TA	0.9142	0.9709	4.4338	0.1144	0.3500	0.4300	0.0201
221	BF+MG+GMax+SO+TA	0.9126	0.9734	4.5817	0.1083	0.6500	0.1500	0.0202
222	BF+SO+TA	0.9201	0.9666	4.4315	0.1190	0.2600	0.5200	0.0202
223	BF+GMax+PL+SO+VM	0.9095	0.9694	4.5912	0.1157	0.2300	0.5000	0.0203
224	RF+SO	0.9059	0.9762	4.8538	0.1140	0.2800	0.4800	0.0209
225	BF+PL+VM	0.9109	0.9740	4.6526	0.1163	0.1500	0.6500	0.0213
226	BF+GMax+PL	0.9083	0.9703	4.7530	0.1186	0.4500	0.3000	0.0215
227	BF+MG+PL+TA	0.9195	0.9758	4.3042	0.1110	0.4500	0.5100	0.0218
228	GMax+PL+RF+SO+TA	0.9195	0.9710	4.4721	0.1169	0.4700	0.4100	0.0219
229	MG+GMax+PL+RF+SO	0.9042	0.9749	4.8711	0.1101	0.7600	0.0400	0.0223
230	BF+MG+GMax+PL+RF	0.9128	0.9699	4.5079	0.1139	0.3300	0.5200	0.0225
231	BF+MG+GMax+RF	0.9012	0.9657	4.6182	0.1111	0.5500	0.2000	0.0225
232	PL+SO+VM	0.9165	0.9777	4.6493	0.1118	0.4800	0.4600	0.0225
233	MG+PL+RF+SO	0.9075	0.9706	4.6334	0.1075	0.5800	0.2600	0.0227
234	BF+RF	0.8938	0.9735	5.0281	0.1170	0.2800	0.4500	0.0233
235	MG+GMax+PL	0.8927	0.9750	4.9577	0.1141	0.4500	0.3200	0.0241

236	BF+RF+SO+VM	0.9056	0.9688	4.7433	0.1169	0.4700	0.3500	0.0241
237	MG+SO+VM	0.9091	0.9799	4.6322	0.1097	0.4000	0.5700	0.0241
238	BF+MG+PL+RF+SO+VM	0.9172	0.9715	4.4573	0.1118	0.5000	0.4800	0.0242
239	BF+MG+GMax+SO+VM	0.9089	0.9767	4.6934	0.1096	0.6300	0.3500	0.0253
240	BF+MG+GMax+PL+SO	0.9026	0.9731	4.7924	0.1119	0.6600	0.2300	0.0255
241	BF+PL+SO+TA	0.9102	0.9704	4.5975	0.1182	0.5500	0.3900	0.0260
242	BF+PL+TA	0.9196	0.9737	4.5939	0.1143	0.5600	0.5200	0.0262
243	GMax+PL+SO+TA	0.9133	0.9735	4.6736	0.1158	0.5100	0.5500	0.0277
244	MG+GMax+RF+TA+VM	0.9082	0.9793	4.5153	0.1044	0.5600	0.5900	0.0279
245	BF+PL+RF	0.8929	0.9757	4.8344	0.1146	0.3100	0.6200	0.0286
246	MG+PL+SO+TA	0.9121	0.9732	4.4892	0.1118	0.5300	0.6000	0.0289
247	RF+VM	0.9009	0.9712	4.8933	0.1181	0.3900	0.5800	0.0296
248	BF+GMax+PL+RF+SO+VM	0.9075	0.9686	4.7066	0.1138	0.5700	0.5200	0.0311
249	RF+TA+VM	0.8905	0.9717	4.9624	0.1169	0.3600	0.5900	0.0313
250	BF+MG+PL+RF+TA+VM	0.8889	0.9724	4.8497	0.1097	0.7000	0.3200	0.0324
251	BF+MG+PL+SO	0.9120	0.9705	4.5136	0.1146	0.5100	0.7400	0.0332
252	BF+MG+PL	0.9065	0.9698	4.5834	0.1201	0.3200	0.8400	0.0335
253	BF+MG+PL+SO+TA+VM	0.9076	0.9744	4.8778	0.1088	0.8800	0.4300	0.0354
254	MG+GMax+PL+SO+TA+VM	0.9119	0.9654	4.7634	0.1110	0.7600	0.6000	0.0381
255	BF+MG+GMax+PL+RF+VM	0.8988	0.9655	4.7963	0.1195	0.7200	0.7700	0.0481

APPENDIX D. THE VERSATILITY IMPLEMENTATION FOR SEMG FEATURE SELECTION

Table D.1

The comparison of the sEMG feature variations calculated over MG+TA. Green shaded cells show the feature variations that provide strongly correlated position and moment predictions (i.e., r $\geq$ 0.90). MG: medial gastrocnemius, TA: tibialis anterior, IEMG: integrated EMG, MAV: mean absolute value, WAMP: Willison amplitude, RMS: root mean square; WL: waveform length.

Rank	sEMG Feature Variations	Pos Corr [r]	Mom Corr [r]	Pos RMSE [deg]	Mom RMSE [Nm/kg]	Pos SPM [%GC]	Mom SPM [%GC]	Overall Error Score
1	WL	0.8894	0.9789	5.0765	0.1059	0.1100	0.0300	0.0030
2	RMS+WL	0.8875	0.9767	5.1379	0.1100	0.1400	0.1800	0.0072
3	MAV+RMS+WL	0.8990	0.9757	4.9453	0.1122	0.0500	0.3500	0.0083
4	IEMG+RMS+WL	0.8949	0.9765	4.9346	0.1092	0.0700	0.3400	0.0086
5	IEMG+WL	0.9189	0.9751	4.5525	0.1109	0.0500	0.4900	0.0091
6	IEMG+MAV+RMS+WAMP	0.9138	0.9652	4.5818	0.1260	0.1000	0.3400	0.0092
7	WAMP	0.9154	0.9744	4.6681	0.1159	0.1500	0.4100	0.0102
8	MAV+RMS+WAMP+WL	0.9144	0.9617	4.5990	0.1351	0.1000	0.4000	0.0112
9	RMS+WAMP+WL	0.9031	0.9709	4.7727	0.1184	0.3200	0.2200	0.0115
10	IEMG+RMS+WAMP+WL	0.9126	0.9723	4.5823	0.1186	0.1100	0.4900	0.0115
11	MAV+RMS+WAMP	0.9125	0.9746	4.6416	0.1183	0.1400	0.5000	0.0121
12	IEMG+MAV+WL	0.8962	0.9740	4.9484	0.1117	0.3600	0.2100	0.0122
13	IEMG	0.8742	0.9776	5.3140	0.1097	0.3700	0.1400	0.0127
14	MAV+WAMP	0.9168	0.9711	4.6124	0.1205	0.0900	0.5900	0.0128
15	WAMP+WL	0.9118	0.9681	4.6735	0.1181	0.2500	0.3900	0.0129

16	RMS+WAMP	0.9105	0.9729	4.7046	0.1184	0.1100	0.5600	0.0131
17	IEMG+MAV+RMS	0.8856	0.9772	5.2000	0.1112	0.2500	0.3300	0.0134
18	MAV+WL	0.8981	0.9761	4.9808	0.1111	0.1600	0.5000	0.0137
19	MAV+WAMP+WL	0.9161	0.9568	4.6171	0.1431	0.1900	0.4000	0.0141
20	IEMG+MAV	0.8796	0.9758	5.2595	0.1101	0.0600	0.5500	0.0148
21	IEMG+MAV+RMS+WL	0.9020	0.9658	4.8555	0.1218	0.2200	0.5400	0.0174
22	IEMG+MAV+RMS+WAMP+WL	0.9134	0.9642	4.6012	0.1246	0.2200	0.6100	0.0175
23	IEMG+MAV+WAMP+WL	0.9104	0.9638	4.6046	0.1249	0.3500	0.5200	0.0188
24	IEMG+WAMP+WL	0.9168	0.9657	4.6832	0.1231	0.5900	0.3700	0.0194
25	IEMG+WAMP	0.9034	0.9726	4.8223	0.1135	0.5200	0.4300	0.0195
26	IEMG+RMS	0.8851	0.9726	5.1959	0.1167	0.1100	0.7400	0.0209
27	IEMG+MAV+WAMP	0.9114	0.9748	4.6971	0.1229	0.2400	0.8500	0.0213
28	IEMG+RMS+WAMP	0.8928	0.9716	4.8437	0.1171	0.5100	0.4500	0.0220
29	MAV+RMS	0.8314	0.9759	5.8084	0.1138	0.7300	0.3700	0.0379
30	RMS	0.2477	0.9760	9.1197	0.1136	0.8500	0.1800	0.1793
31	MAV	0.2502	0.9746	9.0872	0.1163	0.8500	0.2600	0.1946

Table D.2

The comparison of the sEMG feature variations calculated over BF+MG+TA. Green shaded cells show the feature variations that provide strongly correlated position and moment predictions (i.e., r $\geq$ 0.90). BF: biceps femoris, MG: medial gastrocnemius, TA: tibialis anterior, IEMG: integrated EMG, MAV: mean absolute value, WAMP: Willison amplitude, RMS: root mean square; WL: waveform length.

Rank	sEMG Feature Variations	Pos Corr [r]	Mom Corr [r]	Pos RMSE [deg]	Mom RMSE [Nm/kg]	Pos SPM [%GC]	Mom SPM [%GC]	Overall Error Score
1	IEMG+WL	0.9199	0.9787	4.4577	0.1028	0.1400	0.2700	0.0080
2	WL	0.8889	0.9779	5.0233	0.1075	0.1100	0.2100	0.0089
3	RMS	0.8958	0.9773	5.0087	0.1119	0.0500	0.2900	0.0091
4	MAV	0.8938	0.9769	5.0418	0.1140	0.0200	0.3200	0.0094
5	RMS+WL	0.8930	0.9806	4.9612	0.1021	0.1400	0.2300	0.0094
6	IEMG+MAV	0.8876	0.9713	5.1315	0.1144	0.1300	0.2000	0.0101
7	WAMP+WL	0.9159	0.9732	4.5868	0.1160	0.2100	0.2700	0.0110
8	IEMG+MAV+WAMP	0.9166	0.9689	4.5150	0.1233	0.1200	0.3800	0.0121
9	IEMG	0.9086	0.9783	4.7683	0.1067	0.2700	0.2900	0.0128
10	IEMG+WAMP	0.9113	0.9712	4.6174	0.1193	0.2600	0.2600	0.0128
11	IEMG+MAV+WL	0.9075	0.9747	4.7171	0.1087	0.1900	0.3800	0.0136
12	MAV+RMS+WAMP	0.9122	0.9712	4.5584	0.1237	0.2200	0.3300	0.0136
13	IEMG+RMS+WL	0.8964	0.9695	4.8551	0.1086	0.4900	0.0400	0.0146
14	MAV+WAMP	0.9090	0.9779	4.6828	0.1093	0.3800	0.2800	0.0151
15	MAV+WAMP+WL	0.9114	0.9681	4.5964	0.1222	0.2100	0.4100	0.0158

16	IEMG+RMS+WAMP	0.9142	0.9569	4.5646	0.1314	0.1500	0.4300	0.0164
17	MAV+RMS+WL	0.8912	0.9784	5.0994	0.1056	0.1600	0.4600	0.0168
18	IEMG+MAV+RMS+WAMP+WL	0.9076	0.9658	4.5943	0.1214	0.2000	0.4300	0.0168
19	RMS+WAMP	0.9025	0.9738	4.8316	0.1167	0.3200	0.3300	0.0171
20	IEMG+MAV+RMS+WAMP	0.9132	0.9679	4.6074	0.1227	0.2600	0.4600	0.0182
21	IEMG+MAV+RMS	0.8818	0.9719	5.2026	0.1129	0.2000	0.3900	0.0187
22	MAV+WL	0.8940	0.9782	5.0412	0.1073	0.1600	0.5700	0.0194
23	IEMG+MAV+RMS+WL	0.9068	0.9675	4.7496	0.1170	0.3300	0.4100	0.0196
24	MAV+RMS+WAMP+WL	0.9043	0.9679	4.6777	0.1257	0.3700	0.4300	0.0222
25	IEMG+WAMP+WL	0.8882	0.9624	4.8793	0.1287	0.4100	0.2900	0.0234
26	WAMP	0.9066	0.9697	4.7485	0.1239	0.3500	0.5400	0.0239
27	RMS+WAMP+WL	0.8879	0.9682	4.9781	0.1219	0.6100	0.3000	0.0288
28	IEMG+RMS	0.8788	0.9746	5.2628	0.1146	0.3900	0.6800	0.0345
29	MAV+RMS	0.8497	0.9768	5.6081	0.1132	0.3900	0.5000	0.0349
30	IEMG+MAV+WAMP+WL	0.8806	0.9503	4.9230	0.1397	0.4500	0.4700	0.0365
31	IEMG+RMS+WAMP+WL	0.8913	0.9587	4.7921	0.1357	0.6000	0.5300	0.0387

Table D.3

The comparison of the sEMG feature variations calculated over BF+MG+TA+RF+GMax. Green shaded cells show the feature variations that provide strongly correlated position and moment predictions (i.e., r $\geq$ 0.90). BF: biceps femoris, MG: medial gastrocnemius, TA: tibialis anterior, RF: rectus femoris, GMax: gluteus maximus, IEMG: integrated EMG, MAV: mean absolute value, WAMP: Willison amplitude, RMS: root mean square; WL: waveform length.

Rank	sEMG Feature Variations	Pos Corr [r]	Mom Corr [r]	Pos RMSE [deg]	Mom RMSE [Nm/kg]	Pos SPM [%GC]	Mom SPM [%GC]	Overall Error Score
1	IEMG+WL	0.9160	0.9730	4.2670	0.1080	0.0200	0.3600	0.0062
2	IEMG	0.8920	0.9740	5.0670	0.1090	0.1700	0.1600	0.0071
3	MAV+WL	0.9010	0.9740	4.8690	0.1090	0.0500	0.3400	0.0077
4	IEMG+MAV+RMS	0.8870	0.9750	5.0960	0.1120	0.3000	0.0600	0.0081
5	RMS+WL	0.9010	0.9760	4.7560	0.1090	0.2400	0.2200	0.0089
6	WL	0.9050	0.9750	4.7940	0.1110	0.0900	0.4200	0.0096
7	IEMG+MAV+RMS+WL	0.9110	0.9740	4.7150	0.1090	0.2800	0.2800	0.0099
8	IEMG+RMS	0.8940	0.9740	4.9640	0.1110	0.1000	0.4500	0.0116
9	MAV+RMS	0.8720	0.9770	5.3510	0.1100	0.0800	0.4000	0.0122
10	IEMG+MAV+WL	0.8900	0.9710	4.9610	0.1110	0.4500	0.1700	0.0138
11	MAV+WAMP	0.8920	0.9610	4.6620	0.1360	0.2700	0.3200	0.0150
12	IEMG+RMS+WL	0.9030	0.9770	4.7590	0.1090	0.2600	0.5600	0.0153
13	IEMG+MAV	0.8860	0.9750	5.1390	0.1090	0.2900	0.4600	0.0170
14	MAV+RMS+WL	0.9020	0.9740	4.8610	0.1120	0.3000	0.5900	0.0175
15	RMS+WAMP+WL	0.8910	0.9540	4.6940	0.1330	0.2100	0.4900	0.0186

16	MAV+RMS+WAMP+WL	0.8980	0.9340	4.6200	0.1600	0.3100	0.3500	0.0209
17	WAMP	0.8940	0.9420	4.8420	0.1570	0.2300	0.4800	0.0220
18	MAV+WAMP+WL	0.8990	0.9400	4.6300	0.1500	0.2500	0.5400	0.0230
19	WAMP+WL	0.9030	0.9280	4.5960	0.1650	0.3200	0.4700	0.0254
20	IEMG+MAV+RMS+WAMP	0.9010	0.9130	4.5240	0.1850	0.2200	0.5000	0.0273
21	IEMG+RMS+WAMP+WL	0.8980	0.9290	4.4660	0.1800	0.3600	0.4600	0.0282
22	IEMG+MAV+WAMP+WL	0.8940	0.9480	4.6980	0.1480	0.3900	0.6000	0.0284
23	MAV+RMS+WAMP	0.9100	0.9280	4.6090	0.1730	0.5400	0.3700	0.0288
24	RMS+WAMP	0.8870	0.9430	5.1120	0.1460	0.5000	0.4100	0.0290
25	IEMG+WAMP	0.8940	0.9220	4.7000	0.1700	0.3100	0.5000	0.0292
26	IEMG+MAV+WAMP	0.9000	0.9250	4.6840	0.1770	0.3000	0.5700	0.0307
27	IEMG+MAV+RMS+WAMP+WL	0.8740	0.9370	4.8250	0.1610	0.4100	0.6200	0.0375
28	IEMG+WAMP+WL	0.8830	0.9180	4.8510	0.1730	0.4000	0.6300	0.0413
29	IEMG+RMS+WAMP	0.8980	0.9170	4.7240	0.1690	0.4600	0.8100	0.0461
30	MAV	0.8010	0.9760	6.2340	0.1130	0.7400	0.5900	0.0550
31	RMS	0.6910	0.9760	7.1440	0.1120	0.6000	0.5800	0.0789

REFERENCES

1. Ahmad, N., N. Thomas, P. Gill, and F. Torella, "The prevalence of major lower limb amputation in the diabetic and non-diabetic population of england 2003-2013," *Diabetes and Vascular Disease Research*, Vol. 13, no. 5, pp. 348–353, 2016. PMID: 27334482.

2. Imam, B., W. Miller, H. Finlayson, J. Finlayson, *et al.*, "Incidence of lower limb amputation in canada," *Canadian Journal of Public Health*, Vol. 108, p. 374, 11 2017.

3. Huang, S., and D. P. Ferris, "Muscle activation patterns during walking from transtibial amputees recorded within the residual limb-prosthetic interface," *Journal of NeuroEngineering and Rehabilitation*, Vol. 9, pp. 55 – 55, 2012.

4. Isaacs-Itua, A., and I. Sedki, "Management of lower limb amputations," *British Journal of Hospital Medicine*, Vol. 79, pp. 205–210, 04 2018.

5. Hafner, B., J. Sanders, J. Czerniecki, and J. Fergason, "Transtibial energy-storage-and-return prosthetic devices: A review of energy concepts and a proposed nomenclature," *Journal of Rehabilitation Research and Development*, Vol. 39, pp. 1–11, 01 2002.

6. Hansen, A., D. Childress, C. Miff, S. Gard, *et al.*, "The human ankle during walking: Implications for design of biomimetic ankle prostheses," *Journal of Biomechanics*, Vol. 37, pp. 1467–74, 11 2004.

7. Bergelin, B., "Design of a transtibial prosthesis utilizing active and passive components in conjunction with a four-bar mechanism," Master's thesis, Marquette University, Milwaukee, 2010.

8. Tucker, M., J. Olivier, A. Pagel, H. Bleuler, *et al.*, "Control strategies for active lower extremity prosthetics and orthotics: A review," *Journal of NeuroEngineering and Rehabilitation*, Vol. 12, p. 1, 01 2015.

9. Au, S., P. Bonato, and H. Herr, "An emg-position controlled system for an active ankle-foot prosthesis: an initial experimental study," in *9th International Conference on Rehabilitation Robotics, 2005. ICORR 2005.*, pp. 375–379, 2005.

10. Au, S., M. Berniker, and H. Herr, "Powered ankle-foot prosthesis to assist level-ground and stair-descent gaits," *Neural Networks*, Vol. 21, no. 4, pp. 654–666, 2008. Robotics and Neuroscience.

11. Herr, H., and A. Grabowski, "Bionic ankle-foot prosthesis normalizes walking gait for persons with leg amputation," *Proceedings of the Royal Society B: Biological Sciences*, Vol. 279, pp. 457–64, 07 2011.

12. Eilenberg, M., H. Geyer, and H. Herr, "Control of a powered ankle-foot prosthesis based on a neuromuscular model," *IEEE Transactions on Neural Systems and Rehabilitation Engineering*, Vol. 18, pp. 164–73, 04 2010.

13. Tahir, U., A. Hessel, E. Lockwood, J. Tester, *et al.*, "Case study: A bio-inspired control algorithm for a robotic foot-ankle prosthesis provides adaptive control of level walking and stair ascent," *Frontiers in Robotics and AI*, Vol. 5, 04 2018.

14. Huong, V., D. Dong, H.-L. Cao, T. Verstraten, *et al.*, "A review of gait phase detection algorithms for lower limb prostheses," *Sensors*, Vol. 20, p. 3972, 07 2020.

15. Ferris, A., J. Aldridge, C. Rabago, and J. Wilken, "Evaluation of a powered ankle-foot prosthetic system during walking," *Archives of Physical Medicine and Rehabilitation*, Vol. 93, 06 2012.

16. Bovi, G., M. Rabuffetti, P. Mazzoleni, and M. Ferrarin, "A multiple-task gait analysis approach: Kinematic, kinetic and emg reference data for healthy young and adult subjects," *Gait and Posture*, Vol. 33, no. 1, pp. 6–13, 2011.

17. Inman, V. T., H. J. Ralston, and F. Todd, *Human Walking*, Baltimore: Williams and Wilkins., 1981.

18. Palastanga, N., and R. Soames, *Anatomy and Human Movement, Structure and Function*, Elsevier Health Sciences, 2011.

19. Winter, D. A., and S. E. Sienko, "Biomechanics of below-knee amputee gait," *Journal of Biomechanics*, Vol. 21, no. 5, pp. 361–367, 1988.

20. Winter, D. A., *Biomechanics and motor control of human gait: normal, elderly and pathological*, Waterloo Biomechanics, 1991.

21. Quinlivan, B., S. Lee, P. Malcolm, D. Rossi, *et al.*, "Assistance magnitude versus metabolic cost reductions for a tethered multiarticular soft exosuit," *Science Robotics*, Vol. 2, p. eaah4416, 01 2017.

22. Brockett, C., and G. Chapman, "Biomechanics of the ankle," *Orthopaedics and Trauma*, Vol. 30, 04 2016.

23. Klodd, E., A. Hansen, S. Fatone, and M. Edwards, "Effects of prosthetic foot forefoot flexibility on gait of unilateral transtibial prosthesis users," *Journal of Rehabilitation Research and Development*, Vol. 47, no. 9, pp. 899–910, 2010.

24. Athavale, Y., and S. Krishnan, "Biosignal monitoring using wearables: Observations and opportunities," *Biomedical Signal Processing and Control*, Vol. 38, pp. 22–33, 09 2017.

25. Raez, M., M. Hussain, and F. Mohd-Yasin, "Techniques of emg signal analysis: Detection, processing, classification and applications," *Biological Procedures Online*, Vol. 8, pp. 11–35, 02 2006.

26. Kuo, I., and B. Ehrlich, "Signaling in muscle contraction," *Cold Spring Harbor Perspectives in Biology*, Vol. 7, p. a006023, 02 2015.

27. Rodriguez-Carreno, I., L. Gila-Useros, and A. Malanda-Trigueros, "Motor unit action potential duration: Measurement and significance," in *Advances in Clinical Neurophysiology*, ch. 7, Rijeka: IntechOpen, 2012.

28. Zheng, M., M. Crouch, and M. Eggleston, "Surface electromyography as a natural human-machine interface: A review," *IEEE Sensors Journal*, 01 2021.

29. Delis, A., J. Carvalho, A. Rocha, R. Ferreira, *et al.*, "Estimation of the knee joint angle from surface electromyographic signals for active control of leg prostheses," *Physiological Measurement*, Vol. 30, pp. 931–46, 09 2009.

30. Farmer, S., B. Silver-Thorn, P. Voglewede, and S. Beardsley, "Within-socket myoelectric prediction of continuous ankle kinematics for control of a powered transtibial prosthesis," *Journal of Neural Engineering*, Vol. 11, p. 056027, 09 2014.

31. Zabre, E., L. Riem, P. Voglewede, B. Silver-Thorn, *et al.*, "Continuous myoelectric prediction of future ankle angle and moment across ambulation conditions and their transitions," *Frontiers in Neuroscience*, Vol. 15, 08 2021.

32. Eslamy, M., and A. F. Schilling, "Estimation of knee and ankle angles during walking using thigh and shank angles," *Bioinspiration and Biomimetics*, Vol. 16, no. 6, p. 066012, 2021.

33. Eslamy, M., and M. Rastgaar, "Multi-joint leg moment estimation during walking using thigh or shank angles," *IEEE Transactions on Neural Systems and Rehabilitation Engineering*, 2022.

34. Ranavolo, A., M. Serrao, and F. Draicchio, "Critical issues and imminent challenges in the use of semg in return-to-work rehabilitation of patients affected by neurological disorders in the epoch of human–robot collaborative technologies," *Frontiers in Neurology*, Vol. 11, p. 572069, 2020.

35. Halaki, M., and K. Ginn, "Normalization of emg signals: To normalize or not to normalize and what to normalize to?," *Computational Intelligence in Electromyography Analysis*, pp. 175–194, 10 2012.

36. Jain, R., and V. K. Garg, "Emg signal feature extraction, normalization and classification for pain and normal muscles using genetic algorithm and support vector machine.," *Revue d'Intelligence Artificielle*, Vol. 34, no. 5, 2020.

37. Burden, A., "How should we normalize electromyograms obtained from healthy participants? what we have learned from over 25 years of research," *Journal of Electromyography and Kinesiology*, Vol. 20, no. 6, pp. 1023–1035, 2010.

38. Tanaka, T., I. Nambu, Y. Maruyama, and Y. Wada, "Sliding-window normalization to improve the performance of machine-learning models for real-time motion prediction using electromyography," *Sensors*, Vol. 22, no. 13, 2022.

39. Ameri, A., M. Akhaee, E. Scheme, and K. Englehart, "A deep transfer learning approach to reducing the effect of electrode shift in emg pattern recognition-based control," *IEEE Transactions on Neural Systems and Rehabilitation Engineering*, Vol. PP, pp. 1–1, 12 2019.

40. Khushaba, R. N., M. Takruri, J. V. Miro, and S. Kodagoda, "Towards limb position invariant myoelectric pattern recognition using time-dependent spectral features," *Neural Networks*, Vol. 55, pp. 42–58, 2014.

41. Scheme, E., and K. Englehart, "Electromyogram pattern recognition for control of powered upper-limb prostheses: State of the art and challenges for clinical use," *Journal of Rehabilitation Research and Development*, Vol. 48, pp. 643–59, 07 2011.

42. Triwiyanto, T., O. Wahyunggoro, H. A. Nugroho, and H. Herianto, "Muscle fatigue compensation of the electromyography signal for elbow joint angle estimation using adaptive feature," *Computers and Electrical Engineering*, Vol. 71, pp. 284–293, 10 2018.

43. Orosco, E. C., N. M. Lopez, and F. di Sciascio, "Bispectrum-based features classification for myoelectric control," *Biomedical Signal Processing and Control*, Vol. 8, no. 2, pp. 153–168, 2013.

44. Phinyomark, A., P. Phukpattaranont, and C. Limsakul, "Feature reduction and selection for emg signal classification," *Expert Systems with Applications*, Vol. 39, no. 8, pp. 7420–7431, 2012.

45. Restrepo-Agudelo, S., S. Roldan-Vasco, L. Ramirez-Arbelaez, S. Cadavid-Arboleda, *et al.*, "Improving surface emg burst detection in infrahyoid muscles during swallowing using digital filters and discrete wavelet analysis," *Journal of Electromyography and Kinesiology*, Vol. 35, pp. 1–8, 2017.

46. Cop, C. P., G. Durandau, A. M. Esteban, R. C. van't Veld, *et al.*, "Model-based estimation of ankle joint stiffness during dynamic tasks: A validation-based approach," in *2019 Annual International Conference of the IEEE Engineering in Medicine and Biology Society (EMBC)*, pp. 4104–4107, IEEE, 2019.

47. Durandau, G., W. F. Rampeltshammer, H. v. d. Kooij, and M. Sartori, "Neuromechanical model-based adaptive control of bilateral ankle exoskeletons: Biological joint torque and electromyogram reduction across walking conditions," *IEEE Transactions on Robotics*, Vol. 38, no. 3, pp. 1380–1394, 2022.

48. Zhang, F., P. Li, Z.-G. Hou, Z. Lu, *et al.*, "Semg-based continuous estimation of joint angles of human legs by using bp neural network," *Neurocomputing*, Vol. 78, no. 1, pp. 139–148, 2012.

49. Chen, J., X. Zhang, Y. Cheng, and N. Xi, "Surface emg based continuous estimation of human lower limb joint angles by using deep belief networks," *Biomedical Signal Processing and Control*, Vol. 40, pp. 335–342, 2018.

50. Siu, H. C., J. Sloboda, R. J. McKindles, and L. A. Stirling, "Ankle torque estimation during locomotion from surface electromyography and accelerometry," in *2020 8th IEEE RAS/EMBS International Conference for Biomedical Robotics and Biomechatronics (BioRob)*, pp. 80–87, 2020.

51. Jephil, P. B., P. Acharaya, L. Xu, K. Guo, *et al.*, "Estimation of ankle joint torque and angle based on s-emg signal for assistive rehabilitation robots," *Biomedical Signal Processing*, pp. 31–47, 01 2020.

52. Truong, M. T. N., A. E. A. Ali, D. Owaki, and M. Hayashibe, "Emg-based estimation of lower limb joint angles and moments using long short-term memory network," *Sensors*, Vol. 23, no. 6, 2023.

53. Lu, Y., H. Wang, B. Zhou, C. Wei, *et al.*, "Continuous and simultaneous estimation of lower limb multi-joint angles from semg signals based on stacked convolutional and lstm models," *Expert Systems with Applications*, Vol. 203, p. 117340, 2022.

54. Zhang, L., D. Soselia, R. Wang, and E. M. Gutierrez-Farewik, "Lower-limb joint torque prediction using lstm neural networks and transfer learning," *IEEE Transactions on Neural Systems and Rehabilitation Engineering*, Vol. 30, pp. 600–609, 2022.

55. Peng, L., Z.-G. Hou, L. Peng, and W.-Q. Wang, "A practical emg-driven musculoskeletal model for dynamic torque estimation of knee joint," in *2015 IEEE International Conference on Robotics and Biomimetics (ROBIO)*, pp. 1036–1040, 2015.

56. Zou, J., Y. Han, and S.-S. So, "Overview of artificial neural networks," *Artificial Neural Networks: Methods and Applications*, pp. 14–22, 2009.

57. Sepulveda, F., D. M. Wells, and C. L. Vaughan, "A neural network representation of electromyography and joint dynamics in human gait," *Journal of Biomechanics*, Vol. 26, no. 2, pp. 101–109, 1993.

58. Krenker, A., J. Bester, and A. Kos, "Introduction to the artificial neural networks," *Artificial Neural Networks-Methodological Advances and Biomedical Applications*, 04 2011.

59. Luh, J.-J., G.-C. Chang, C.-K. Cheng, J.-S. Lai, *et al.*, "Isokinetic elbow joint torques estimation from surface emg and joint kinematic data: using an artificial neural network model," *Journal of Electromyography and Kinesiology*, Vol. 9, no. 3, pp. 173–183, 1999.

60. Souza, J., N. Fey, J. Cheesborough, S. Agnew, *et al.*, "Advances in transfemoral amputee rehabilitation: Early experience with targeted muscle reinnervation," *Current Surgery Reports*, Vol. 2, pp. 1–9, 05 2014.

61. Kaiser, M., "Time-delay neural networks for control," *IFAC Proceedings Volumes*, Vol. 27, no. 14, pp. 967–972, 1994.

62. Liu, W., L. Zhu, F. Feng, W. Zhang, *et al.*, "A time delay neural network based technique for nonlinear microwave device modeling," *Micromachines*, Vol. 11, p. 831, 08 2020.

63. Hochreiter, S., and J. Schmidhuber, "Long short-term memory," *Neural Computation*, Vol. 9, no. 8, pp. 1735–1780, 1997.

64. Yu, Y., X. Si, C. Hu, and J. Zhang, "A review of recurrent neural networks: Lstm cells and network architectures," *Neural Computation*, Vol. 31, no. 7, pp. 1235–1270, 2019.

65. Cheng, H.-R., G.-Z. Cao, C.-H. Li, A. Zhu, *et al.*, "A cnn-lstm hybrid model for ankle joint motion recognition method based on semg," *2020 International Conference on Ubiquitous Robots (UR)*, pp. 339–344, 2020.

66. Lawson, B. E., J. Mitchell, D. Truex, A. Shultz, *et al.*, "A robotic leg prosthesis: Design, control, and implementation," *IEEE Robotics and Automation Magazine*, Vol. 21, no. 4, pp. 70–81, 2014.

67. Gates, D., J. Lelas, U. Croce, H. Herr, *et al.*, "Characterization of ankle function during stair ambulation," *The 26th Annual International Conference of the IEEE Engineering in Medicine and Biology Society*, Vol. 2, pp. 4248–4251, 2004.

68. Culver, S., H. Bartlett, A. Shultz, and M. Goldfarb, "A stair ascent and descent controller for a powered ankle prosthesis," *IEEE Transactions on Neural Systems and Rehabilitation Engineering*, Vol. 26, no. 5, pp. 993–1002, 2018.

69. Hargrove, L. J., A. J. Young, A. M. Simon, N. P. Fey, *et al.*, "Intuitive Control of a Powered Prosthetic Leg During Ambulation: A Randomized Clinical Trial," *JAMA*, Vol. 313, pp. 2244–2252, 06 2015.

70. Spanias, J., A. Simon, S. Finucane, E. Perreault, *et al.*, "Online adaptive neural control of a robotic lower limb prosthesis," *Journal of Neural Engineering*, Vol. 15, 10 2018.

71. Hoozemans, M. J., and J. H. van Dieen, "Prediction of handgrip forces using surface emg of forearm muscles," *Journal of Electromyography and Kinesiology*, Vol. 15, no. 4, pp. 358–366, 2005.

72. Al-Quraishi, M. S., A. J. Ishak, S. A. Ahmad, and M. K. Hasan, "Impact of feature extraction techniques on classification accuracy for emg based ankle joint movements," in *2015 10th Asian Control Conference (ASCC)*, pp. 1–5, 2015.

73. Cavallaro, E., J. Rosen, J. C. Perry, and S. Burns, "Real-time myoprocessors for a neural controlled powered exoskeleton arm," *IEEE Transactions on Biomedical Engineering*, Vol. 53, pp. 2387–2396, 2006.

74. Fleischer, C., and G. Hommel, "A human–exoskeleton interface utilizing electromyography," *IEEE Transactions on Robotics*, Vol. 24, no. 4, pp. 872–882, 2008.

75. Spanias, J. A., A. M. Simon, K. A. Ingraham, and L. J. Hargrove, "Effect of additional mechanical sensor data on an emg-based pattern recognition system for a powered leg prosthesis," *2015 7th International IEEE/EMBS Conference on Neural Engineering (NER)*, pp. 639–642, 2015.

76. Naidu, D., C.-H. Chen, A. Perez, and M. P. Schoen, "Control strategies for smart prosthetic hand technology: An overview," in *2008 30th Annual International Conference of the IEEE Engineering in Medicine and Biology Society*, pp. 4314–4317, 2008.

77. De Luca, C. J., L. Donald Gilmore, M. Kuznetsov, and S. H. Roy, "Filtering the surface emg signal: Movement artifact and baseline noise contamination," *Journal of Biomechanics*, Vol. 43, no. 8, pp. 1573–1579, 2010.

78. Zhang, Z., J. Jiang, L. Peng, and H. Fan, "A method to control ankle exoskeleton with surface electromyography signals," in *Lecture Notes in Computer Science*, Vol. 13, pp. 390–397, 11 2010.

79. Sup, F., H. A. Varol, J. Mitchell, T. Withrow, *et al.*, "Design and control of an active electrical knee and ankle prosthesis," in *2008 2nd IEEE RAS and EMBS International Conference on Biomedical Robotics and Biomechatronics*, pp. 523–528, 2008.

80. Hermens, H. J., B. Freriks, C. Disselhorst-Klug, and G. Rau, "Development of recommendations for semg sensors and sensor placement procedures," *Journal of Electromyography and Kinesiology*, Vol. 10, no. 5, pp. 361–374, 2000.

81. Lencioni, T., I. Carpinella, M. Rabuffetti, A. Marzegan, *et al.*, "Human kinematic, kinetic and emg data during different walking and stair ascending and descending tasks," *Scientific Data*, Vol. 6, p. 309, 12 2019.

82. Liu, J., S. H. Kang, D. Xu, Y. Ren, *et al.*, "Emg-based continuous and simultaneous estimation of arm kinematics in able-bodied individuals and stroke survivors," *Frontiers in Neuroscience*, Vol. 11, 08 2017.

83. Rahmatian, S., M. J. Mahjoob, and M. R. Hanachi, "Continuous estimation of ankle joint angular position based on the myoelectric signals," in *2016 Artificial Intelligence and Robotics (IRANOPEN)*, pp. 158–163, 2016.

84. Pulliam, C., J. Lambrecht, and R. Kirsch, "Electromyogram-based neural network control of transhumeral prostheses," *Journal of Rehabilitation Research and Development*, Vol. 48, pp. 739–54, 07 2011.

85. Siu, W.-C., L.-P. Chau, L. Wang, and T. Tan, *Learning Approaches in Signal Processing*, Pan Stanford Publishing Pte Ltd, 2018.

86. MacKay, D. J. C., "A practical bayesian framework for backprop networks," *Neural Computation*, 1992.

87. Pataky, T. C., "Generalized n-dimensional biomechanical field analysis using statistical parametric mapping," *Journal of Biomechanics*, Vol. 43, no. 10, pp. 1976–1982, 2010.

88. Kiguchi, K., and Y. Hayashi, "An emg-based control for an upper-limb power-assist exoskeleton robot," *IEEE Transactions on Systems, Man, and Cybernetics, Part B (Cybernetics)*, Vol. 42, no. 4, pp. 1064–1071, 2012.

89. Hahn, M., and K. O'Keefe, "A neural network model for estimation of net joint moments during normal gait," *Journal of Musculoskeletal Research*, Vol. 11, 09 2008.

90. Huang, H., F. Zhang, L. Hargrove, Z. Dou, *et al.*, "Continuous locomotion-mode identification for prosthetic legs based on neuromuscular-mechanical fusion," *Biomedical Engineering*, Vol. 58, pp. 2867 – 2875, 11 2011.

91. Lee, S., M.-O. Kim, T. Kang, J. Park, *et al.*, "Knit band sensor for myoelectric control of surface emg-based prosthetic hand," *IEEE Sensors*, Vol. 18, no. 20, pp. 8578–8586, 2018.

92. Ison, M., I. Vujaklija, B. Whitsell, D. Farina, *et al.*, "High-density electromyography and motor skill learning for robust long-term control of a 7-dof robot arm," *IEEE Transactions on Neural Systems and Rehabilitation Engineering*, Vol. 24, no. 4, pp. 424–433, 2016.

93. Rojas-Martinez, M., M. A. Mananas, and J. Alonso, "High-density surface emg maps from upper-arm and forearm muscles," *Journal of Neuroengineering and Rehabilitation*, Vol. 9, p. 85, 12 2012.

94. Zwarts, M. J., and D. F. Stegeman, "Multichannel surface emg: Basic aspects and clinical utility," *Muscle and Nerve*, Vol. 28, pp. 1 – 17, 07 2003.

95. Clites, T. R., M. J. Carty, J. B. Ullauri, M. E. Carney, *et al.*, "Proprioception from a neurally controlled lower-extremity prosthesis," *Science Translational Medicine*, Vol. 10, no. 443, p. eaap8373, 2018.

96. Srinivasan, S., M. Diaz, M. Carty, and H. Herr, "Towards functional restoration for persons with limb amputation: A dual-stage implementation of regenerative agonist-antagonist myoneural interfaces," *Scientific Reports*, Vol. 9, 02 2019.

97. Herr, H., and A. Grabowski, "Bionic ankle-foot prosthesis normalizes walking gait for persons with leg amputation," *Proceedings of the Royal Society B: Biological Sciences*, Vol. 279, pp. 457–64, 07 2011.

98. Ingraham, K., H. Choi, E. Gardinier, C. Remy, *et al.*, "Choosing appropriate prosthetic ankle work to reduce the metabolic cost of individuals with transtibial amputation," *Scientific Reports*, Vol. 8, 10 2018.

99. Wilken, J. M., E. H. Sinitski, and E. A. Bagg, "The role of lower extremity joint powers in successful stair ambulation," *Gait and Posture*, Vol. 34, no. 1, pp. 142–144, 2011.

100. Montgomery, J., and A. Grabowski, "Individual leg and joint work during sloped walking for people with a transtibial amputation using passive and powered prostheses," *Frontiers in Robotics and AI*, Vol. 4, 12 2017.

101. Montgomery, J., and A. Grabowski, "The contributions of ankle, knee and hip joint work to individual leg work change during uphill and downhill walking over a range of speeds," *Royal Society Open Science*, Vol. 5, p. 180550, 08 2018.

102. Montgomery, J., and A. Grabowski, "Use of a powered ankle-foot prosthesis reduces the metabolic cost of uphill walking and improves leg work symmetry in people with transtibial amputations," *Journal of The Royal Society Interface*, Vol. 15, p. 20180442, 08 2018.

103. Hudgins, B., P. Parker, and R. Scott, "A new strategy for multifunction myoelectric control," *IEEE Transactions on Biomedical Engineering*, Vol. 40, no. 1, pp. 82–94, 1993.

104. Brackx, B., M. V. Damme, A. Matthys, B. Vanderborght, *et al.*, "Passive ankle-foot prosthesis prototype with extended push-off," *International Journal of Advanced Robotic Systems*, Vol. 10, no. 2, p. 101, 2013.

105. Gehlhar, R., Y. Chen, and A. D. Ames, "Data-driven characterization of human interaction for model-based control of powered prostheses," in *2020 IEEE/RSJ International Conference on Intelligent Robots and Systems (IROS)*, pp. 4126–4133, 2020.

106. Vucina, A., "Kinematics and forces in the above-knee prosthesis during the stair climbing," *International Journal of Simulation Modelling*, Vol. 4, pp. 17–26, 03 2005.

107. Nasr, A., B. Laschowski, and J. McPhee, "Myoelectric Control of Robotic Leg Prostheses and Exoskeletons: A Review," *International Design Engineering Technical Conferences and Computers and Information in Engineering Conference*, Vol. 8, 08 2021.

108. Shultz, A., and M. Goldfarb, "A unified controller for walking on even and uneven terrain with a powered ankle prosthesis," *IEEE Transactions on Neural Systems and Rehabilitation Engineering*, Vol. PP, pp. 1–1, 02 2018.

109. Attal, F., Y. Amirat, A. Chibani, and S. Mohammed, "Automatic recognition of gait phases using a multiple-regression hidden markov model," *IEEE/ASME Transactions on Mechatronics*, Vol. 23, no. 4, pp. 1597–1607, 2018.

110. Liu, H., Q. Huang, and Z. Tong, "Simulation and analysis of a full-active electrohydrostatic powered ankle prosthesis," in *2019 19th International Conference on Advanced Robotics (ICAR)*, pp. 81–86, 2019.

111. Lenzi, T., M. Cempini, L. J. Hargrove, and T. A. Kuiken, "Design, development, and validation of a lightweight nonbackdrivable robotic ankle prosthesis," *IEEE/ASME Transactions on Mechatronics*, Vol. 24, no. 2, pp. 471–482, 2019.

112. Quintero, D., D. J. Villarreal, D. J. Lambert, S. Kapp, *et al.*, "Continuous-phase control of a powered knee-ankle prosthesis: Amputee experiments across speeds and inclines," *IEEE Transactions on Robotics*, Vol. 34, no. 3, pp. 686–701, 2018.

113. Khademi, G., and D. Simon, "Toward minimal-sensing locomotion mode recognition for a powered knee-ankle prosthesis," *IEEE Transactions on Biomedical Engineering*, Vol. 68, no. 3, pp. 967–979, 2021.

114. Zhang, K., *Sensor fusion for predictive control of human-prosthesis-environment dynamics in assistive walking.* PhD thesis, University of British Columbia, 2022.

115. Ferris, D., and B. Schlink, "Robotic devices to enhance human movement performance," *Kinesiology Review*, Vol. 6, pp. 70–77, 02 2017.

116. Hosseini, M., R. Meattini, A. San-Millan, G. Palli, *et al.*, "A semg-driven soft exosuit based on twisted string actuators for elbow assistive applications," *IEEE Robotics and Automation Letters*, Vol. PP, 04 2020.

117. Huang, S., J. P. Wensman, and D. P. Ferris, "Locomotor adaptation by transtibial amputees walking with an experimental powered prosthesis under continuous myoelectric control," *IEEE Transactions on Neural Systems and Rehabilitation Engineering*, Vol. 24, no. 5, pp. 573–581, 2016.

118. Hunt, G. R., S. Hood, and T. Lenzi, "Stand-up, squat, lunge, and walk with a robotic knee and ankle prosthesis under shared neural control," *IEEE Open Journal of Engineering in Medicine and Biology*, Vol. 2, pp. 267–277, 2021.

119. Kyeong, S., J. Feng, J. K. Ryu, J.-J. Park, *et al.*, "Surface electromyography characteristics for motion intention recognition and implementation issues in lower-limb exoskeletons," *International Journal of Control, Automation and Systems*, Vol. 20, pp. 1018–1028, 2022.

120. Li, Z., Y. Yuan, L. Luo, W. Su, *et al.*, "Hybrid brain/muscle signals powered wearable walking exoskeleton enhancing motor ability in climbing stairs activity," *IEEE Transactions on Medical Robotics and Bionics*, Vol. 1, no. 4, pp. 218–227, 2019.

121. Yin, G., X. Zhang, D. Chen, H. Li, *et al.*, "Processing surface emg signals for exoskeleton motion control," *Frontiers in Neurorobotics*, Vol. 14, 07 2020.

122. Zhang, Q., K. Lambeth, Z. Sun, A. Dodson, *et al.*, "Evaluation of a fused sonomyography and electromyography-based control on a cable-driven ankle exoskeleton," *IEEE Transactions on Robotics*, pp. 1–20, 2023.

123. Huang, H., T. Kuiken, and R. Lipschutz, "A strategy for identifying locomotion modes using surface electromyography," *IEEE Transactions on Bio-medical Engineering*, Vol. 56, pp. 65–73, 02 2009.

124. Liu, M., F. Zhang, and H. Huang, "An adaptive classification strategy for reliable locomotion mode recognition," *Sensors*, Vol. 17, 09 2017.

125. Miller, J. D., M. S. Beazer, and M. E. Hahn, "Myoelectric walking mode classification for transtibial amputees," *IEEE Transactions on Biomedical Engineering*, Vol. 60, no. 10, pp. 2745–2750, 2013.

126. Varol, H. A., F. Sup, and M. Goldfarb, "Multiclass real-time intent recognition of a powered lower limb prosthesis," *IEEE Transactions on Biomedical Engineering*, Vol. 57, no. 3, pp. 542–551, 2010.

127. Asif, M., M. I. Tiwana, U. S. Khan, W. S. Qureshi, *et al.*, "Advancements, trends and future prospects of lower limb prosthesis," *IEEE Access*, Vol. 9, pp. 85956–85977, 2021.

128. Fleming, A., N. Stafford, S. Huang, X. Hu, *et al.*, "Myoelectric control of robotic lower limb prostheses: A review of electromyography interfaces, control paradigms, challenges and future directions," *Journal of Neural Engineering*, Vol. 18, 07 2021.

129. Chowdhury, R., M. Reaz, M. A. B. M. Ali, K. Chellappan, *et al.*, "Surface electromyography signal processing and classification techniques," *Sensors*, Vol. 13, no. 9, pp. 12431–12466, 2013.

130. Chambers, A., J. Haney, T. Huppert, and M. Redfern, "The effect of prolonged walking with intermittent standing on erector spinae and soleus muscle oxygenation and discomfort," *Journal of Sports Science and Medicine*, Vol. 18, pp. 337–343, 06 2019.

131. Schlink, B., A. Nordin, C. Brooks, and D. Ferris, "Fatigue induces altered spatial myoelectric activation patterns in the medial gastrocnemius during locomotion," *Journal of Neurophysiology*, Vol. 125, 04 2021.

132. den Otter, A., A. Geurts, T. Mulder, and J. Duysens, "Speed related changes in muscle activity from normal to very slow walking speeds," *Gait and Posture*, Vol. 19, no. 3, pp. 270–278, 2004.

133. Ma, X., Y. Liu, Q. Song, and C. Wang, "Continuous estimation of knee joint angle based on surface electromyography using a long short-term memory neural network and time-advanced feature," *Sensors*, Vol. 20, 09 2020.

134. Foroutannia, A., M.-R. Akbarzadeh-T, and A. Akbarzadeh, "A deep learning strategy for emg-based joint position prediction in hip exoskeleton assistive robots," *Biomedical Signal Processing and Control*, Vol. 75, p. 103557, 2022.

135. Hussain, T., N. Iqbal, F. Maqbool, M. Khan, *et al.*, "Intent based recognition of walking and ramp activities for amputee using semg based lower limb prostheses," *Biocybernetics and Biomedical Engineering*, Vol. 40, 06 2020.

136. Du, L., F. Zhang, H. He, and H. Huang, "Improving the performance of a neural-machine interface for prosthetic legs using adaptive pattern classifiers," *Annual International Conference of the IEEE Engineering in Medicine and Biology Society*, Vol. 2013, pp. 1571–1574, 07 2013.

137. Hargrove, L., A. Simon, A. Young, R. Lipschutz, *et al.*, "Robotic leg control with emg decoding in an amputee with nerve transfers," *The New England Journal of Medicine*, Vol. 369, pp. 1237–42, 09 2013.

138. Spanias, J. A., E. J. Perreault, and L. J. Hargrove, "Detection of and compensation for emg disturbances for powered lower limb prosthesis control," *IEEE Transactions on Neural Systems and Rehabilitation Engineering*, Vol. 24, no. 2, pp. 226–234, 2016.

139. Young, A., T. Kuiken, and L. Hargrove, "Analysis of using emg and mechanical sensors to enhance intent recognition in powered lower limb prostheses," *Journal of Neural Engineering*, Vol. 11, p. 056021, 09 2014.

140. Hoover, C., G. Fulk, and K. Fite, "The design and initial experimental validation of an active myoelectric transfemoral prosthesis," *Journal of Medical Devices*, Vol. 6, p. 011005, 03 2012.

141. Mohammed Zaffir, M. A., P. Gunaratne, D. Arase, K. Sakurai, *et al.*, "Comparison of deep neural network models and effectiveness of emg signal feature value for estimating dorsiflexion," *Electronics*, Vol. 10, p. 2767, 11 2021.

142. Isakov, E., H. Burger, M. Gregoric, and C. Marincek, "Stump length as related to atrophy and strength of the thigh muscles in trans-tibial amputees," *Prosthetics and Orthotics International*, Vol. 20, pp. 96–100, 09 1996.

143. Ranz, E. C., J. M. Wilken, D. A. Gajewski, and R. R. Neptune, "The influence of limb alignment and transfemoral amputation technique on muscle capacity during gait," *Computer Methods in Biomechanics and Biomedical Engineering*, Vol. 20, no. 11, pp. 1167–1174, 2017. PMID: 28650686.

144. Tintle, S., J. Keeling, S. Shawen, J. Forsberg, *et al.*, "Traumatic and trauma-related amputations part i general principles and lower-extremity amputations," *The Journal of Bone and Joint Surgery*, Vol. 92, pp. 2852–68, 12 2010.

145. Keles, A. D., and C. A. Yucesoy, "Development of a neural network based control algorithm for powered ankle prosthesis," *Journal of Biomechanics*, Vol. 113, p. 110087, 2020.

146. Kaushik, S., A. Choudhury, P. Kumar, N. Dasgupta, *et al.*, "Ai in healthcare: Time-series forecasting using statistical, neural, and ensemble architectures," *Frontiers in Big Data*, 01 2020.

147. Yi, C., F. Jiang, S. Zhang, H. Guo, *et al.*, "Continuous prediction of lower-limb kinematics from multi-modal biomedical signals," *IEEE Transactions on Circuits and Systems for Video Technology*, Vol. 32, no. 5, pp. 2592–2602, 2022.

148. Song, J., A. Zhu, Y. Tu, H. Huang, *et al.*, "Effects of different feature parameters of semg on human motion pattern recognition using multilayer perceptrons and lstm neural networks," *Applied Sciences*, Vol. 10, p. 3358, 05 2020.

149. Cipolla, R., Y. Gal, and A. Kendall, "Multi-task learning using uncertainty to weigh losses for scene geometry and semantics," in *2018 IEEE/CVF Conference on Computer Vision and Pattern Recognition*, pp. 7482–7491, 2018.

150. Rebuffi, S.-A., H. Bilen, and A. Vedaldi, "Learning multiple visual domains with residual adapters," in *Advances in Neural Information Processing Systems*, Vol. 30, Curran Associates, Inc., 2017.

151. Zhang, Y., and Q. Yang, "A survey on multi-task learning," *IEEE Transactions on Knowledge and Data Engineering*, Vol. PP, 07 2021.

152. Phinyomark, A., C. Limsakul, and P. Phukpattaranont, "A novel feature extraction for robust emg pattern recognition," *Journal of Computing*, Vol. 1, pp. 71–80, 12 2009.

153. Phinyomark, A., S. Hirunviriya, A. Nuidod, P. Phukpattaranont, *et al.*, "Evaluation of emg feature extraction for movement control of upper limb prostheses based on class separation index," *IFMBE Proceedings*, Vol. 35, 06 2011.

154. Kingma, D., and J. Ba, "Adam: A method for stochastic optimization," *International Conference on Learning Representations*, 12 2014.

155. Zhang, X., and M. Ma, "Research on semg feature generation and classification performance based on ebgan," *Electronics*, Vol. 12, p. 1040, 02 2023.

156. Bao, T., S. A. R. Zaidi, S. Xie, P. Yang, *et al.*, "A cnn-lstm hybrid model for wrist kinematics estimation using surface electromyography," *IEEE Transactions on Instrumentation and Measurement*, Vol. 70, pp. 1–9, 2021.

157. Kim, D., K. Koh, G. Oppizzi, R. Baghi, *et al.*, "Simultaneous estimations of joint angle and torque in interactions with environments using emg," in *2020 IEEE International Conference on Robotics and Automation (ICRA)*, pp. 3818–3824, 2020.

158. Azocar, A. F., L. M. Mooney, L. J. Hargrove, and E. J. Rouse, "Design and characterization of an open-source robotic leg prosthesis," in *2018 7th IEEE International Conference on Biomedical Robotics and Biomechatronics (Biorob)*, pp. 111–118, 2018.

159. Elery, T., S. Rezazadeh, C. Nesler, and R. D. Gregg, "Design and validation of a powered knee ankle prosthesis with high torque, low-impedance actuators," *IEEE Transactions on Robotics*, Vol. 36, no. 6, pp. 1649–1668, 2020.

160. Lenzi, T., M. Cempini, L. Hargrove, and T. Kuiken, "Design, development, and testing of a lightweight hybrid robotic knee prosthesis," *The International Journal of Robotics Research*, Vol. 37, p. 027836491878599, 07 2018.

161. Dawley, J., K. Fite, and G. Fulk, "Emg control of a bionic knee prosthesis: Exploiting muscle co-contractions for improved locomotor function," *International Conference on Rehabilitation Robotics*, Vol. 2013, pp. 1–6, 06 2013.

162. Wang, J., O. A. Kannape, and H. M. Herr, "Proportional emg control of ankle plantar flexion in a powered transtibial prosthesis," in *2013 IEEE 13th International Conference on Rehabilitation Robotics (ICORR)*, pp. 1–5, 2013.

163. Greff, K., R. Srivastava, J. Koutnik, B. Steunebrink, and J. Schmidhuber, "Lstm: A search space odyssey," *IEEE Transactions on Neural Networks and Learning Systems*, Vol. 28, 03 2015.

164. Bi, L., A. G. Feleke, and C. Guan, "A review on emg-based motor intention prediction of continuous human upper limb motion for human-robot collaboration," *Biomedical Signal Processing and Control*, Vol. 51, pp. 113–127, 2019.

165. Chen, C., Y. Yu, X. Sheng, and X. Zhu, "Non-invasive analysis of motor unit activation during simultaneous and continuous wrist movements," *IEEE Journal of Biomedical and Health Informatics*, Vol. 26, no. 5, pp. 2106–2115, 2022.

166. Gupta, R., I. S. Dhindsa, and R. Agarwal, "Continuous angular position estimation of human ankle during unconstrained locomotion," *Biomedical Signal Processing and Control*, Vol. 60, p. 101968, 2020.

167. Rabe, K., and N. Fey, "Evaluating electromyography and sonomyography sensor fusion to estimate lower-limb kinematics using gaussian process regression," *Frontiers in Robotics and AI*, Vol. 9, p. 716545, 03 2022.

168. Zhang, Q., A. Iyer, Z. Sun, K. Kim, *et al.*, "A dual-modal approach using electromyography and sonomyography improves prediction of dynamic ankle movement: A case study," *IEEE Transactions on Neural Systems and Rehabilitation Engineering*, Vol. 29, pp. 1944–1954, 2021.

169. Ren, B., Z. Zhang, C. Zhang, and S. Chen, "Motion trajectories prediction of lower limb exoskeleton based on long short-term memory (lstm) networks," *Actuators*, Vol. 11, p. 73, 02 2022.

170. Huihui, C., G. Farong, C. Chao, and T. Taixing, "Estimation of ankle angle based on multi-feature fusion with random forest," in *2018 37th Chinese Control Conference (CCC)*, pp. 5549–5553, 2018.

171. Wang, J., L. Wang, S. M. Miran, X. Xi, *et al.*, "Surface electromyography based estimation of knee joint angle by using correlation dimension of wavelet coefficient," *IEEE Access*, Vol. 7, pp. 60522–60531, 2019.

172. Wang, J., Y. Dai, T. Kang, and X. Si, "Research on human motion recognition based on lower limb electromyography (emg) signals," in *2021 IEEE 4th International Conference on Electronics Technology (ICET)*, pp. 1234–1239, 2021.

173. Li, T.-H. S., P.-H. Kuo, C.-H. Cheng, C.-C. Hung, *et al.*, "Sequential sensor fusion-based real-time lstm gait pattern controller for biped robot," *IEEE Sensors Journal*, Vol. 21, no. 2, pp. 2241–2255, 2021.

174. Goodfellow, I., Y. Bengio, and A. Courville, *Deep Learning*, MIT Press, 2016.

175. Molnar, C., *Interpretable Machine Learning*, Lulu.com, 2020.

176. Khan, S., A. Khan, and O. Farooq, "Pattern recognition of emg signals for low level grip force classification," *Biomedical Physics and Engineering Express*, Vol. 7, 09 2021.

177. Aghasadeghi, N., H. Zhao, L. J. Hargrove, A. D. Ames, *et al.*, "Learning impedance controller parameters for lower-limb prostheses," in *2013 IEEE/RSJ International Conference on Intelligent Robots and Systems*, pp. 4268–4274, 2013.

178. Wu, R., M. Li, Z. Yao, W. Liu, *et al.*, "Reinforcement learning impedance control of a robotic prosthesis to coordinate with human intact knee motion," *IEEE Robotics and Automation Letters*, Vol. 7, no. 3, pp. 7014–7020, 2022.

179. Gil, M., M. Albert, J. Fons, and V. Pelechano, "Designing human-in-the-loop autonomous cyber-physical systems," *International Journal of Human-computer Studies*, Vol. 130, pp. 21–39, 2019.

180. Merletti, R., and P. J. Parker, *Electromyography: physiology, engineering, and non-invasive applications*, Vol. 11, John Wiley and Sons, 2004.

181. Scheme, E., and K. Englehart, "Electromyogram pattern recognition for control of powered upper-limb prostheses: state of the art and challenges for clinical use.," *Journal of Rehabilitation Research and Development*, Vol. 48, no. 6, 2011.

182. Choi, A., H. Jung, and J. H. Mun, "Single inertial sensor-based neural networks to estimate com-cop inclination angle during walking," *Sensors*, Vol. 19, no. 13, p. 2974, 2019.

183. Wu, B., J. Zhong, and C. Yang, "A visual-based gesture prediction framework applied in social robots," *IEEE/CAA Journal of Automatica Sinica*, Vol. 9, no. 3, pp. 510–519, 2021.

184. Li, Z., Y. Xia, D. Wang, D.-H. Zhai, *et al.*, "Neural network-based control of networked trilateral teleoperation with geometrically unknown constraints," *IEEE Transactions on Cybernetics*, Vol. 46, no. 5, pp. 1051–1064, 2015.

185. Karnam, N. K., S. R. Dubey, A. C. Turlapaty, and B. Gokaraju, "Emghandnet: A hybrid cnn and bi-lstm architecture for hand activity classification using surface emg signals," *Biocybernetics and Biomedical Engineering*, Vol. 42, no. 1, pp. 325–340, 2022.

186. Puig, D., and M. A. García, "Determining optimal window size for texture feature extraction methods," in *IX Spanish Symposium on Pattern Recognition and Image Analysis*, Vol. 2, pp. 237–242, 2001.

187. Englehart, K., and B. Hudgins, "A robust, real-time control scheme for multifunction myoelectric control," *IEEE Transactions on Biomedical Engineering*, Vol. 50, no. 7, pp. 848–854, 2003.

188. Oskoei, M. A., and H. Hu, "Myoelectric control systems - a survey," *Biomedical signal processing and control*, Vol. 2, no. 4, pp. 275–294, 2007.

189. Chen, Y., H. Jiang, S. Yu, and S. Chen, "The classification of surface electromyographic for ankle eversion and inversion based on cerebellar model neural networks," in *2019 15th International Conference on Mobile Ad-Hoc and Sensor Networks (MSN)*, pp. 353–356, 2019.

190. Liu, G., L. Zhang, B. Han, T. Zhang, *et al.*, "Semg-based continuous estimation of knee joint angle using deep learning with convolutional neural network," in *2019 IEEE 15th International Conference on Automation Science and Engineering (CASE)*, pp. 140–145, 2019.

191. Li, M., J. Wang, S. Yang, J. Xie, *et al.*, "A cnn-lstm model for six human ankle movements classification on different loads," *Frontiers in Human Neuroscience*, Vol. 17, p. 1101938, 2023.

192. Hargrove, L., A. Simon, R. Lipschutz, S. Finucane, *et al.*, "Non-weight-bearing neural control of a powered transfemoral prosthesis," *Journal of Neuroengineering and Rehabilitation*, Vol. 10, p. 62, 06 2013.

193. Keleş, A., R. Türksoy, and C. Yucesoy, "The use of nonnormalized surface emg and feature inputs for lstm-based powered ankle prosthesis control algorithm development," *Frontiers in Neuroscience*, Vol. 17, 07 2023.

194. Bai, D., T. Liu, X. Han, and H. Yi, "Application research on optimization algorithm of semg gesture recognition based on light cnn+lstm model," *Cyborg and Bionic Systems*, Vol. 2021, 2021.

195. Ullah, A., S. Ali, I. Khan, M. A. Khan, *et al.*, "Effect of analysis window and feature selection on classification of hand movements using emg signal," in *Proceedings of SAI Intelligent Systems Conference*, pp. 400–415, Springer, 2020.

196. Zhang, F., and H. Huang, "Source selection for real-time user intent recognition toward volitional control of artificial legs," *IEEE Journal of Biomedical and Health Informatics*, Vol. 17, no. 5, pp. 907–914, 2012.

197. Suplino, L. O., G. C. de Melo, G. S. Umemura, and A. Forner-Cordero, "Elbow movement estimation based on emg with narx neural networks," in *2020 42nd Annual International Conference of the IEEE Engineering in Medicine and Biology Society (EMBC)*, pp. 3767–3770, 2020.

198. Hajian, G., and E. Morin, "Deep multi-scale fusion of convolutional neural networks for emg-based movement estimation," *IEEE Transactions on Neural Systems and Rehabilitation Engineering*, Vol. 30, pp. 486–495, 2022.

199. She, H., J. Zhu, Y. Tian, Y. Wang, *et al.*, "Semg feature extraction based on stockwell transform improves hand movement recognition accuracy," *Sensors*, Vol. 19, no. 20, p. 4457, 2019.

200. Rasch, M., A. Martino, M. Drobics, and M. Merenda, "Short-term time series forecasting based on edge machine learning techniques for iot devices," in *2022 7th International Conference on Smart and Sustainable Technologies (SpliTech)*, pp. 1–5, IEEE, 2022.